

THE UNIVERSITY OF CHICAGO

SYNTHESIS AND CHARACTERIZATION OF VARIED SILICON NANOMATERIAL
INTERFACES FOR PHOTORESPONSIVE APPLICATIONS

A DISSERTATION SUBMITTED TO
THE FACULTY OF THE DIVISION OF THE PHYSICAL SCIENCES
IN CANDIDACY FOR THE DEGREE OF
DOCTOR OF PHILOSOPHY

DEPARTMENT OF CHEMISTRY

BY
KELLIANN CLEARY KOEHLER

CHICAGO, ILLINOIS

AUGUST 2019

Abstract

The field of nanomaterials is ever expanding, populated with a wealth of nanostructures that have been effectively integrated into almost every field there are successful applications ranging from photovoltaics, biosensing and stimulation, photocatalytic water reduction, cellular stimulation, infrared detectors, gas sensing and monitoring to address a few. The source of this variety stems from the ability to capitalize on the well explored bulk properties of the base materials while the size scale confers an entirely new set of mostly unexplored properties. This duality dominates the nano-regime. Nanomaterials promise to provide better insight into fundamental studies and simultaneously guarantees advancements for practical applications and technologies. We will use this technology to develop advancements for traditional roles while opening up new unexplored platforms. The source of this vast potential arises from the shrinking length scale paired with increased surface area. As sizes are reduced the structure, morphology, and surfaces are precisely controlled through the synthesis process. Despite the range of nanomaterials that have been developed there still exists a tremendous number of properties, effects, and functionalities that have yet to be explored.

Here we set out to explore and characterize the variation in a cross section of silicon nanomaterials and exploit our depth of knowledge in this region to employ targeted nanomaterial fabrication to specific silicon interfaces. The silicon choice for base structural competent here is strategic as silicon nanomaterials integrate the indirect band gap of silicon, synthetic control over morphology, chemical composition, doping profile, biodegradable and nontoxic functionality, and the potential for widely accessible silicon chemistry for surface modifications. Most significantly, the indirect band gap of silicon provides optical absorption over a wide range of wavelengths in the visible and near infrared (IR) portion of the electromagnetic spectrum provide the potential for

photothermal and photoelectric processes for optical stimulation at the silicon interface. Within the scope of this work we will characterize the properties dictating silicon interfaces.

In the first part we will address both bulk and surface modifications to (1) the bottom up CVD fabrication process of silicon nanowires (SiNWs) and (2) post synthetic modifications to surface structure. From this analysis of the range of modifications we will develop an understanding of the impacts of these processes on factors such as surface chemical variation and surface electrical structure. In this study, all modifications will look at new approaches to tailor the surfaces of silicon nanostructures. This opens up new methods to implement the bottom up synthesis to precisely arrange materials down to submicron or nanoscale dimensions. We then demonstrate several applications of this analysis protocol to direct fabrication of novel materials and implement these creative designs to tailor materials to unique silicon interfaces. In our second approach, we employ the same analysis procedures to guide post synthetic surface modifications including silicon functionalization, etching, and silicide coating. We analyze these range of synthesis procedures for tailoring the silicon nanostructure interfaces to understand how they make materials more or less effective in specific applications. With this fundamental study we establish an understanding of the vast range of surface properties that arise from a small cross section of materials and then explore the possible silicon interfaces that can be controlled from this point.

In the second part of this work I will leverage the guidelines which arose from part one to establish a method of using this analysis to apply well characterized silicon interfaces for specific applications. In this portion we explore the interaction of silicon nanostructure interfacing with polymers, cells, tissues, and water surfaces. At silicon nanostructure – polymer interface we demonstrate the potential to imbed previously inaccessible functionality to well explored polymers. As silicon has biocompatibility and optical stimulation properties ideal for integration

with biointerfaces, we next explore the photoelectric stimulation at cardiomyocyte cell interfaces. In a third approach, we expand on this stimulation at biointerfaces to explore the SiNW tissue interface. In a final approach, we examine the impact of silicon nanostructures assembled into hierarchical nanostructured porous structures for modulating water interfaces in unique biomimetic approaches.

Through this work we produce a platform for surface characterization able to directly analyze the changes in surface chemical composition, surface band structure, and work function. We demonstrate the use of this analysis method for identifying changes to the silicon interface resulting from both CVD synthesis and post synthesis modifications. From this fundamental study we can develop a guiding design more precisely synthesize nanomaterials for a range of applications. We then integrate this analysis with materials applications to utilize the targeted synthesis of silicon for specified material interfaces.

Acknowledgements

The course of my PhD research has been a wide exploration of research focuses from XPS research to clean room fabrication to cellular studies and everything in between. Although at times the variety between these fields seemed too large a gap to bridge, at the culmination of this work it has become clear how much each different research field has bolstered my deeper understanding of each individual research area. This diverse exploration was made possible exclusively by the support of my advisor, Professor Bozhi Tian. From the first time I spoke with him I was impressed by the ability to understand and integrate ideas from a range of research fields to produce incredibly creative research ideas and novel approaches. From every group meeting and talk we have had since Professor Tian has trained us and pushed us to be creative in the development of our scientific thinking and project development. I have been continually impressed by the breadth and depth of the ideas and method of developing new research approaches by Professor Tian. I was especially impressed by the training in the cooperative development of novel research plans through the participation of group conversations integrating ideas from wide ranging fields. Moving forward in my career, I am appreciative of the time and effort Professor Tian has invested in training me in creative scientific thinking supported by rigorous scientific work and collaborative support.

I would especially like to thank Professor Tian for supporting me in my exploration of XPS work in conjunction with my main projects. Initially this began as supporting research for other projects and as we explored a wider range of materials I discovered what an amazing tool it was for discovering new science in our field and discovered how much I enjoyed it. This personal development of course would not have been possible without the unending and above and beyond training and support of Dr. Alex Filatov. I want to sincerely thank Dr. Filatov for spending so much time working through challenging research questions with me and providing so much insight

in research, paper writing, and professional development. Through all of this support of my interest in XPS research I was incredibly fortunate to find a job where I will be able to continue to develop these skills and expand into new fields. I want to sincerely thank everyone who helped push me in this direction because without this extensive background my career trajectory would be an entirely different one.

In the Tian Lab I was fortunate to participate in a number of collaborative projects with many of the lab members. Primarily I would like to thank Dr. Ramya Parameswaran for her work collaborating with me for the SiNW – polymer based cardiomyocyte stimulation work. Not only did she push this work to produce a fantastic paper, but working with her I learned so much about how I can improve my writing skills, presentation skills, and scientific rigor. I not only learned so much working with her, but I also was appreciative of the friendship and support. I would also like to thank Dr. Hemi Rotenberg for his significant contribution to this work providing an entirely new field of tissue studies for us to add to this work. Additionally, I greatly appreciated the chance to work with Dr. Zhiqiang Luo and Andrew Phillips on two additional projects. Both provided novel scientific insight and the chance to expand and explore new research concepts I had not had experience with prior to working with them. I want to thank Dr. Yuanwen Jiang and Dr. Yin Fang for allowing me to characterize their materials by XPS for their papers. I am also appreciative to everyone else in the Tian lab; Youjin Lee, Hector Acaron Ledesma, Dr. Yin Fang, Dr. Xiang Gao, Dr. Yin Fang, Dr. Yiliang Lin, Vishnu Nair, Lingyuan Meng, Zifan Ye, Jessica Morgan, Dr. John Zimmerman, Dr. Jaeseok Yi, who provided scientific insights and support whenever I was struggling with a new topic.

I want to thank all of my undergraduate students who collaborated with me and contributed to almost all of my research efforts; Dara Weiss, Tom Hayes, Genevieve Nemeth, John Hickernell,

Kiela Moreno, Michael J. Burke, and especially Nivedina Sarma who has contributed to our lab for so long. Working with these students has been the best part of my PhD because they provided an endless amount of optimism and enthusiasm for the scientific process and all provided amazing scientific insights. I would especially like to thank Nivedina Sarma who has helped in the majority of my projects, established amazing projects of her own, and has taught me a lot about how to be a fantastic presenter, writer, and researcher. I wish her and all of the undergraduate students who spent so much time working with me the best for their careers after University of Chicago.

External to the Tian lab I would like to thank Andriy Neshchadin and Erik Schaumann who both collaborated with me on projects included in my thesis work. These projects provided new research directions and both were fantastic collaborators both for scientific insight and the fantastic lab environment they created. I would also like to especially thank both Maggie Hudson and Eric Janke for the constant support and research insights. I have asked so much in a scientific capacity and every time there is an incredible amount of scientific insights. Additionally, I would like to thank them and all of my other friends and family who supported me through graduate school including Kade Head-Marsden, Ali Raeber, Kat Scott, Chrissy Hartigan, my siblings and especially my parents. Without all of their unconditional support I would never have made it this far in my career. I would like to dedicate this thesis to my parents and take this time to thank them for the excessive love and support throughout the entire PhD including everything from listening to practice talks, reading paper drafts, helping with taxes, moving from apartment to apartment, cards and gummy bears during the stressful seasons, CSOTD, and the book length emails and texts of supportive messages even when I didn't realize I needed it.

Table of Contents

List of Figures	xv
List of Tables	xix
Chapter 1 : Introduction	1
1.1 Overview of nanomaterial interfaces	1
1.2 Shrinking to the nanoscale	2
1.3 The range of nanomaterials demonstrated for advanced applications	2
1.3.1 Carbon based nanomaterials	3
1.3.2 Gold nanoparticles	4
1.3.3 Polymeric nanomaterials	5
1.3.4 Silicon nanomaterials	5
1.4 Synthetic modification of silicon structures dictating silicon surfaces	7
1.4.1 Top down fabrication	8
1.4.2 Bottom up synthesis	8
1.5 Post synthesis modifications for tuning surface properties	11
1.6 Semiconductor properties exploited for photoresponsive applications	12
1.6.1 Photoelectric applications.....	13
1.6.2 Photothermal applications	14
1.7 Applications of silicon materials to interfaces	15
1.7.1 Polymer nanostructures interfaces	15
1.7.2 Biomaterial interfaces	16
1.7.2.1 Extracellular	17
1.7.2.2 Intracellular	17

1.7.3	Tissue interfaces	19
1.7.4	Environmental application interfaces	20
1.7.5	Nanomaterial water interfaces	21
1.8	Thesis Overview	23
1.9	Bibliography	27

Chapter 2 : XPS and UPS characterization of variability in silicon SiNW surfaces during CVD synthesis; surface chemical composition and band structure

2.1	Introduction	31
2.2	Results and Discussion	32
2.2.1	Employing CVD synthesis to alter chemical composition and band structure at the surface of silicon nanostructures	32
2.2.1.1	Gold diffusion process	36
2.2.1.2	XPS chemical analysis	41
2.2.1.3	UPS provides work function analysis	44
2.2.1.4	XPS and UPS band structure	46
2.2.2	Implementation of XPS analysis methods to characterized nanostructures with CVD synthetic variations for specific applications.	51
2.2.3	Atomic gold at the surface of PIN SiNWs is key to photoelectrochemical stimulation at biointerfaces as demonstrated by neuronal stimulation	52
2.2.3.1	Identifying gold at the surface of PIN SiNWs by XPS	53
2.2.3.2	Optical stimulation at the PIN SiNW neuron interface is capable of eliciting an action potential	55

2.2.3.3 Atomic gold is an important component for photoelectric stimulation at the PIN SiNW	56
2.2.4 Silicon metal alloy interface dictates surface chemical patterning	57
2.2.4.1.1 Characterizing the rows of atomic gold at the SiNW surface by XPS	58
2.2.4.1.2 Phosphine effects on gold	59
2.2.4.1.3 Stick slip motion depends on the chemical environment at the silicon interface	60
2.2.5 Conclusions and Outlook	61
2.3 Experimental	62
2.4 Bibliography	64
 Chapter 3 : Exploring the post-synthetic tuning of silicon nanostructures for specific bio interfaces	
3.1 Introduction	66
3.2 Results and discussion	66
3.2.1 Silicon chemistry employed for surface functionalization	66
3.2.1.1 APTES based functionalization of SiNW surface with molecular photodiode for targeting cell membranes	67
3.2.1.2 Undecylenic Acid functionalization of SiNWs for antibody based targeting to T Cells	70
3.2.2 Etching SiNWs to advance photothermal properties for stimulating retinal cells .	71
3.2.2.1 XPS analysis of SiNW identifying gold during the MACE etching process.	72
3.2.3 Silicon nanostructures modified with varied metal coatings; gold, titanium, aluminum, for modifying silicon water interface to tailor redox reactions	74

3.2.3.1	Metallic gold sputter coating and e-beam deposition shift structure and fermi edge	75
3.2.3.2	ALD of TiO ₂ on PIN SiNWs	77
3.2.3.3	ALD Al ₂ O ₃ on PIN SiNWs	77
3.2.4	Characterizing gold silicon interface of gold nanomesh on silicon heterojunction for optical stimulation at biointerfaces	79
3.2.4.1	Gold nanomesh structure provides evidence of an Au-Si interface promoting photoelectrochemical processes	79
3.2.4.2	The measurements of photoresponse of silicon nanomeshes in solution provide insight into the effect on biointerfaces	81
3.2.5	Conclusions and Outlook	82
3.3	Experimental	83
3.4	Bibliography	84
 Chapter 4 : Polymer composite with heterogeneous nanowire incorporation for free-standing silicon mesh		
4.1	Introduction	86
4.2	Results and Discussion	87
4.2.1	High density PIN SiNW mesh synthesis	87
4.2.2	Nanowire polymer incorporation heterogeneous structure	88
4.2.3	Photolithography and waveguiding	89
4.2.4	Modeling light transfer to surrounding regions	92
4.2.5	Photoelectric effect	93

4.2.6	Mechanical measurements	96
4.2.7	Increased water adhesion properties based on nanostructured surface	98
4.2.8	Conclusions and Outlook	99
4.3	Experimental	100
4.4	Bibliography	103

Chapter 5 : Novel x-y plane scanning based stimulation method paired with photovoltaic polymer - SiNW composite for optical stimulation of isolated cardiac cells.

5.1	Introduction	104
5.2	Results and Discussion	105
5.2.1	Cell – material interface	105
5.2.2	Stimulation method	106
5.2.2.1	Scanning stimulation in the x-y plane	108
5.2.2.2	Simulating the waveguiding properties of SiNW network	110
5.2.3	Demonstrated cellular viability on PIN SiNW scaffold	110
5.2.4	Optical stimulation of cardiomyocytes to alter cardiac beating frequency	112
5.2.5	Importance of break times for cellular stimulation	114
5.2.6	Memory effect resulting from scanning based cellular stimulation	115
5.2.7	Conclusions and Outlook	116
5.3	Experimental	116
5.4	Bibliography	122

Chapter 6 : Altering cardiac tissue beating frequency through the application of the PIN SiNW SU-8 mesh and scanning stimulation in the z-plane.

6.1	Introduction	124
-----	--------------------	-----

6.2	Results and Discussion	125
6.2.1	Water adhesion properties	125
6.2.2	Water adhesion properties for suture free and adhesion to tissue interface	126
6.2.3	Soft and flexible properties	127
6.2.4	Taking advantage of mechanical contraction for z-plane scanning stimulation ..	128
6.2.5	Increased beating frequency of rat hearts via z-plane scanning stimulation	129
6.2.6	Minimal cytotoxicity results from laser stimulation	132
6.2.7	Conclusions and Outlook	132
6.3	Experimental	133
6.4	Bibliography	135

Chapter 7 : Porous SiNW – Carbon scaffolds for modulated water adhesion

7.1	Introduction	137
7.2	Results and Discussion	140
7.2.1	Fabrication	140
7.2.1.1	Freeze patterning of silicon nanostructures	141
7.2.1.2	Silicon-Carbon Structure	145
7.2.2	Hierarchal porous nanostructured interfaces result in a range of water interactions	148
7.2.2.1	Superhydrophobic state with low water adhesion	149
7.2.2.2	Superhydrophobic state with high water adhesion	151
7.2.2.3	Hydrophilic surfaces	153
7.2.3	Materials properties soft and flexible	154
7.2.4	Photothermal properties under illumination	155

7.2.5	Conclusions and Outlook	157
7.3	Experimental	158
7.4	Bibliography	160
Chapter 8	: Conclusion and Outlook	163

List of Figures

Figure 1-1. Silicon nanomaterial fabrication methods, top down vs bottom up.	7
Figure 1-2. CVD growth process including both Vapor Liquid Solid and Vapor Solid growth mechanisms.	9
Figure 2-1. Energy band structure of the silicon – vacuum interface.	34
Figure 2-2. Platform of materials synthesized by CVD for XPS and UPS analysis.	35
Figure 2-3. Central XPS and UPS analysis scheme.	36
Figure 2-4. Gold XPS peak analysis and chemical identification.	40
Figure 2-5. Silicon peak shift comparison for doping variation and structure.	41
Figure 2-6. Silicon peak shift comparison for PIN SiNWs.	42
Figure 2-7. Full UPS spectra reveals three different regions of analysis for nanostructures.	44
Figure 2-8. In-Depth examination of SECO and fermi level.	45
Figure 2-9. Calculated values for band bending and surface dipole for PIN SiNW samples.	46
Figure 2-10. Calculated values for dipole, work function, and band bending are integrated into the band structure to visualize the effect of CVD variations on band structure.	50
Figure 2-11. Characterization of PIN SiNW surfaces.	52
Figure 2-12. In depth analysis of XPS data collected for PIN SiNWs for neuron stimulation.	54
Figure 2-13. Function of SiNWs at cellular interfaces for neuronal stimulation.	56
Figure 2-14. The presence of atomic gold is identified through peak analysis of the Au 4f signal.	58
Figure 3-1. Functionalization scheme for APTES based linkage of molecular photodiode to SiNW.	67
Figure 3-2. Functionalization scheme analyzed by XPS analysis.	68

Figure 3-3. Functionalization scheme linking antibodies to the surface of the SiNW based on undecylenic acid linkage.	69
Figure 3-4. Depth profiling reveals the interface variations for sputter coated and e-beam evaporated gold layers on the PIN SiNW surface.	73
Figure 3-5. UPS characterization of electron density at the fermi edge of PIN SiNWs modified with gold.	75
Figure 3-6. XPS depth of PIN SiNWs modified with metal oxides.	76
Figure 3-7. XPS depth analysis of gold nanomesh on silicon wafers.	78
Figure 4-1. SU-8 scaffold fabrication produced a robust SiNW mesh due to SiNW waveguiding.	87
Figure 4-2. SU-8/SiNW meshes are prepared via a photolithographic patterning	89
Figure 4-3. SiNWs waveguide light during the UV exposure.	91
Figure 4-4. 3D FDTD and FEM Simulations demonstrate nanowire waveguiding.	92
Figure 4-5. Photothermal response of PIN SU-8, III SU-8, SU-8 only, and glass.	94
Figure 4-6. Reduction of SU-8 Modulus after fabrication with microstructure and nanostructure.	95
Figure 4-7. Droplet adhesion measured through pinning of droplet edges during drying.	97
Figure 5-1. x-y scanning based stimulation method for altering cellular activity.	107
Figure 5-2. Simulations demonstrate nanowire waveguiding during scanning based stimulation.	109
Figure 5-3. Biocompatibility is demonstrate by viability assay and cellular alignment on the SU-8 substrate.	111

Figure 5-4. Cellular stimulation with defined x-y scanning method demonstrates effective pacing of cells.	113
Figure 5-5. Optical stimulation of cardiomyocytes on SU-8 grids, glass, and SU-8/III-SiNW meshes do not result in training.	114
Figure 5-6. Break time is key to effective pacing of cardiomyocytes to continue to beat at target frequency.	115
Figure 6-1. Su-8 water adhesion to tissue	126
Figure 6-2. Reduction of SU-8 Modulus after fabrication with microstructure and nanostructure.	127
Figure 6-3. Optical training of adult hearts <i>ex vivo</i>	129
Figure 6-4. PIN SU-8 meshes induce optical training of adult rat hearts <i>ex vivo</i> while III SU-8 meshes and light alone do not.	130
Figure 6-5. PIN SU-8 meshes cause minimal damage from phototoxicity.	131
Figure 7-1. <i>Salvinia Molesta</i> fern produces a stable air - water interface	139
Figure 7-2. Breakdown of the varied air-water interfaces that result from minimal changes in SiNW scaffold synthetic procedure.	140
Figure 7-3. SiNW scaffold fabrication process.	141
Figure 7-4. Freeze casting test with Unidirectional, 2-Directional, and 3-Directional freezing of scaffolds.	142
Figure 7-5. Freeze casting of scaffolds is tested with a variety of SiNW diameters, and the density of SiNWs in PVA.	144
Figure 7-6. SEM Visualizing the variation between hydrophilic and hydrophobic samples.	147
Figure 7-7. Droplet impact studies of flexible and crushed scaffolds.	150

Figure 7-8. Droplet inversion studies demonstrate adhesion at interface is supports droplets
against gravity.152

Figure 7-9. Scaffold compression demonstrates flexibility and recovery.154

Figure 7-10. Photothermal scaffold response and potential for water evaporation.....155

List of Tables

Table 2-1. Ratios of elemental composition calculated from XPS data.	38
Table 2-2. UPS data calculation of work function from SECO.	48
Table 2-3. UPS data calculation of electron affinity, band bending, and surface dipole.	49
Table 2-4. Calculated Au 4f binding energies for the studies of the gold ratio at the surface. ...	53

Chapter 1 : Introduction

1.1 Overview of nanomaterial interfaces

Development of materials provides new tools to either address challenges in well explored applications or provide previously inaccessible platforms with entirely novel functionality. For these nanomaterial devices to be translated to therapeutic or commercialization applications, precise control over the interfaces and synthesis process that directs this interface becomes crucial. The development of a focused design strategy for nanostructures with an understanding of implications of top down or bottom up synthesis is key to control over new properties and structures. Both synthetic approaches have significant impacts on the surface and bulk properties of nanostructures, such as morphology, chemical composition, hierarchical structures. From this strategy for targeted design we are able to improve on device interfaces and performance. Developing new methods of characterizing surface properties and the wide range of synthetic and post synthetic techniques will become more and more important with the expansion of the field.

Nanomaterials provide opportunities to deviate from bulk materials as structures shift towards surface dominated properties. The potential for strict design control over both core composition and surface properties due to the highly tunable nature of both factors. Nanomaterials have potential for advancing both fundamental studies and practical applications. Silicon, specifically, has been fabricated with a range of nanostructures including; 0-dimensional silicon quantum dots, one dimensional silicon nanowires, 2-dimensional silicon membranes with a range of morphologies and compositions within each category.¹ From this wealth of structures silicon has been integrated for a range of materials applications including photovoltaic, stimulation, biomedical, photocatalytic water reduction, gas sensing, photo detecting, and solar cells.

1.2 Shrinking to the nanoscale

As materials shrink to the nanoscale the dominating factors for materials properties shift from bulk properties to surface properties. Due to the high surface area to volume ratio, shifting towards smaller and smaller devices, surface properties become more and more important. This introduces the importance of effects such as surface state defects, band bending, surface dipole, and chemical contamination. Many physical properties can be enhanced or tuned compared to bulk materials such as physiochemical properties, melting point, material wettability, electrical or thermal conductivity.² One of the demonstrated effects of shrinking to the nanoscale is the changes in both light absorption and scattering. The large surface area that exists for nanoscale devices is key for applications such as water treatment or enhanced photocatalytic activity. For photoelectric applications, this high surface area has been shown to increase light harvesting efficiency.³ Additionally, the large surface to volume ratio has been applied to increase sensitivity for sensing device applications. In other cases, these properties have been leveraged for water treatment, wettability changes, smart actuator, transparent coatings, electrodes applications. Developing more specific control over these interfaces will provide access to implementing nanomaterials in a wider range of applications.

1.3 The range of nanomaterials demonstrated for advanced applications

Nanomaterials have been successfully implemented in a range of applications both industrial purposes and fundamental research. With the potential to unlock unique properties due to the nanoscale properties the wealth of materials in this range has become abundant. This range of materials can be categorized based on the size, shape, and composition. Successful materials for photothermal and photoelectric stimulation range from carbon based nanomaterials, quantum dots,

gold nanoparticles, polymers, and silicon nanomaterials. The significant diversity of structure, morphology, composition, and physical properties, reactivity necessitates an understanding of how to manipulate interfaces on the nanoscale for specific applications. Following will be an overview of some of the nanomaterials with comparable functionality to silicon nanomaterials. This will outline the platform of materials, fabrication, applications, and challenges.

1.3.1 Carbon based nanomaterials

Carbon based nanomaterials have been fabricated in a plentiful range of morphologies including tubes, ellipsoids, spheres, sheets ect. This has resulted in fullerenes (C60), Carbon nanotubes (CNTs), nanodiamonds, carbon nanofibers, carbon black, graphene and more. From this spread of materials studies have demonstrated unique electronic, optical, thermal, mechanical, and chemical properties. Much of these materials are fabricated by laser ablation, arc discharge, or chemical vapor deposition (CVD). Research into carbon nanomaterials has demonstrated high mechanical strength paired with electrical conductivity and low dimension. Implementing these properties has provided significant advances in the application of carbon nanomaterials. Carbon black, graphite, graphene, CNTs, carbon composites have been applied to plasmonic solar driven steam generation, efficient light to heat conversation, rapid water evaporation.⁴

At bioelectronic interfaces carbon nanomaterials operate at a size range that provides unique methods of interacting with living systems by provides intimate contact with cells. The shape and materials properties can be tailored for specific cell systems. In addition, carbon chemistry provides potential for surface functionalization allowing for the modification with specific target molecules or fluorescence tags for cellular interfaces. CNTs based on size and cellular interface have been shown to be applicable to neuronal sensing and stimulation.⁵⁻⁷ Additionally, the interfacing of CNTs with polymers for the fabrication of microelectrodes was

key to drastically increasing sensitive of neuronal sensing.^{8,9} CNTs have also been shown to be successful for stem cell differentiation to neurons.¹⁰ Currently the biggest challenge facing the integration of carbon nanomaterials in biomedical applications is the conflicting literature on the toxicity of these materials.¹¹⁻¹³ Further investigation into the specific properties resulting in the toxic effect on cells is key.

1.3.2 Gold nanoparticles

Gold is a well explored nanomaterial system due to the unique properties at the nanoscale. Mainly gold has been employed for photothermal stimulation at the nanomaterial interface. Gold nanomaterials undergo plasmonic heating when stimulated at the resonance wavelength. Compared to other semiconductor materials system gold nanomaterials provide only photothermal potential with no photovoltaic potential.

This material has been used for applications to biotechnology due to the potential for easy delivery, sensing and stimulation potential, large surface area, and facile surface functionalization with antibodies, proteins, oligonucleotides.¹⁴ With the potential for surface functionalization binding events at the cell nanoparticle interface has been shown to alter surface plasmon resonance, material conductivity, and redox activity. These detectable changes in signal can be used for sensing applications.¹⁵

In a stimulation capacity core shell magnetic gold nanoparticles¹⁶ have been shown to combine radiotherapy and photothermal therapy to enhance targeting of tumor tissue. These materials were shown to have uniform morphology and enhanced surface plasmon resonance and enhanced superparamagnetic properties. Core shell magnetic gold nanoparticles demonstrated high photothermal conversion efficiency. With these properties, NIR irradiation at the nanoparticle

cell interface was effective for photothermal killing of cervical cancer cells. Application of an external magnetic field was shown to synergistically enhance anticancer efficacy.¹⁶

1.3.3 Polymeric nanomaterials

Polymers provide a wide scope of structures accessible based on modifications of fabrication methods and material composition. Nanostructures can be leveraged in this space through either the formation of composite materials combining NP with bulk polymer materials as well as the synthesis of polymer structures in the NP size range. Polymer composites utilize a polymer base and take advantage of the NP structures to enhance properties. The biggest challenge for the polymer field is the difficulty in tuning photovoltaic properties for wide ranges such as other materials, the challenge of fabrication for devices compared to facile SC devices, and they often have lower energy conversion efficiency.^{17,18}

Conducting polymers can be fabricated on the nanoscale for nongenetic photostimulation. In one approach nanoparticles were fabricated via an emulsion method from a diketopyrrolopyrrole polymer with strong light absorption in the NIR optical window.¹⁹ These polymer NP demonstrated strong light absorption and efficient photothermal conversion with light to heat conversion efficiency of 49.5%. NP demonstrated biocompatibility and were taken up by cells. Under irradiation in the NIR window polymer NP were specifically targeted HeLA cell viability. This demonstrated the potential for targeting cancer cells and employing photothermal based cancer cell killing potential as a therapeutic approach with polymers fabricated on the nanoscale.

1.3.4 Silicon nanomaterials

Silicon has been fabricated on the nanoscale as 2D membranes, 1D nanowires, and 0D quantum dots because as a bulk material it provides the potential to take the traditional silicon

properties and integrate new ones based on surface variations. The advantages of silicon for nanostructure synthesis includes the ability to manipulate geometry, length scale, diameter, chemical composition, doping profile, and chemical reactivity of silicon based on surface chemistry. In addition to this silicon has been shown to be biodegradable and nontoxic.²⁰ Under physiological conditions silicon structures have been shown to degrade to Si(OH)_4 silica.^{20,21} The most interesting property for nanostructure stimulation arises from the indirect band gap of 1.1 eV with significant absorption of optical wavelengths through the near infrared (NIR). This absorption of a broad range of light wavelengths make silicon nanostructures key for stimulation by two main parallel processes; photoelectric or photothermal.

Even within well explored platforms such as silicon nanowires the effects of VLS process, choice of the metal catalyst, morphology, and even diameter simple variations have many unknown consequences. Within the Tian Lab we have recently discovered evidence of a “coffee ring effect” for 3D patterning of gold atoms based on dopant interactions. Specifically, the use of gold nanoparticles, one of many options for metal nanoparticle catalysts, dictates the variations in the CVD process resulting in significant alteration of surface properties. While there is an impressive control over structural morphologies of SiNWs and there is evidence that the geometric modulation can affect properties such as electrical conduction there is as of yet minimal exploration addressing the true range and impact of these geometric modifications as much is focused on composition variation. Finally, and possibly most simply, the key properties of SiNWs in the diameter range of nanowires from 1 nm – 100 nm is relatively well explored, the range of SiNWs larger than that 100 nm – 1000 nm is still a underdeveloped field. As illustrated by this breakdown, even a microscopic cross section of the challenges to understanding materials at the nanoscale is still widely unknown.

1.4 Synthetic modification of silicon structures dictating silicon surfaces

By identifying the workspace of synthetic modifications we can more specifically target fabrication methods for desired applications. This includes both nanostructure synthesis processes; bottom up or top down, as well as post synthesis processes. Understanding these controls opens up new routes for developing novel nanostructures or for tracking why nanostructures are useful in specific applications. There are many well explored methods of synthesizing nanoparticles that generally fall under the categories of top down fabrication or bottom up synthesis including; vapor phase synthesis, chemical precipitation, laser ablation, arc discharge methods, mechanical milling, ect. The biggest challenge to advancing Si nanomaterials into wider applications is the process requirements for large scale production of pure atomically precise, nanoparticles with uniform size distribution, morphology, crystallinity, chemical composition. Control over these properties is key and is important to be achievable while increasing scalability potential and reducing production costs.²² Developing methods of control over these factors and expanding the fabrication workspace will expand the utilization of nanomaterials in industrial applications and fundamental research fields.

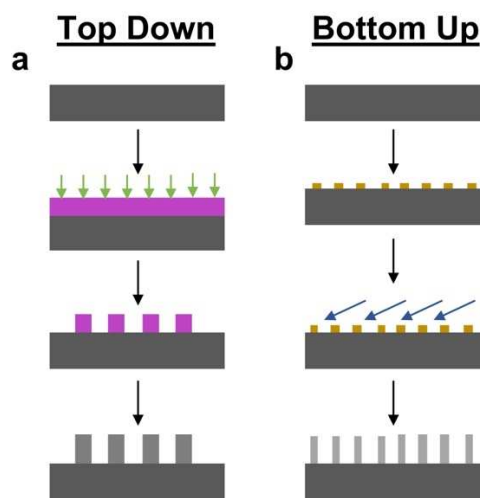


Figure 1-1. Silicon nanomaterial fabrication methods, top down vs bottom up. a. Silicon nanomaterials can be fabricated through two main approaches. One example of top down fabrication methods relies on lithographic patterning. A photoresist (purple) is added to a silicon wafer (grey) and patterned with UV light (green). Then

Figure 1-1 continued. the wafer is etched revealing nanostructures protected by photoresist pattern with the size and etch time determining structure. Removal of photoresist reveals nanomaterials (grey). **b.** In the bottom up approach, silicon wafers are patterned with metallic nanoparticles (yellow). Precursor gasses (blue) are introduced to the sample at proper temperatures to form a eutectic alloy of silicon and desired metal nanoparticle. As silicon becomes supersaturated in the droplet catalyst, it will precipitate out below the nanoparticle. Through this process nanostructures grow vertically with the size determined by the nanoparticle diameter and growth time.

1.4.1 Top down fabrication

The methods that fall under the umbrella of top down fabrication focuses on reducing the size of a uniform material to create the desired nanostructures. (Figure 1-1 a) The main benefit of the top down method is the potential for large scale synthesis of nanostructures and the potential to scale up batch sizes while maintaining material quality. In one top down approach the fabrication process uses lithographic patterning of a surface to etch down into materials revealing nanostructures. This process additionally provides significant surface variation. This approach is common for the electronics industry to produce unique circuitry.²² In other approaches mechanical milling is applied produce nanoparticles. Milling relies on the mechanical disintegration of metals to small particles under collision with balls. This is typically used for production of hard metals, oxide powders, ceramics or composites. The downside to this approach is the challenge of producing uniform structures due to internal stress introduced by the process as well as structural defects and contamination.²² The main challenge facing all bottom up approaches is the ability to produce wide scale is uniform nanoparticles while conferring precise atomic control over structures.

1.4.2 Bottom up synthesis

Bottom up synthesis overcomes some of the challenges facing top down fabrication by providing precise control by assembly of atoms or molecules into larger nanostructures based on chemical or physical approaches. (Figure 1-1 b) In this approach, we will focus on bottom up synthesis methods with nanostructure growth schemes that rely on vertical growth from a growth

substrate. The biggest benefit of this method is that it provides the potential for highly controlled properties down to micron or nanoscale level precision. For this work we focus on the chemical vapor deposition (CVD) methods of metal catalyzed vapor liquid solid (VLS) and vapor solid (VS).²³ Specifically, this method provides temporal control over structures with the vertical growth being a time controlled process. (Figure 1-2) Additionally, the CVD synthesis conditions, temperature, pressure, and doping ratio have all been employed to exert nanoscale control over fabrication. With these controls CVD synthesis has been demonstrated to precisely dictate chemical composition, morphology, structure core shell, gold, size, band bending, chemical potential, surface dipole.

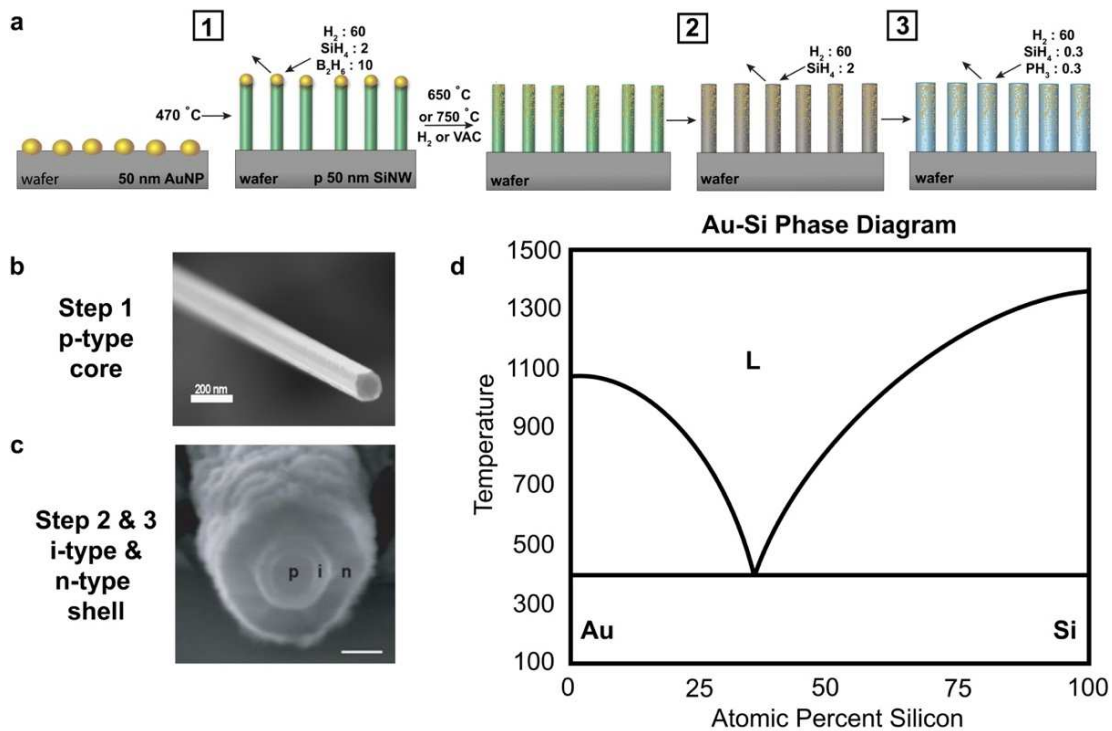


Figure 1-2. CVD growth process including both Vapor Liquid Solid and Vapor Solid growth mechanisms.
a. CVD Core and Core-Shell growth process is based on both VLS and VS mechanisms. Initially gold nanoparticles (yellow) are deposited on to the surface of the silicon wafer. (1) At 470°C the VLS growth mechanism dominates. For p-type (green) core growth, silane, hydrogen, and diborane are introduced to initiate SiNW growth. After core growth is complete the shell method can be grown by VS mechanism by ramping to temperatures above 650°C under vacuum or hydrogen. During this process the metallic gold nanoparticle diffuses down the surface of the SiNW to form gold nanoclusters and atomic gold. (2) Once appropriate temperatures are achieved, shell growth occurs radially. First the intrinsic shell (purple) is grown with hydrogen and silane, and then the n-type shell (blue) is grown with hydrogen, silane, and phosphine. During the shell

Figure 1-2 continued. growth process gold has the ability to travel to the surface of the SiNW from the interior p-type core. **b.** SEM image of p-type core SiNW grown via VLS mechanism. (Scale bar 200 nm) **c.** SEM image of PIN core-shell SiNW with p-type core grown through VLS method and shells through VS method. (Scale bar 100 nm) **d.** VLS growth mechanism schematic diagram demonstrates the basis of the method reliant on the Au-Si phase diagram. This diagram includes the solid crystalline phase at the bottom shifting based on atomic percent of silicon. The eutectic phase is shown in the upper portion of the diagram. **e.** Reproduced from Ref. 32

The general approach revolves around the use of a gaseous precursor silane (SiH_4) is introduced to a vacuum. The silane gas decomposes to Si and H_2 at high temperatures. For nanostructure growth, metal nanoparticles act as the catalyst for decomposition of silane. Although gold is the most popular metal catalyst other metals have been employed including copper, indium, gallium, aluminum, ect.²⁴ As the gaseous precursor passes by the metal catalysts a liquid alloy of the Si-metal system is formed above the eutectic temperature. For a gold nanoparticle alloy Si-Au eutectic temperature of ~ 363 °C. Dopants of diborane (B_2H_6) and phosphine (PH_3) are introduced as gasses to achieve SiNW doping as either p-type or n-type Si respectively. Synthesis with no dopant gasses results in intrinsic Si. As increasing amounts of Si is introduced the np catalyst becomes supersaturated causing precipitation of Si to the substrate. This precipitation results in vertical growth of the SiNW with the np catalyst remaining at the tip via (VLS). (Figure 1-2 a,b) Through this method, the morphology and dopant profile can be specifically controlled in the vertical direction over the time course of growth. The SiNW diameter and growth rate is determined by the np diameter and the height is determined by the growth time.²⁴ Vertical patterns of doping or other modifications can be introduced by varying ratios of gasses at periodic intervals during growth.

Alternatively, horizontal wire modifications can be achieved by the vapor-solid growth mechanism (VS). (Figure 1-2 a,c) At higher temperatures, silane can spontaneously decompose on all surfaces in the absence of the catalyst resulting in film growth. This can be used to synthesize membranes on flat wafer substrates or to horizontally grow shells around the SiNW core. Due to

the fact that these two mechanisms occur under similar growth conditions these methods compete during growth and can be observed simultaneously. Reaction conditions such as high growth temperatures and low pressure, can be utilized to select for specifically VS processes. During this high temperature and low pressures synthesis, the growth of shells can be used to modify SiNW properties horizontally such as doping profile. One example of this growth method is coaxial p-i-n SiNWs with a p-type core grown via VLS and two shells intrinsic and n-type.

For our research we specialize on bottom up CVD synthesis of inorganic semiconductors. We focus on silicon for the development of novel materials and the application of silicon in sensing applications, optical stimulation, and study fundamental biology of bioelectronic systems such as neurons, cardiomyocytes, and HUVECS. With the CVD process we are able to produce Si nanowires (SiNWs) and Si membranes or films. In all of our work we focus on gold nanoparticle catalysts as the gold has been demonstrate to participate in key photoelectric, photoelectrochemical, and photothermal processes.

1.5 Post synthesis modifications for tuning surface properties

Targeting bottom up or top down synthesis modifications provides one approach for modifying the surfaces of nanomaterials. Post synthesis modifications provide a rich work space for altering surfaces beyond what is available through other methods. Surface modifications typically rely on surface chemistry based on the chemical ratios available at the surface. For this reason there is some entanglement of CVD synthetic modifications and post synthesis tuning. Both of these approaches provides methods to target different properties such as surface atomic ratios from CVD and chemical composition from compound functionalization. With control over both of these and

an understanding of how one can be leveraged to impact another provides access to a rich work space of materials interfaces.

Previous modifications have explored functionalization with proteins and molecular tags, sputter coating, metal assisted chemical etching and more. Chemical functionalization takes advantage of the silicon surface chemistry to link compounds to target materials to specific interfaces. This can employ thermal or UV alkene or alkyne hydrosilylation²⁵⁻²⁷ on hydrogen terminated silicon surfaces, or silicon functionalization by primary amines²⁸, or APTES functionalization on SiOH surfaces.²⁹ These silicon linkages can be used to bind proteins or antibodies to silicon nanostructure surfaces for targeting materials to bind to specific cells or direct or prevent cellular internalization. In addition to biological applications surface functionalization can tune other surface properties. Aromatic fluorophores, phenanthrene, pyrene, and perylene chromophores, at the surface were shown to sensitize energy transfer at the surface. The functionalization of silicon quantum dots with fluorophores improved quantum yield and tuned photoluminescence emission.³⁰ In other approaches Si can be modified by sputter coating or e-beam evaporation to add metals and metal oxides such as gold or alumina to tailor photoelectrochemical pathways. In another approach metal assisted chemical etching has been shown to enhance surface states and dramatically increasing photothermal pathways. Through these and more surface modifications, the interfaces can be tuned for applications such as cellular targeting or directing photoelectric or photothermal pathways.

1.6 Semiconductor properties exploited for photoresponsive applications

The indirect band gap of silicon semiconductors has many times been demonstrated to provide a key functionality to nanostructures. Through this light absorption silicon semiconductors can

provide optical stimulation via two main pathways; photoelectric and photothermal. The potential to absorb in the NIR range where tissues are transparent paired with the biocompatibility has made silicon nanomaterials a been prime candidates for bioelectronic stimulation and has previously been shown to modulate cellular activity and membrane voltage of neurons through photoelectric stimulation.³¹

Currently, our understanding regarding these optically stimulated processes as the silicon surface is minimal. This understanding is even more limited when we interrogate the physiochemical processes that occur at the silicon surface of physiological solutions. Another complicating factor is the fact that there is no clear picture as to how these processes shift at interfaces altered by surface variations, functionalization, various interfaces, air, water, electrolyte conditions.

To understand the electrical and electrochemical pathways at the silicon interfaces it will be important to characterize the potential shifts at the surface to identify the range of device functions. We can explore how this shifts with different CVD synthesis and post synthesis functionalization altering by size and doping. We also observe the shift resulting from different length scales, membranes, nanowires, large diameter nanowires to provide insight into the understanding of how light induced processes are affected by these properties.

1.6.1 Photoelectric applications

During the photoelectric processes in silicon light illumination produces carriers which accumulate at the surface of the silicon. Under physiological conditions the accumulation of carriers at the surface changes the local surface potential. With this charge accumulation, ions in the media are attracted or repelled based on the photogenerated potential resulting in ionic currents.

The properties of structure size, doping, and surface chemistry can be used to direct desired physiochemical processes at the varied interfaces key for efficient signal transduction and power generation for photovoltaic applications. From previous studies of nanostructure photovoltaic properties are enhanced by the higher surface for light generated carriers.

Previously we have demonstrated the photoelectric potential for silicon nanostructures through the fabrication of coaxial p-type / intrinsic / n-type (PIN) SiNWs.³² For the fabrication of these structures p-type core SiNWs are grown from a growth substrate via vapor liquid solid (VLS) mechanism at 470 °C with a gold liquid alloy growth catalyst. After growth of the p-type core the intrinsic and n-type shells are grown via the vapor solid (VS) growth mechanism. For shell deposition, the temperature is ramped to 750 °C. After the CVD synthesis the PIN core shell structures have the doping profile required for a built in photodiode junction. Under illumination the light generated carriers, electrons and holes, are swept to the shell and core respectively under the influence of the built in electric field. Initial applications for this SiNW structure was photovoltaic and since then has been applied to the optical stimulation of biointerfaces.

1.6.2 Photothermal applications

The competing process to the photoelectric affect is photothermal. Many materials are capable of photothermal heating including metals, gold nanocrystals, semiconductors, metal oxides, graphene, and carbon nanotubes. For materials undergoing photothermal processes, light illumination results in the photogenerated carriers, and then recombination events of light generated carriers convert the photon energy input into the vibrational energy in the silicon lattice. Surface defects in the crystal lattice has been shown to be a site for recombination events, and increasing the surface defects enhances this effect. The heat generated by the recombination events dissipates through the silicon lattice and across the silicon interface based on heat transfer.³³ At

the solution interface, the heat is dissipated into the surrounding electrolyte resulting in elevated temperatures of the surrounding solutions.

1.7 Applications of silicon materials to interfaces

The silicon nanomaterials interfaces determine the biocompatibility, cellular interface, environmental impact, tailoring electronic properties for photothermal or photoelectric applications. As the interface is key to tailoring nanomaterials for specific applications many approaches for altering these surfaces has been explored from synthetic modifications to post synthetic modifications. This provides the ability to narrow down the realm of materials to better suit materials for targeted interfaces or solutions. There has been significant research into leveraging these interfaces for a wide range of applications including polymer nanostructures, biointerfaces, environmental applications, and water interfaces. Following will be an overview of targeted applications of nanomaterials at a variety of interfaces.

1.7.1 Polymer nanostructures interfaces

Polymer nanostructure interfaces dictates the formation of composites. Due to the combinatorial nature of composites there is a wide range of materials that can be accessed. The elongated nature of silicon nanostructures and high surface area allows for significant surface interactions and promotes fiber entanglement. This provides a second advantage is the potential to modify morphology and materials properties based on polymer nanostructure interactions.

Polymer nanostructure composites take advantage of the mechanical properties of both the nanostructure and polymer to form a hybrid with unique properties. This has been demonstrated with the addition of graphene, carbon nanosheets, into polyvinyl alcohol from low to high loading of nanostructures.³⁴ The fully exfoliated graphene nanosheets interface with the PVA chains in an

aqueous solution. This composite demonstrated significant enhancement of mechanical properties with about 150% increase in tensile strength and 10 times increase in Young's modulus of the composite with ideal loading of 1.8% graphene.

Alternatively, polymer nanostructure interfaces can be exploited to alter morphologies of structures. Magnetic properties of nickel and cobalt co-doped ferrite nanostructures³⁵ have been tuned by the addition of a polymer shell. For these materials it has been challenging to gain control over particle size and morphology with synthetic approaches. The addition of the PVA shell was prepared via an ultrasonication process providing access to a range of morphologies including rectangle and self-assembled beads. The significant anisotropy of these shape variations provided enhanced magnetic properties.

1.7.2 Biomaterial interfaces

Biomaterial interfaces provide significant potential for taking advantage of the significant surface to volume ratio of nanomaterials. The surface area not only increases the potential for sensing and stimulation across interfaces, but also operates on a length scale ideal for cellular interfaces. The size regime of nanoparticles is similar to that for cells and biomolecules allowing for novel pathways with cells, provides facile delivery to challenging biological locales, and provides highly localized targeting. These properties have been applied to biointerfaces for biosensing, imaging, stimulation, probes and sensors.

The cell nanostructure interface determines the response of the cells and chronic tissue response it is key to understanding the impact of implants or sensors for therapeutic applications. Surface features and chemical composition dictate the interface with nanostructures are taken up or located at the surface.

1.7.2.1 Extracellular

One regime of biological interfaces for nanomaterials occurs at the extracellular location. This occurs when nanomaterials are targeted to the surfaces of cells and extracellular regions. This interface can be used to track and understand biological properties, sensing at biological interfaces, and modulating cellular interfaces. The high surface area has the potential for extensive nanomaterial cellular junctions. With appropriate composition and structure many nanomaterials have been shown to be biocompatible and biodegradable.

Vertical nanopillar arrays^{36,37} have been studied to understand the substrate constraints that preferentially support cells without penetrating the membrane. In this approach minimal perturbation occurs and the cell viability is not impacted. The cell – nanowire interface morphology is shown to be dictated by post spacing, pitch, and nanostructure diameter. For nanopillars smaller than 300 nm in diameter the cell membrane wraps the nanopillar without penetration of the cell. For closer packed arrays cells sat on top of the array. The increased surface area and tight junction at the nanostructure interface can enhance electrophysiology recordings or stimulation. In another stimulation based approach SiNWs³⁸ free from a substrate were added to neuron culture and stimulated to produce an action potential. After allowing SiNWs to settle to the surface of the cell the nanostructure cell interface was shown to be a tight interface. Under laser illumination at the SiNW cell interface an action potential was produced at the stimulated neuron.

1.7.2.2 Intracellular

In many cases, internalization of nanostructures provides unique access to studying and dictating cellular activity. In these instances, the internalization or surface localization of nanostructures is determined with morphology, chemical composition, and surface modifications. Applying morphological variations to the concept of the vertical nanopillar array can be used as a

minimally invasive approach for nano-injection of biomolecules to cells. Vertical arrays of silicon nanoneedles were fabricated on a flexible elastomer patch to form cell interfaces with low mechanical mismatch. Substrates were shown to be biocompatible and capable of injecting small interfering RNA at a large loading dose.

In substrate free approaches³⁹ nanostructures have been applied to improve fundamental studies as well as stimulate cellular activity. In one approach, semiconductor nanocrystals⁴⁰ were used as fluorescent probes for staining and imaging of mouse fibroblast nuclei and F-actin filaments. Cells took up nanoparticles and then preferentially were bound to one structure based on surface modifications. The surfaces were interfaced with structures through either electrostatics and hydrogen bonding or through a ligand receptor interaction, in this case avidin-biotin. The nanocrystals that were silyanized with trimethylsilylpropyl urea and acetate compounds bound to the nucleus. For the alternative approach biotin was bound to the nanoparticle surface and incubated with cells stained with phalloidin-biotin and streptavidin. Through this method surface modifications dictate the uptake and binding of nanostructures to specific cell moieties. Alternatively, intracellular nanostructures have been shown as novel approaches for sensing and recording of cellular activity. Tian et al⁴¹ fabricated a flexible nanoscale SiNW field effect transistor capable of intracellular electrical recording in embryonic chicken cardiomyocytes. Cells were cultured on polydimethylsiloxane (PDMS) and placed over nanoproboscopes. Kinked SiNW were fabricated with nanoscale FET probes based on pressure and doping variation during synthesis. Then the surface of the probe was modified with a phospholipid bilayer to provide the potential for fusion with cell membranes. Steady intracellular electrical recordings from kinked nanowire FETs were successful first steps for novel recordings with high spatial and temporal resolution.

1.7.3 Tissue interfaces

Tissue interfaces provide a unique set of challenges for sensing and stimulation approaches to therapeutic applications. Development of better devices can provide precise medical data or alter tissue activity with electrical stimuli. The soft nature of tissues necessitates flexible and stretchable implantable devices. These devices face challenges that can interfere with high fidelity of recordings while under strain and biofouling at the interface. One consideration is the flexibility of tissues. The typical elastic modulus of cellular interfaces can be on the order of 1 Pa – 50 GPa with tissues often between 1 kPa to 100 kPa⁴²⁻⁴⁴, and specific situations such as wound healing can impact the modulus by up to a factor of five. In addition to this, tissues can have contractile activity. Implantation can affect this activity at the device tissue interface by impeding muscle contractions. Devices should be flexible so as not to impact regular tissue functioning and to prevent delamination from the tissue surface. Mechanical mismatch or device incompatibility can lead to immune responses at the device interface.

To address the mechanical mismatch at the tissue interface, high aspect ratio conductive CNTs were integrated into viscoelastic films.⁴⁵ Metal electrodes on elastomeric substrates typically fail at 10-20% strain due to cracks forming in the surface. Integrating CNTs provided the potential to bridge cracks formed under strain providing the potential for implanted devices with high stability under curvature and strain for device implantations. Implementation of this type of flexible device with CNTs in a flexible polymeric support⁷ were employed to record and stimulate chick retinas. This efficient neuronal stimulation from a flexible device overcame the tissue interface challenges. Alternative approaches have employed flexible silver – gold core – sheath nanowire composites⁴⁶ for electrophysiological recordings and thermal stimulation. For this device, gold coated nanowires of silver were embedded in a poly(styrene-butadiene-styrene)

elastomer. The high aspect ratio of the nanowires provided significant conductivity while the gold sheath protected the device from oxidation and made it biocompatible. The cardiac mesh was applied to the tissue of a swine heart to acquire ECG recordings from healthy and injured regions of an ischemic heart even under mechanical strain.

1.7.4 Environmental application interfaces

Nanomaterials have been implemented in a wide range of environmental applications including water remediation, biosensing, gas sensing and monitoring, and catalytic gas treatment.⁴⁷ The high surface area and radius of curvature improves reactivity compared to conventional techniques and the diverse morphologies provide potential for a range of purposes. The expansion of this technology is key becomes even more important when we consider the significant and ever increasing pollution and industrialization. The high surface area has been used in many applications, but this property of nanomaterials is especially useful in degrading and capturing pollutants in the water or air. The large radius of curvature produces a high density of atoms at the surface with low coordination making the materials more reactive. Degradation of water pollutants at surfaces has been accomplished with photocatalytic activity at nanostructured TiO₂ interfaces. The surfaces is very photoreactive with illumination producing redox reactions with water molecules and hydroxide ions adsorbed on the surface. The photocatalytic activity of TiO₂⁴⁸ with UV illumination was shown to be enhanced in the nanostructured form. Without this nanostructure the photocatalytic activity is minimal. Structure and particle shape and lattice defects are shown to be significant components in determining photocatalytic activity.⁴⁹ This photocatalytic activity can in turn break down organic contaminants in waste water treatment applications. Additionally, significant antimicrobial properties have been demonstrated at nanomaterial surfaces based on silver nanoparticles, titanium dioxide (TiO₂), and CNTs. Treating microbe contamination is a

challenge as antimicrobial resistance grows. Antimicrobial nanomaterials can be employed to treatment of drinking water contaminated with viruses or bacteria. Silver nanoparticles⁵⁰ have been used for antimicrobial activity, and this activity can be enhanced by the surface functionalization with cationic antimicrobial peptide ubiquicidin 29–41 through the NH₂ groups on the protein. The effects on bacterial growth of *Escherichia coli* and *Pseudomonas aeruginosa* were studied. This demonstrated the significant enhancement of the antimicrobial activity beyond the silver nanoparticles with the addition of the protein to the surface.

1.7.5 Nanomaterial water interfaces

There has been significant research into employing nanostructured surfaces for significantly altering water interfaces. Much of this work has centered on synthetic materials developed to take advantage of examples from naturally occurring nanostructures. Nanostructure roughness, morphology and chemical composition at the surface have been shown to be important factors in dictating this interface. These biomimetic structures have been utilized to produce materials with advanced anti-reflection structures, high adhesion, self-cleaning, wettability switching, and anti-icing properties.⁵¹ Some of the biggest biomimetic examples are lotus leaf with superhydrophobic properties and low adhesion, rose petals with superhydrophobic and high water adhesion, and butterfly wings with anisotropic super wetting.

The lotus leaf surface is one of the most commonly cited biomimetic examples. This is due to the highly superhydrophobic nature conferred by the micro and nanoscale hierarchal structure. The low adhesion on this surface results in small sliding angles where water at the surface easily slides off with minimal interaction due to nanopatterning. Superhydrophobic surfaces mimicking the hierarchal structure of lotus leaves was fabricated from a microsphere of polystyrene coated with a nanofibrous film of polystyrene.⁵² The nanofibers were approximately 420 nm with a high

aspect ratio and were randomly oriented across the surface. The combined microsphere and nanofiber structure produced a contact angle of 160.4° compared to the basic polystyrene film with a contact angle of 95.1° . This indicates the hierarchal structure produces the superhydrophobic film.

Rose petals also have a hierarchal structure, but compared to the effect of lotus leaf structures, the microscale papillae combined with nanofolds pins water droplets to the superhydrophobic surface. This prevents droplet sliding even in complete inversion. In one approach this rose petal structure was replicated using a UV nanomolding procedure in polyurethane acrylate⁵³ followed by a perfluoropolyether (PFPE) imprint leaving a PFPE micro- nanostructured hierarchal surface on a glass substrate. The calculated water contact angle was 144° with a hysteresis of 83° indicating a highly adhesive superhydrophobic surface.

Butterfly wings provide a directional sliding based on box like scales and a hierarchal structure with aligned nanogrooves. This oriented structure provides a biomimetic basis for liquid transportation. Synthetic anisotropic hierarchal surfaces mimicking the natural properties of the butterfly wings was produced by fabricating CNT coated microscales.⁵⁴ Curved CNT scales were produced by strain engineered CVD synthesis. The synthetic microscales are $70\ \mu\text{m}$ wide and $3\ \mu\text{m}$ thick. The CNT surfaces are then coated with a thin layer of thin hydrophobic polymer divinylbenzene because CNTs exhibit strong wetting and water wicking properties. This anisotropic surface provided a roll-off anisotropy of 6.2° . The potential to fabricate this type of structure with anisotropic wetting properties from CNTs indicates that additional properties of electrical conductivity and mechanical robustness could be incorporated in the future.

1.8 Thesis overview

In my thesis I will synthesize a range of previously unexplored materials via synthetic modifications and post synthetic modifications. I will report the characterization of atomic chemical variations at the surface via XPS and demonstrate the integration of XPS and UPS data to interrogate the effects of chemical and physical variation on surface band structure properties. We currently have a limited understanding of the physiochemical processes at the Si surface and the dependence of these processes on key properties at the different interfaces ranging from surface functionalization, chemical composition, or morphological variations. From this information the synthesis and post synthesis variations will enhance our understanding of the photoelectric and photoelectrochemical processes occurring at the nanostructure surfaces. From this analysis I will demonstrate these interface variations in a series of different applications with photoelectric, photoelectrochemical, and photothermal stimulation across the interface.

In Chapter 2, I will design materials with a variety of surfaces based on CVD synthesis modifications and then outline the method I applied to combine UPS and XPS analysis for identification of chemical variation and silicon band structure variation on the surface. The Si structures fabricated have very minor changes to the CVD process, but these small modifications produce significant alterations in the atomic composition of gold at the surface of the nanostructures. I identify several key CVD synthesis variations for tuning these properties; including shell ramping temperature and pressure, SiNW diameter, and phosphine doping. The impact of the shell growth conditions tailored the atomic percentage of gold from approximately 0% to almost 1% with no alterations in other properties. Both increasing SiNW diameter and increasing phosphine decreased atomic gold percentage at the SiNW surface predictably. From the analysis I identify the key components of band structure at the surface as they relate to binding

energy shift of the silicon peak in the XPS spectra and work function calculated from the secondary electron cutoff in the UPS spectra. I will show the application of this method to developing a range of Si nanostructures including coaxial p-i-n SiNWs with atomic gold integration during CVD growth and 3D patterning of atomic gold at the surface from a “coffee ring” like phenomenon based on the phosphine effects on the gold catalyst during CVD growth.

In Chapter 3, I will explore the post-synthesis surface modifications accessible for SiNWs after CVD growth. This approach relies on the surface chemistry of the nanostructures to tailor the surface for a range of applications. I employ the XPS analysis to characterize the success and extent of chemical reactions, identify alterations in chemical species on the SiNW surface, and determine the rearrangement of chemical species on the surface during the synthesis processes. In the first approach I will focus on two specific silicon reactions to functionalize the surface with compounds that will dictate the interaction of cells with the nanowire surface. This will specifically be focused on both a photodiode and an antibody each altering the SiNW interfaces with cellular systems. For each system the optical stimulation of structures is designed to alter cellular activity. The second approach will rely on metal assisted etching of the gold catalyst to introduce nanopores into the SiNW surface to enhance photothermal activity. We use XPS to characterize the alteration of chemical species on the surface with different etching methods to identify the changes in structures for photothermal stimulation of cells. In the third post synthesis modification the SiNWs are treated with various metals, Au, Ti, and Al, to alter Si solution interfaces for dictating photoelectrochemical properties at cellular interfaces. XPS analysis reveals the chemical rearrangement at the surface and the changes of surface electronic properties based on the metal – Si interface. Finally, I integrate gold nanomesh on a silicon surface by electroless deposition and track intermixing at the Au-Si interface between silicon and gold islands. This gold nanomesh

tailors the photoelectric properties of the silicon – solution interface and can significantly alter the photoelectric interaction at cell interfaces.

In Chapter 4, I will delve into the potential for silicon nanostructure interfaces to alter photolithography during polymer synthesis. I fabricate a heterogeneous structure with SiNWs integrated at a high density across an SU-8 polymer surface. This composite is patterned into a mesh structure by photolithography, but the SiNW interface demonstrates waveguiding properties that pattern nanoribbons of polymer in the window regions blocked to UV exposure. In a typical photolithographic patterning of mesh with no SiNWs there is no light present in window regions and as a result no nanoribbons form. The impact of these nanoribbons is that it supports a robust high-density mesh of SiNWs spanning the full window region. With this heterogeneous SiNW – Polymer composite I will demonstrate the evolution of novel properties resulting from the SiNW mesh including photoelectric effects, extreme flexibility and durability under stress, and increased water pinning and adhesion.

In Chapter 5, I will explore the SiNW – cellular interface by optically stimulating isolated neonatal cardiomyocytes. I demonstrate the ability to grow cardiomyocytes on a high density SiNW mesh and the presence of an extended SiNW-cell interface based on SEM and fluorescence microscopy. The cardiomyocytes are optically paced by a novel scanning based stimulation method that integrates a high speed focused laser spot scanned in the x-y direction with the waveguiding potential of a SiNW mesh for efficient stimulation of cardiomyocytes with low intensity laser stimulation. This mesh and stimulation are both demonstrated to be biocompatible by not inducing any significant amounts of cell death compared to cardiomyocytes grown on glass slides. Finally, I demonstrate the success of this low intensity x-y scanning – waveguiding based stimulation method for pacing cardiomyocytes and find key factors such as stimulation break time

for stability of cardiomyocytes at paced frequency for significant amounts of time after light stimulus is removed.

In Chapter 6, I apply the high-density SiNW mesh to optically stimulating tissue level interfaces. At this level mechanical properties of the mesh dominate the interface as water adhesion and structural stability under flexion dictate the effectiveness of optical stimulation. The water adhesion was used to wick the mesh to the tissue surface and the mechanical properties were used to adhere mesh to curvilinear tissue surface and undergo repeated beating stress without tearing. I demonstrate the stimulation of the heart tissue using the ex-vivo Langendorff method and optical illumination of the SiNW mesh – tissue interface. Through this photoelectric stimulation whole hearts were successfully paced to a range of stimulation frequencies. This method caused minimal tissue damage from laser stimulation.

In Chapter 7, I will utilize a porous foam synthesized from SiNWs to modulate water interfaces on the macroscale. Foams are synthesized from freeze patterning of SiNW suspensions in polyvinyl alcohol (PVA) followed by lyophilization to remove water and finally carbonizing to form a core of SiNWs glued together by a shell of carbon. The nanostructure and microstructure of this foam dictates the water interface switching from highly hydrophobic and water repulsive to hydrophobic with high water adhesion and finally to highly hydrophilic. From this minor variation significant changes in the water interface occur. I demonstrate an unexplored route for the production of biomimetic interfaces ranging from lotus leaf like water interaction; superhydrophobic and low adhesion, to rose petal like interfaces; superhydrophobic and high adhesion, based on hierarchical nanowire bundles. From this water interaction we can both produce novel materials for highly controlled water interface applications and more fundamentally tease out the contribution of structural and chemical effects dictating water interfaces. From this 3D

scaffold I demonstrate significant photothermal responses under laser illumination used for water boiling or ice melting at the foam water interface. Additionally, under significant laser intensity the photothermal properties are significant enough to burn off the carbon shell revealing a hydrophilic SiNW surface.

1.9 Bibliography

- 1 He, Y., Fan, C. & Lee, S.-T. Silicon nanostructures for bioapplications. *Nano Today* **5**, 282-295, doi:10.1016/j.nantod.2010.06.008 (2010).
- 2 Jeevanandam, J., Barhoum, A., Chan, Y. S., Dufresne, A. & Danquah, M. K. Review on nanoparticles and nanostructured materials: history, sources, toxicity and regulations. *Beilstein Journal of Nanotechnology* **9**, 1050-1074, doi:10.3762/bjnano.9.98 (2018).
- 3 Yang, H.-Y., Rho, W.-Y., Lee, K. S., Kim, H. S. & Hahn, Y.-B. TiO₂ Nanoparticles/Nanotubes for Efficient Light Harvesting in Perovskite Solar Cells. *Nanomaterials* **9**, doi:10.3390/nano9030326 (2019).
- 4 Dao, V.-D. & Choi, H.-S. Carbon-Based Sunlight Absorbers in Solar-Driven Steam Generation Devices. *Global Challenges* **2**, 1700094, doi:10.1002/gch2.201700094 (2018).
- 5 Baldrighi, M., Trusel, M., Tonini, R. & Giordani, S. Carbon Nanomaterials Interfacing with Neurons: An In vivo Perspective. *Frontiers in neuroscience* **10**, 250-250, doi:10.3389/fnins.2016.00250 (2016).
- 6 Mazzatenta, A. *et al.* Interfacing Neurons with Carbon Nanotubes: Electrical Signal Transfer and Synaptic Stimulation in Cultured Brain Circuits. *The Journal of Neuroscience* **27**, 6931, doi:10.1523/JNEUROSCI.1051-07.2007 (2007).
- 7 David-Pur, M., Bareket-Keren, L., Beit-Yaakov, G., Raz-Prag, D. & Hanein, Y. All-carbon-nanotube flexible multi-electrode array for neuronal recording and stimulation. *Biomedical microdevices* **16**, 43-53, doi:10.1007/s10544-013-9804-6 (2014).
- 8 Luo, X., Weaver, C. L., Zhou, D. D., Greenberg, R. & Cui, X. T. Highly stable carbon nanotube doped poly(3,4-ethylenedioxythiophene) for chronic neural stimulation. *Biomaterials* **32**, 5551-5557, doi:10.1016/j.biomaterials.2011.04.051 (2011).
- 9 Jan, E. *et al.* Layered Carbon Nanotube-Polyelectrolyte Electrodes Outperform Traditional Neural Interface Materials. *Nano Letters* **9**, 4012-4018, doi:10.1021/nl902187z (2009).
- 10 Park, S. Y. *et al.* Polarization-controlled differentiation of human neural stem cells using synergistic cues from the patterns of carbon nanotube monolayer coating. *ACS nano* **5**, 4704-4711, doi:10.1021/nn2006128 (2011).
- 11 Sharifi, S. *et al.* Toxicity of nanomaterials. *Chemical Society reviews* **41**, 2323-2343, doi:10.1039/c1cs15188f (2012).
- 12 Florence Mouchet, P. L., Elodie Sarremejean, Guillaume Bernard, Pascal Puech, Eric Pinelli, Emmanuel Flahaut, Laur yGauthier. Characterisation and in vivo ecotoxicity evaluation of double-wall carbon nanotubes in larvae of the amphibian *Xenopus laevis*. *Aquatic Toxicology* **87** (2008).

- 13 Julie Muller, F. H., Nicolas Moreau, Pierre Misson, Jean-François Heilier, Monique Delos, Mohammed Arras, Antonio Fonseca, Janos B. Nagy. Dominique Lison. Respiratory toxicity of multi-wall carbon nanotubes. *Toxicology and Applied Pharmacology* **207** (2005).
- 14 Yeh, Y.-C., Creran, B. & Rotello, V. M. Gold nanoparticles: preparation, properties, and applications in bionanotechnology. *Nanoscale* **4**, 1871-1880, doi:10.1039/C1NR11188D (2012).
- 15 Zhang, Y. *et al.* New Gold Nanostructures for Sensor Applications: A Review. *Materials (Basel, Switzerland)* **7**, 5169-5201, doi:10.3390/ma7075169 (2014).
- 16 Hu, R. *et al.* Core-Shell Magnetic Gold Nanoparticles for Magnetic Field-Enhanced Radio-Photothermal Therapy in Cervical Cancer. *Nanomaterials (Basel, Switzerland)* **7**, 111, doi:10.3390/nano7050111 (2017).
- 17 Blattmann, O. C. & Pratsinis, E. S. Single-Step Fabrication of Polymer Nanocomposite Films. *Materials* **11**, doi:10.3390/ma11071177 (2018).
- 18 Chidichimo, G. & Filippelli, L. Organic Solar Cells: Problems and Perspectives. *International Journal of Photoenergy* **2010**, doi:10.1155/2010/123534 (2010).
- 19 Wei, Z. *et al.* Semiconducting polymer-based nanoparticles for photothermal therapy at the second near-infrared window. *Chemical Communications* **54**, 13599-13602, doi:10.1039/C8CC07583B (2018).
- 20 Chiappini, C., Liu, X., Fakhoury, J. R. & Ferrari, M. Biodegradable porous silicon barcode nanowires with defined geometry. *Advanced functional materials* **20**, 2231-2239, doi:10.1002/adfm.201000360 (2010).
- 21 Kang, S.-K. *et al.* Dissolution Chemistry and Biocompatibility of Silicon- and Germanium-Based Semiconductors for Transient Electronics. *ACS Applied Materials & Interfaces* **7**, 9297-9305, doi:10.1021/acsami.5b02526 (2015).
- 22 Su, S. S. & Chang, I. in *Commercialization of Nanotechnologies—A Case Study Approach* (eds Dermot Brabazon *et al.*) 15-29 (Springer International Publishing, 2018).
- 23 H.-J., C. Vapor-liquid-solid growth of semiconductor nanowires. *NanoScience and Technology* **58**, 1-36 (2012).
- 24 Shao, M., Ma, D. D. D. & Lee, S.-T. Silicon Nanowires – Synthesis, Properties, and Applications. *European Journal of Inorganic Chemistry* **2010**, 4264-4278, doi:10.1002/ejic.201000634 (2010).
- 25 Langner, A. *et al.* Controlled Silicon Surface Functionalization by Alkene Hydrosilylation. *Journal of the American Chemical Society* **127**, 12798-12799, doi:10.1021/ja054634n (2005).
- 26 Khung, Y. L., Ngalim, S. H., Scaccabarozzi, A. & Narducci, D. Thermal and UV Hydrosilylation of Alcohol-Based Bifunctional Alkynes on Si (111) surfaces: How surface radicals influence surface bond formation. *Scientific reports* **5**, 11299-11299, doi:10.1038/srep11299 (2015).
- 27 Buriak, J. M. Functionalization of Silicon Surfaces for Device Applications. *JALA: Journal of the Association for Laboratory Automation* **4**, 36-39, doi:10.1016/S1535-5535-04-80009-1 (1999).
- 28 Bent, S. F., Kachian, J. S., Rodríguez-Reyes, J. C. F. & Teplyakov, A. V. Tuning the reactivity of semiconductor surfaces by functionalization with amines of different basicity. *Proceedings of the National Academy of Sciences* **108**, 956, doi:10.1073/pnas.1006656107 (2011).

- 29 Pasternack, R. M., Rivillon Amy, S. & Chabal, Y. J. Attachment of 3-(Aminopropyl)triethoxysilane on Silicon Oxide Surfaces: Dependence on Solution Temperature. *Langmuir* **24**, 12963-12971, doi:10.1021/la8024827 (2008).
- 30 Abdelhameed, M. *et al.* Tuning the Optical Properties of Silicon Quantum Dots via Surface Functionalization with Conjugated Aromatic Fluorophores. *Scientific Reports* **8**, 3050, doi:10.1038/s41598-018-21181-8 (2018).
- 31 Cui, H. *et al.* Near-infrared (NIR) controlled reversible cell adhesion on a responsive nanobiointerface. *Nano Research* **10**, 1345-1355, doi:10.1007/s12274-017-1446-1 (2017).
- 32 Tian, B. *et al.* Coaxial silicon nanowires as solar cells and nanoelectronic power sources. *Nature* **449**, 885, doi:10.1038/nature06181 (2007).
- 33 Ohkura, Y., Weisse, J. M., Cai, L. & Zheng, X. Flash Ignition of Freestanding Porous Silicon Films: Effects of Film Thickness and Porosity. *Nano Letters* **13**, 5528-5533, doi:10.1021/nl403114g (2013).
- 34 Zhao, X., Zhang, Q., Chen, D. & Lu, P. Enhanced Mechanical Properties of Graphene-Based Poly(vinyl alcohol) Composites. *Macromolecules* **43**, 2357-2363, doi:10.1021/ma902862u (2010).
- 35 K. Thanigai Arul, E. M., P. P. Murmu, J. Kennedy, M. Henini. Enhanced magnetic properties of polymer-magnetic nanostructures synthesized by ultrasonication. *Journal of Alloys and Compounds* **720**, 395-400 (2017).
- 36 Hanson, L., Lin, Z. C., Xie, C., Cui, Y. & Cui, B. Characterization of the Cell–Nanopillar Interface by Transmission Electron Microscopy. *Nano Letters* **12**, 5815-5820, doi:10.1021/nl303163y (2012).
- 37 Santoro, F. *et al.* Revealing the Cell–Material Interface with Nanometer Resolution by Focused Ion Beam/Scanning Electron Microscopy. *ACS Nano* **11**, 8320-8328, doi:10.1021/acsnano.7b03494 (2017).
- 38 Parameswaran, R. *et al.* Photoelectrochemical modulation of neuronal activity with free-standing coaxial silicon nanowires. *Nature Nanotechnology* **13**, 260-266, doi:10.1038/s41565-017-0041-7 (2018).
- 39 L West, J. & Halas, N. *Applications of nanotechnology to biotechnology - Commentary*. Vol. 11 (2000).
- 40 Bruchez, M., Moronne, M., Gin, P., Weiss, S. & Alivisatos, A. P. Semiconductor Nanocrystals as Fluorescent Biological Labels. *Science* **281**, 2013, doi:10.1126/science.281.5385.2013 (1998).
- 41 Tian, B. *et al.* Three-Dimensional, Flexible Nanoscale Field-Effect Transistors as Localized Bioprobes. *Science* **329**, 830, doi:10.1126/science.1192033 (2010).
- 42 Rivnay, J., Wang, H., Fenno, L., Deisseroth, K. & Malliaras, G. G. Next-generation probes, particles, and proteins for neural interfacing. *Science Advances* **3**, e1601649, doi:10.1126/sciadv.1601649 (2017).
- 43 Butcher, D. T., Alliston, T. & Weaver, V. M. A tense situation: forcing tumour progression. *Nature Reviews Cancer* **9**, 108, doi:10.1038/nrc2544 (2009).
- 44 Cox, T. R. & Erler, J. T. Remodeling and homeostasis of the extracellular matrix: implications for fibrotic diseases and cancer. *Disease Models & Mechanisms* **4**, 165, doi:10.1242/dmm.004077 (2011).
- 45 Hu, L., Yuan, W., Brochu, P., Gruner, G. & Pei, Q. Highly stretchable, conductive, and transparent nanotube thin films. *Applied Physics Letters* **94**, 161108, doi:10.1063/1.3114463 (2009).

- 46 Choi, S. *et al.* Highly conductive, stretchable and biocompatible Ag–Au core–sheath
nanowire composite for wearable and implantable bioelectronics. *Nature Nanotechnology*
13, 1048-1056, doi:10.1038/s41565-018-0226-8 (2018).
- 47 Ren, Z., Guo, Y., Liu, C.-H. & Gao, P.-X. Hierarchically nanostructured materials for
sustainable environmental applications. *Frontiers in Chemistry* 1, 18 (2013).
- 48 Nasikhudin, Diantoro, M., Kusumaatmaja, A. & Triyana, K. Study on Photocatalytic
Properties of TiO₂ Nanoparticle in various pH condition. *Journal of Physics: Conference*
Series 1011, 012069, doi:10.1088/1742-6596/1011/1/012069 (2018).
- 49 Rickerby, D. G.
- 50 Morales-Avila, E. *et al.* Antibacterial Efficacy of Gold and Silver Nanoparticles
Functionalized with the Ubiquicidin (29–41) Antimicrobial Peptide. *Journal of*
Nanomaterials 2017, 10, doi:10.1155/2017/5831959 (2017).
- 51 Wen, G., Guo, Z. & Liu, W. Biomimetic polymeric superhydrophobic surfaces and
nanostructures: from fabrication to applications. *Nanoscale* 9, 3338-3366,
doi:10.1039/C7NR00096K (2017).
- 52 Jiang, L., Zhao, Y. & Zhai, J. A Lotus-Leaf-like Superhydrophobic Surface: A Porous
Microsphere/Nanofiber Composite Film Prepared by Electrohydrodynamics. *Angewandte*
Chemie 116, 4438-4441, doi:10.1002/ange.200460333 (2004).
- 53 Soyoung Choo, H.-J. C., Heon Lee. Replication of rose-petal surface structure using UV-
nanoimprint lithography. 121, 170-173 (2014).
- 54 Zhao, H. *et al.* Synthetic Butterfly Scale Surfaces with Compliance-Tailored Anisotropic
Drop Adhesion. *Advanced Materials* 31, 1807686, doi:10.1002/adma.201807686 (2019).

Chapter 2 : XPS and UPS characterization of variability in SiNW surfaces during CVD synthesis; surface chemical composition and band structure

2.1 Introduction

The field of nanomaterials has had a drastic increase in variety and has been applied to almost every field of research due to the potential for the ability to produce novel properties from materials with a known set of properties. Silicon nanomaterials specifically have significant potential in this area. Silicon nanomaterials can take advantage of the many functions of semiconductors including light absorption over a range of wavelengths, tunable doping profile, biocompatibility, chemical reactivity, demonstrated photovoltaic and photothermal applications. SiNWs are especially interesting in this regard due to their high surface area and high aspect ratio. As we shrink these materials to the nanoscale a new set of properties evolve including increased surface area, band bending, surface dipole, and more. The main focus of the previously developed structures has resulted in extensive research into the ability to tailor morphologies of nanostructures including dopant modulation¹, core-shell SiNWs², SiNW diameter and tapering³, kinked SiNWs⁴⁻⁶, barbed structures⁷, crystal phase engineering⁸, twin plane defect⁹, gold incorporation¹⁰. For this work we take a more in depth examination of the surface properties that can be employed to tailor structures through either synthetic modifications or post-synthesis modifications. From this analysis we will have a set of design principles to apply nanostructures to biological structures, photovoltaics, polymers, or energy applications by modifying surface properties to tune these interfaces.

Here we examine a range of silicon nanostructures to get an understanding of how the CVD synthesis process impacts these nanomaterials and how small modifications can result in significant changes. We focus on core-shell silicon nanowire structures as they provide the most significant way to drastically alter surface properties with no changes to bulk core structure. This

comes with a focus p-type/intrinsic/n-type (PIN) SiNW structures. This is fabricated from the growth of a p-type core NW grown via the VLS method and two shells of intrinsic and then n-type silicon grown via VS method. We focus on this structure because the PIN shell structure establishes a coaxial PIN diode which has been demonstrated to have a photoelectric response under illumination². This results from the photogenerated carriers produced under light where electrons are swept by the built in electric field towards the n-type shell while holes are pushed towards the p-type core. Previously we have demonstrated the potential for these wires to serve in everything from photoelectric energy generation capacity as well to the stimulation of cellular components at biological-nanowire interfaces. With this previously demonstrated work and the potential for significant variations within this general structure, we can open up a new field of structures more specifically applied to a wider range of applications.

2.2 Results and Discussion

2.2.1 Employing CVD synthesis to alter chemical composition and band structure at the surface of silicon nanostructures

The CVD process confers a high level of control over the synthesized silicon nanostructures including the diameter, length, dopant profile, and more. With the vapor liquid solid (VLS) and vapor solid (VS) growth processes, structures such as core shell coaxial SiNWs and silicon membrane are able to be synthesized. The use of gold as the liquid metal alloy can result in significant variation in surface chemistry. We explored the range of variations that can be employed during the CVD growth process of core shell SiNW structures including temperature, pressure, doping, and diameter. We synthesized this series of SiNWs and analyzed the effects on the surface via Photoelectron Spectroscopy (PES). Through this analysis we

identify the potential to modify the gold concentration at the surface shifting between 0.01% - 1% atomic percentage of gold at the surface. We verify the effects of phosphine doping on the gold diffusion process resulting from the strong interaction between phosphine with both gold and silicon. In addition to this, we identify silicon nanostructure diameter as a key parameter impacting surface structures. From this analysis we are able to target synthetic conditions that are key for altering silicon nanostructure properties to develop new nanostructures. This type of analysis will also be key for more specifically matching nanostructures to desired applications for stimulation or sensing. With the ability to control the ratio and density of Au decorating the surface of silicon nanostructures we are able to identify multiple species of Au from (a) gold in metallic environments (Au bonded predominantly to other Au atoms), (b) gold in nanoclusters of Au or at a surface (with dangling bonds or surface states), (c) gold in isolated atomic form (Au predominantly bonded to Si).

Previous XPS studies have shown that we can tune the character of the surface chemical and elemental composition, with in increasing metallic character of bonding with increased coverage of Au forming Au-Si bonds.¹¹ With the method applied here using a combination of XPS/UPS we outline the physical basis, specifically chemical composition and morphological changes controlled during synthesis, to understand how this impacts electronic structure of materials at the surface. XPS interrogates the chemical composition of surface of materials up to 10 nm specifically the core electrons. UPS provides information about the electronic structure of the valence band structure sampled from the top 2-3 nm of the material.

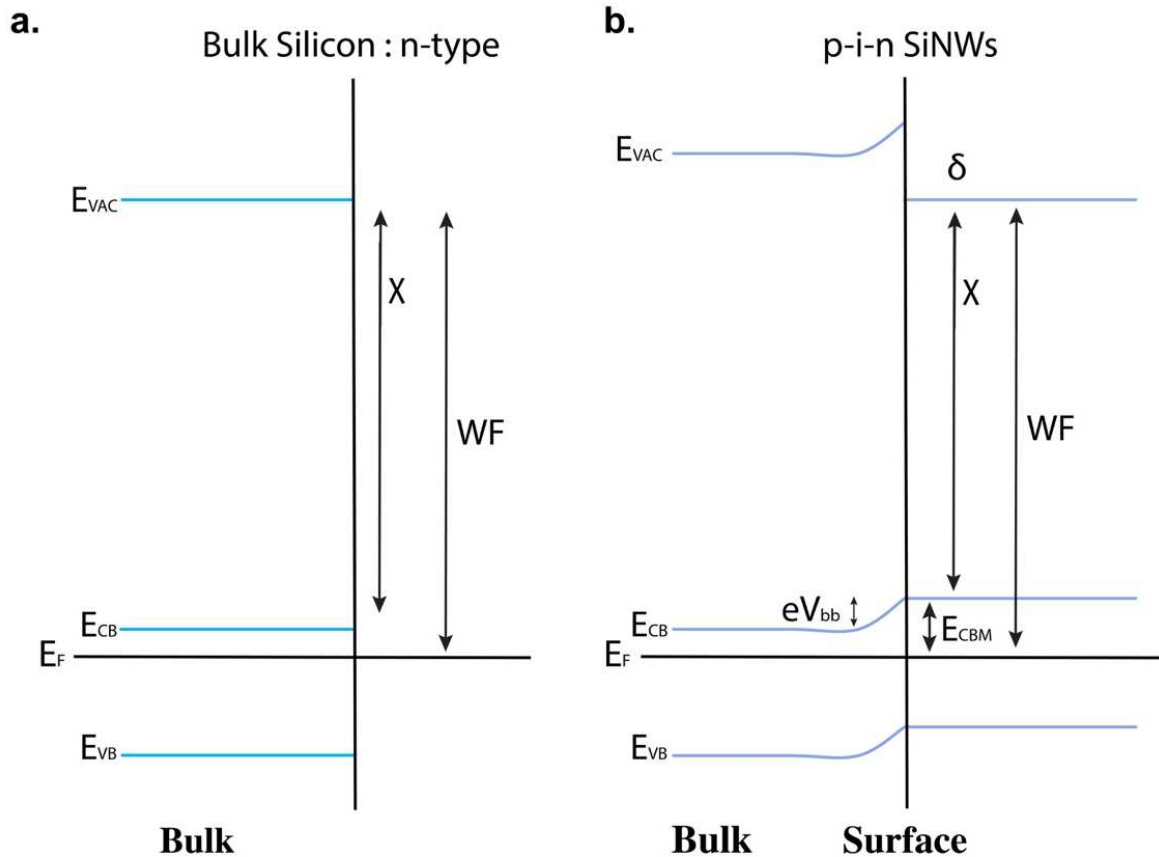


Figure 2-1. Energy band structure of the silicon – vacuum interface. **a.** The diagram of the bulk structure of n-type silicon is calculated for flat band values. The theoretical calculations are based on doping ratio, electron affinity (X), and band gap (E_g) **b.** Band diagram for PIN SiNWs based on the n-type bulk diagram with values calculated from XPS and UPS analysis. The calculated values for band bending (bb), surface dipole (δ), and work function are integrated into the theoretical band diagram. This analysis integrates measured values for the effects of the surface at the silicon – vacuum interface.

For this analysis we compare membranes vs nanostructures, doping, and gold incorporation. To understand this we need to characterize the bandgap, absolute position of the fermi level, the valence band edge, the conduction band edge, distribution of gap states. Information about the energy band structure will be useful for fundamentally understanding how nanostructure properties are dependent on key surface properties and additionally will be important to experimentally characterize the properties of different Si nanomaterials to make them successful or useful for a wide range of applications. (Figure 2-1)

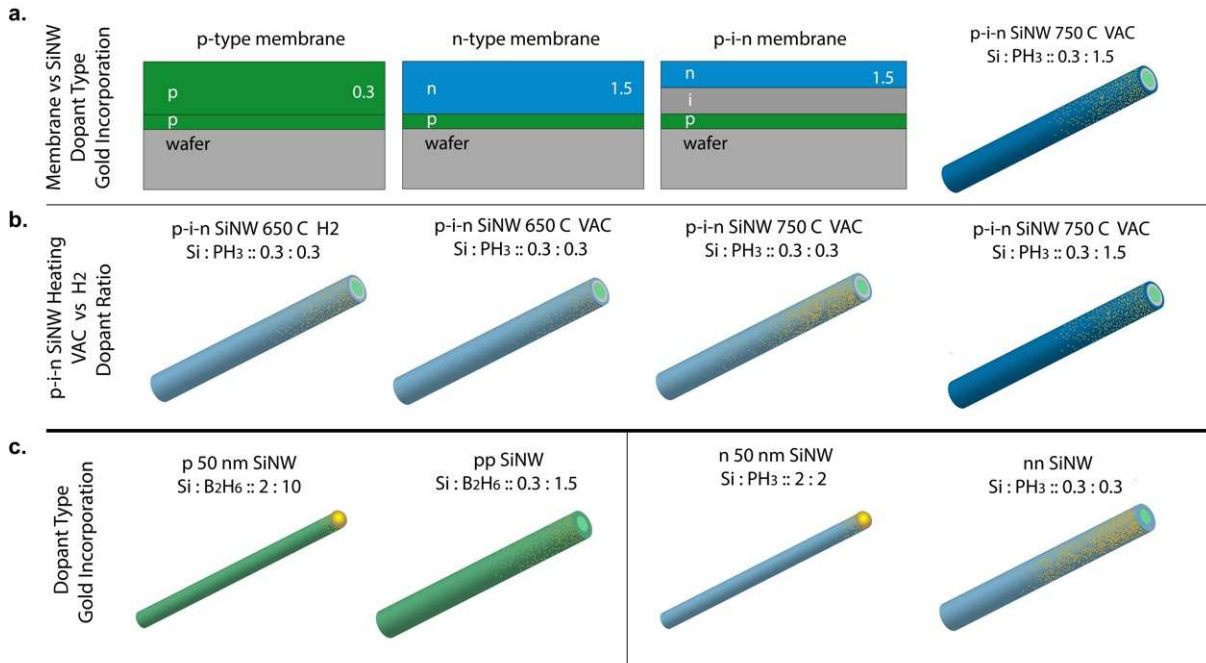


Figure 2-2. Platform of materials synthesized by CVD for XPS and UPS analysis. **a.** This includes structures of p-type (green), n-type (blue), and p-i-n membranes grown via VS on SOI (silicon on insulator) wafers. Membranes serve as a control for nanostructure variations to ensure surface structure does not alter analysis method. **b.** In the second analysis set five different types of PIN SiNWs are compared focusing on samples with a range of CVD growth conditions including 750 °C vs 650 °C and under hydrogen or vacuum with varied gold atomic ratios. These samples are compared to large diameter wires and wires with high doping ratios (dark blue). **c.** For the final set of samples core vs core-shell SiNWs are compared for p-type (green) and n-type (blue) SiNWs.

With the method applied here using a combination of XPS/UPS we outline the chemical composition and morphological changes controlled during synthesis, to understand the physical basis for changes that impact electronic structure of materials at the surface. (Figure 2-2) XPS interrogates the chemical composition of surface of materials up to 10 nm to specifically examine the core electrons. UPS provides information about the electronic structure of the valence band sampled from the top 2-3 nm of the material. This work will help us (a) establish a protocol based on PES to characterize our nanomaterials for a range of CVD variations (figure 2-3), (b) which could be applied to fundamentally understanding electronic properties of silicon nanostructures and how they interface with their environment, and (c) rationally design a wider range of nanomaterials where surfaces dominates the material properties such as 0D (nanoparticles,

quantum dots, Nano lenses), 1D (nanowires, nanorods, nanotubes, SiNWs CNTs), 2D nanosheets (membranes, coatings, graphene) and more.

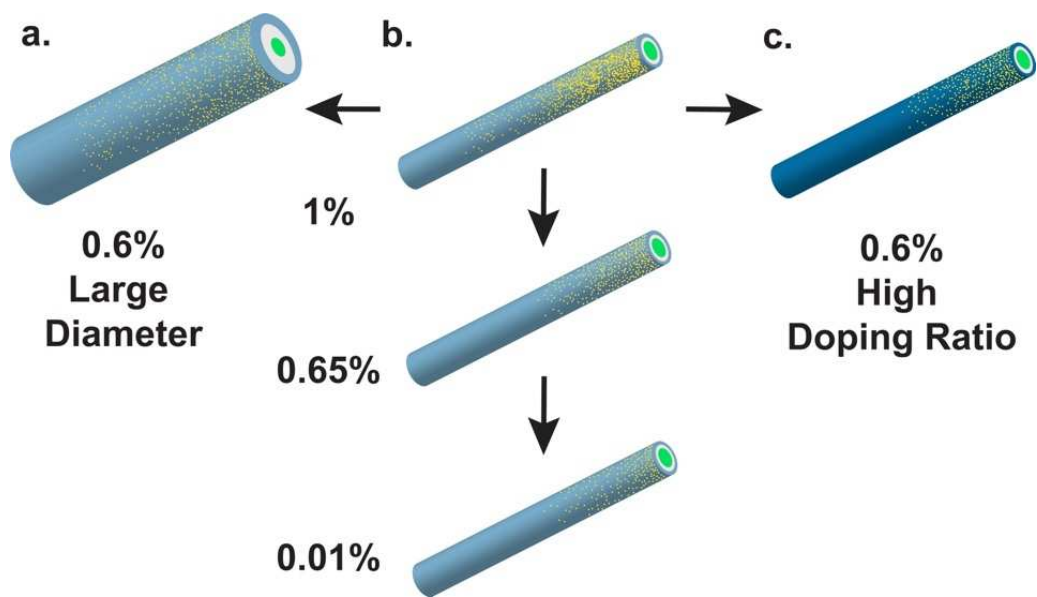


Figure 2-3. Central XPS and UPS analysis scheme. **a.** Large diameter wires are compared to **b.** SiNWs with varied gold percentages at the surface. The focus of this analysis is based on PIN SiNWs with varied shell ramping conditions. (light blue) This results in atomic gold ranging between 0.01% Au – 1% Au at the surface. **c.** This is then compared to and SiNWs and high phosphine doping ratio SiNWs. (dark blue). This allows for study of both gold ratio variations resulting of CVD tuning.

2.2.1.1 Gold diffusion process

Gold incorporation is an inevitable part of SiNW growth via CVD. For SiNW grown via the VLS method the majority of the gold is trapped in the AuNP. This ratio of atomic incorporation via this process is small and highly dependent on growth conditions and dopant concentration. High temperature growth at low pressure results in diffusion of the gold nanoparticle down the sidewalls. The growth of VLS core wires results in minimal amounts of contamination down the surface of the wire as gold atoms can be left behind during the wire elongation process. This can activity can be enhanced through high phosphine doping and large wire diameter.^{7,10}

XPS survey spectra were used to calculate the atomic ratio of both Carbon and Gold atoms on the surface of the SiNWs. Sample preparation was conducted prior to XPS and UPS collection

and samples were cut and loaded in the clean room to minimize carbon contamination and carbon over-layer growth which is detrimental especially for UPS data collection. For all samples the XPS survey spectra was used to calculate the atomic ratio of Si : C to ensure this value was below 10%.

The gold contamination at the surface of the SiNW can be significantly enhanced by vacuum or high temperatures during the growth process. This is especially prominent during the VS shell growth process. During the growth of the shells gold floats to the surface resulting from high diffusivity of gold in silicon at high temperatures or low pressures. We explore the variation in gold species at the surface of the silicon by fitting gold peaks based on sputter cleaned gold control samples. We compare core n-type SiNWs to core-shell n-type SiNWs to identify the shift from metallic gold at 84 eV to atomic or gold silicide species closer to 86 eV. (Figure 2-4 a-b) The fitting of these gold peaks is determined by the full width half max (FWHM) of the gold control peak and ensuring that fitted peaks are no more than double that size. The shift of the metallic peak is set below 84.1 eV based on the gold control samples. XPS Au 4f spectra (Figure 2-4) contains the peak analysis of gold for an n-type core SiNW grown via VLS demonstrating that the majority of the Au present in the sample is trapped in the 50 nm AuNP cap with a portion of the Au atoms shifted to higher energy due to their presence at the AuNP surface.¹²⁻¹⁴ To verify the fitting of each sample is appropriate, we plot the shift of Au peaks for each sample and verify that each peak falls within the desired range. (Figure 2-4 d) Additionally, we use XPS analysis to calculate the atomic ratio of gold at the surface of the SiNWs with varied temperatures and pressures during the ramping process.

Sample Type	Dopant	C Ratio (Si : C)		Au Ratio (Si : Au)	
		Average	Stdev	Average	Stdev
p	10 sccm	6.58	0.00	0.03	0.00
pp	1.5 sccm	4.34	1.79	0.00	0.00
p membrane	1.5 sccm	6.35	0.99	0.00	0.00
n	2 sccm	5.92	0.00	0.28	0.00
nn	0.3 sccm	3.63	1.20	2.01	0.04
n membrane	1.5 sccm	7.45	1.02	0.00	0.00
pin membrane	1.5 sccm	5.98	1.88	0.00	0.00
pin 750 Vac	1.5 sccm	6.85	1.62	0.56	0.54
pin 750 VAC 1 um	0.3 sccm	7.61	0.54	0.57	0.36
pin 750 VAC	0.3 sccm	5.64	2.13	0.94	0.52
pin 650 : VAC	0.3 sccm	5.86	1.81	0.02	0.01
pin 650 : H2	0.3 sccm	5.32	2.73	0.65	0.18

Table 2-1. Ratios of elemental composition calculated from XPS data. Carbon and gold ratios were calculated using the survey spectra. For each element the ratio is compared to the silicon signal to keep a consistent reference. All carbon ratios are between the range of 3.6-7.6%. Minimal carbon contamination is key for quality of data. The gold ratio provides information about the chemical composition that is key to understanding changes in the surface electronic structure.

Atomic ratios of Au : Si were also calculated from XPS survey spectra (Table 2-1, Figure 2-4) and this data provided insight into the elemental variation at the SiNW surface resulting from synthetic variation. The synthetic conditions during shell growth 650°C or 750°C and ramped under H₂ or Vacuum with both affecting gold diffusion. Figure 3d shows the effect of this variation (a) 650°C + Vac, (b) 650°C + H₂, (c) 750°C + Vac with increasing Au% at the surface. The effect of SiNW diameter was explored by comparing 750°C + Vac at 200 nm vs 1000 nm. The larger diameter SiNWs in this condition present about 50% less Au atomic percentage at the surface. This variation is likely a result of a static starting AuNP size of 50 nm and an increase in SiNW surface altering the ratio of Au : Si atoms at the surface. The final condition examined was doping ratio for SiNWs 750°C + Vac with either 0.3 sccm phosphine or 1.5 sccm phosphine for the n-type shell synthesis. The results show that the 5x increase in flow rate of phosphine resulted in a significant

drop in Au atomic percent at the surface from 1% to 0.01%. Samples were prepped under 750°C significantly facilitating Au diffusion down the surface of the wire. The effect of the increased phosphine ratio is likely a result of a lowered mobility of Au atoms preventing them from floating to the surface as seen with 0.3 sccm samples.¹⁰ With the ability to control the ratio and density of Au decorating the surface of silicon nanostructures we are able to identify multiple species of Au from (a) gold in metallic environments, 84 eV, (Au bonded predominantly to other Au atoms), (b) gold in nanoclusters of Au 85 eV or at a surface of NP (with dangling bonds or surface states), and (c) gold in isolated atomic form, 86 eV (Au predominantly bonded to Si). Analysis of p-i-n SiNWs (Fig 2-4) shows similar peak distributions for all synthetic variations, but showed significant variation in atomic ratio of Au : Si at the surface. The variations in Au atoms at the surface result from conditions during shell growth, SiNW diameter, and dopant ratio.

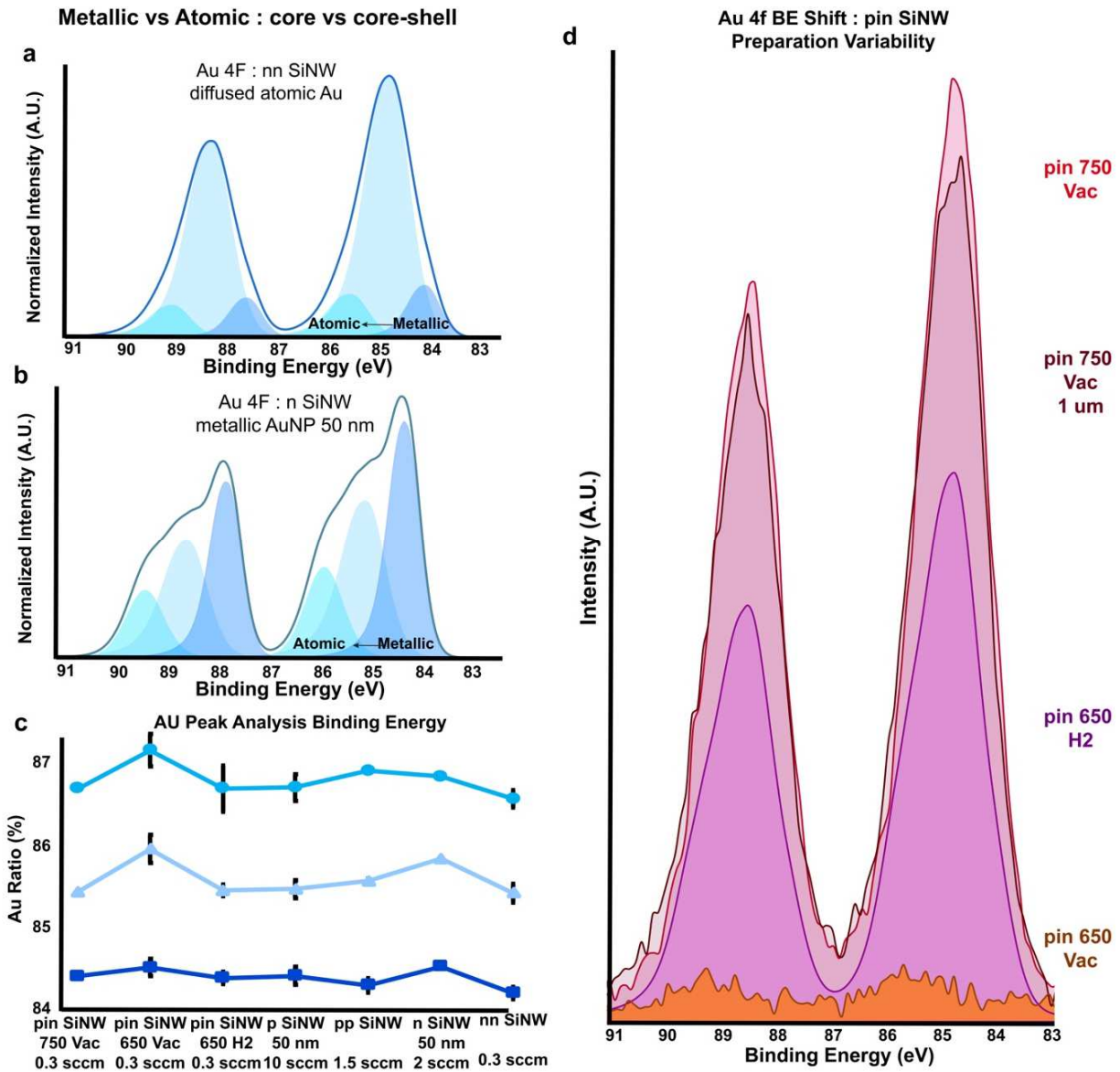


Figure 2-4. Gold XPS peak analysis and chemical identification. The gold chemical identification is verified by comparing core and core shell SiNWs (**a and b**) For core-shell n-type samples **a**, the gold 4f peak is shifted to binding energies significantly higher than the 84 eV of metallic gold. This results in predominant peaks of light blue due to gold silicide formation. In comparison **b**, core samples with a metallic gold cap and minimal gold silicide contamination. This results in the predominant peak as the dark blue metallic peak at 84 eV). **c**, The focus of this analysis is verifying that the gold peaks are fitted appropriately. The shift of each peak is plotted for each sample indicating that gold, gold silicide, and atomic gold peaks are all within the desired shift range. **d**, Gold intensity for the PIN SiNW samples are compared by plotting gold peaks for the SiNW samples with a range of synthetic conditions. While samples shift between 0.01% - 1% Au : Si, the gold peak shifts are all similar indicating that the gold species present are in the form of gold silicide with the main variation just being atomic ratio and not species.

2.2.1.2 XPS chemical analysis

Binding energy shifts for Si 2p spectra from XPS data collection shown in Figure 2-5 indicate changes in the electronic structure at the surface because photoelectrons calculated for XPS measurements are produced from the surface space charge region.¹⁵ The spectra shown in Figure 2-5 are representative of the XPS core level Si 2p signal for p-type, n-type, and p-i-n membranes. These samples were prepared via VS silicon growth (Figure 2-5) and have no Au incorporation required for growth as is key to the SiNW growth. This membrane comparison serves as a control for identifying the effect of dopants on Si 2p shift. The n-type membrane of p-i-n growth is significantly larger than 10 nm thick and XPS samples approximately the top 10 nm. Figure 3a spectra indicates that as expected p-i-n samples are consistent with n-type samples with identical doping profiles. To verify consistency between samples FWHM was measured and identified to be all within a range of 0.7 eV well within the range of literature values.^{15,16}

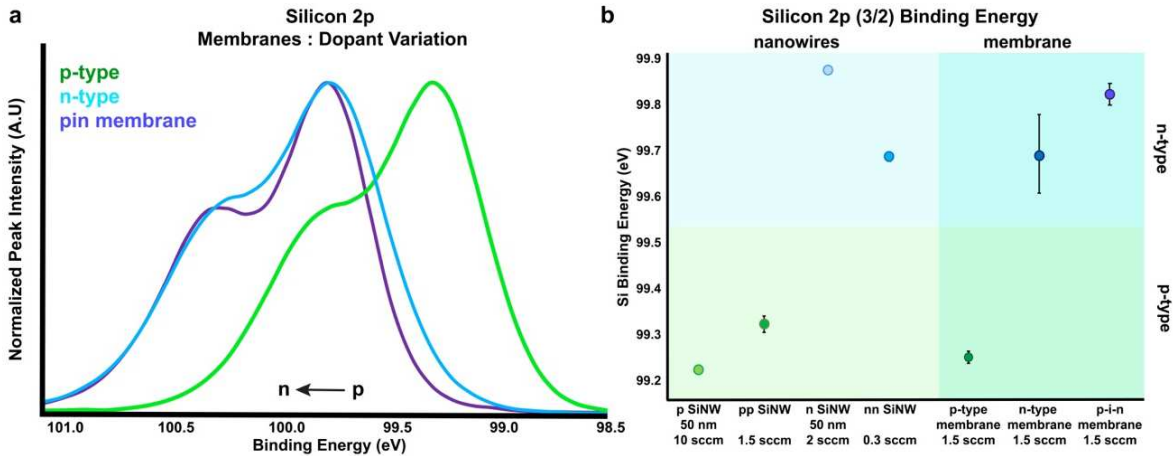


Figure 2-5. Silicon peak shift comparison for doping variation and structure. **a.** Silicon peak values for p-type (green), n-type (blue), and pin membrane (purple) are plotted to identify the effect of doping on the band bending of the material. This shift falls within the expected range. **b.** The comparison of p-type and n-type membrane and nanostructure samples indicated that the surface structure does not significantly alter the analysis method. Samples of the same doping do not shift from predicted ranged by the addition of the nanostructured texture.

As demonstrated by the graph in Figure 2-5, for all samples p-type silicon is about 0.5 eV lower BE than n-type samples, consistent with literature values.¹⁵ This is a result of the fact that at the n-type silicon interface the charge carriers at the surface are depleted in comparison to bulk resulting in a net positive charge in this depletion region. Due to the effect of this space charge region, photoelectrons from electron deficient interfaces of n-type samples requires a larger energy to remove electrons due to higher screening. These binding energy differences reflect the upward band bending at n-type interfaces and downward band bending at p-type interfaces.

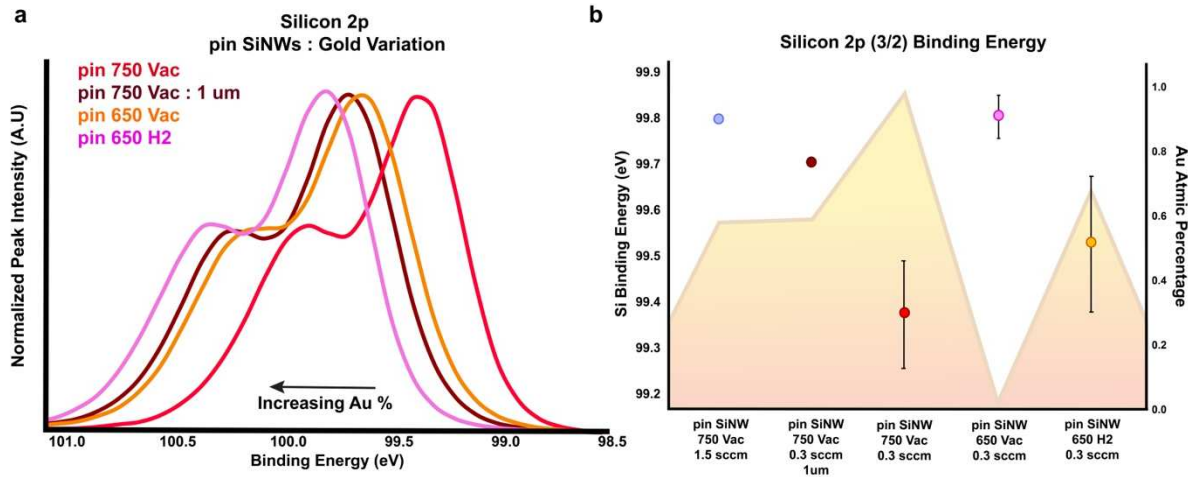


Figure 2-6. Silicon peak shift comparison for PIN SiNWs. a. Silicon peak values for PIN structures with a range of gold ratios indicates that the binding energy of the Si 2p 3/2 peak shifts predictably based on gold percentages. b. Graph demonstrates the shift in binding energy for SiNW samples plotted against Au : Si atomic ratios (yellow mountain plot)

Examining the effect of Au incorporation at the surface of the SiNW based on temperature and pressure during synthesis Figure 2-6 shows that SiNWs shift to higher BE with lower Au incorporation percent. For the growth of p-i-n core shell SiNWs the core is grown via VLS method and subsequent shells are grown via VS deposition. For the shell growth samples are heated to higher temperatures (650°C or 750°C) appropriate for VS deposition. This ramp from VLS temperature to VS temperatures can be done under H₂ or Vacuum. We have previously shown the presence of this atomic gold at the surface of p-i-n SiNW.¹⁷ Figure 2-6 also indicates that variations

in elemental surface composition of p-i-n SiNWs is one key lever for altering Si 2p elemental shift. The shifts of p-i-n SiNWs fall within the expected range of n-type surfaces 99.64 eV +/-0.18. Within this range BE is shifted by Au percent incorporation, doping ratio, and SiNW diameter indicating that these synthetic variations can be used to tailor surface band bending effects of SiNW.

SiNW diameter variation (Figure 2-6) is the second parameter for altering surface electronic properties. SiNWs with increased NW diameter (250 nm vs 1 μ m) the Au atomic percentage at the surface drops about 50% and BE shifts about 0.3 eV higher. This follows the trend of Au atomic % at the surface, but is likely resulting instead from travel of Au to the surface but rather a result of the increased size of the NW in comparison to the same number of Au atoms in the Au cap on each wire. The final synthetic variation examined was doping ratio with either 0.3 sccm (low) and 1.5 sccm (high). Higher doping ratio reduces the Au atomic percentages at the surface about 50%, and shifts the BE to about 0.45 eV higher. This indicates that in addition to the Au% at the surface varying doping ratio is a significant factor in determining shift in BE is the doping. With the large diameter (1 μ m) SiNW a similar Au atomic percentage was present at the surface, but the BE was shifted to a higher eV for the higher (1.5 sccm) SiNW. This is consistent with the trend of more electron deficient surfaces increasing BE of Si 2p peaks.

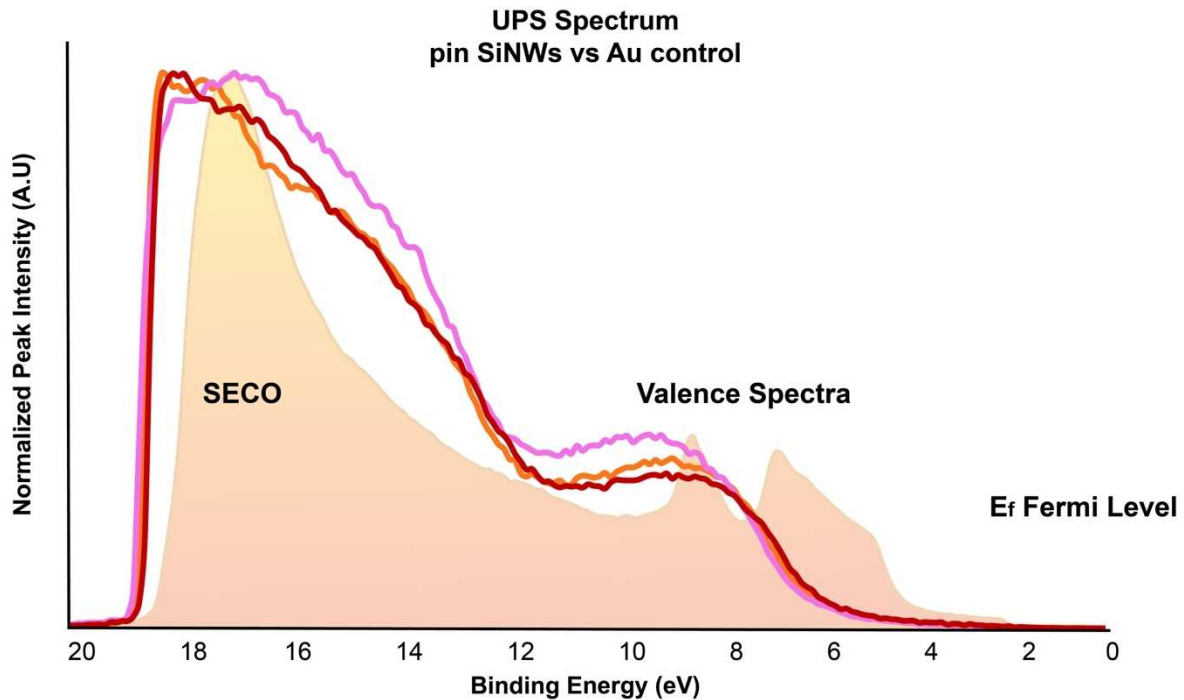


Figure 2-7. Full UPS spectra reveals three different regions of analysis for nanostructures. Graph demonstrates the three key regions including secondary electron cutoff (SECO), valence band, and fermi level (E_f). Red, orange, and pink traces indicate PIN SiNWs and orange plot represents gold control. The SECO of gold control sample is shifted to higher BE based on metallic nature of sample. The effect of the gold variation at the surface of the SiNWs causes significant shift in SECO, but samples fall within the semiconductor range.

2.2.1.3 UPS data provides work function analysis

Work function results from both the band bending information at the interface and surface electrostatics, or the dipole effects. The wide UPS spectrum (Figure 2-7) contains three main regions for extracting information about the valence band data of the materials interface. The first region (I) is the secondary electron cutoff (SECO) where the energy of the electrons is not large enough to overcome the energy of the work function and escape the material for calculation. The SECO is then used to calculate the work function of the sample by subtracting this value from the energy ($h\nu = 21.21$ eV). In the second region (II) the density of states of the valence band spectra is illuminated. Silicon has a broad density of states between 3-4 eV. The addition of significant portions of gold evolves clear valence band spectra peaks similar to what is seen with pure gold

control. The final region (III) at the fermi edge can indicate the shift to a metallic state. This curve can be shifted by the addition of a metallic gold layer through sputter coating.

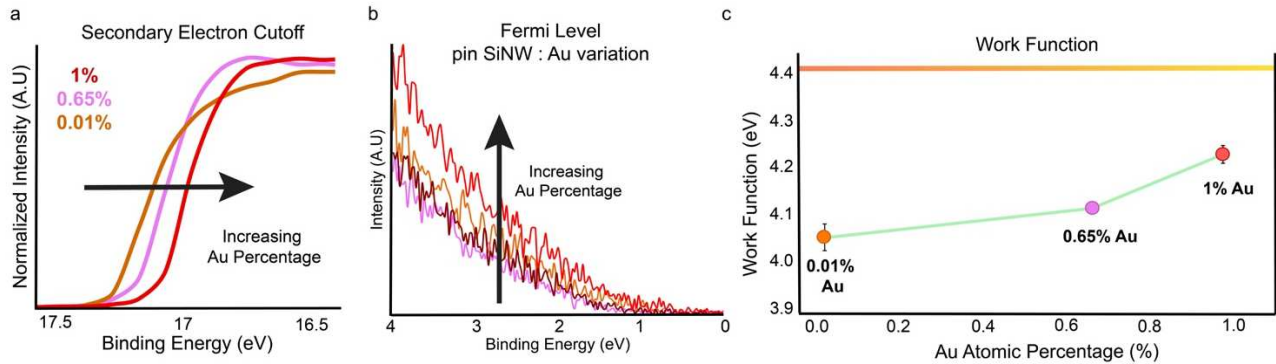


Figure 2-8. In-Depth examination of SECO and fermi level. **a.** The SECO for samples with a range of gold percent at the surface shifts to lower binding energies with higher gold incorporation. From the SECO the WF value is calculated. **b.** The fermi level provides information about the electron density close to the fermi level of the material. For metallic samples, there is a stepwise change indicating a high electron density at the fermi level. The PIN SiNW samples have a semiconductor like structure with a decay to 0. **c.** The calculated work function of the SiNW samples is compared to the work function of the sputter cleaned gold control. This indicates that increasing gold atomic percentages on the SiNWs shifts the work function towards but not at the work function of gold (yellow bar).

Previous studies have indicated that electron rich interfaces (n-type compared to p-type) or surface modifications resulting in more electron rich interfaces shift SECO to higher eV. The trend seen in Figure 2-8 of pin SiNWs with varied Au incorporation (0.2% - 1%) at the surface shifts SECO to lower BE, closer to Ar ion sputter cleaned Au control sample. This results in effectively increasing work function with the addition of gold at the NW surface towards but not at the measured level of the Au sample at 4.41 eV. Examining the larger diameter SiNWs, Figure 4b shows that the 1000 nm SiNWs are shifted to higher eV for SECO compared to the 200 nm SiNWs. The large diameter wires, as shown previously, have about 50% less atomic ratio of gold as compared to the surface of the smaller diameter wires. The SECO value for large diameter wires significantly varies from the trend of the percentage gold atoms at the surface indicating that diameter has a more significant contribution to the SECO and resulting work function. For the

final variation, higher dopant density for n-type wires makes for a more electron rich interface this trend is supported by the shift in SECO to 0.18 eV higher BE inconsistent with what we would expect to see if it was exclusively based on Au atomic percentage at the surface alone. This indicates that dopant concentration is a much more significant factor in the SECO and therefore WF of the sample.

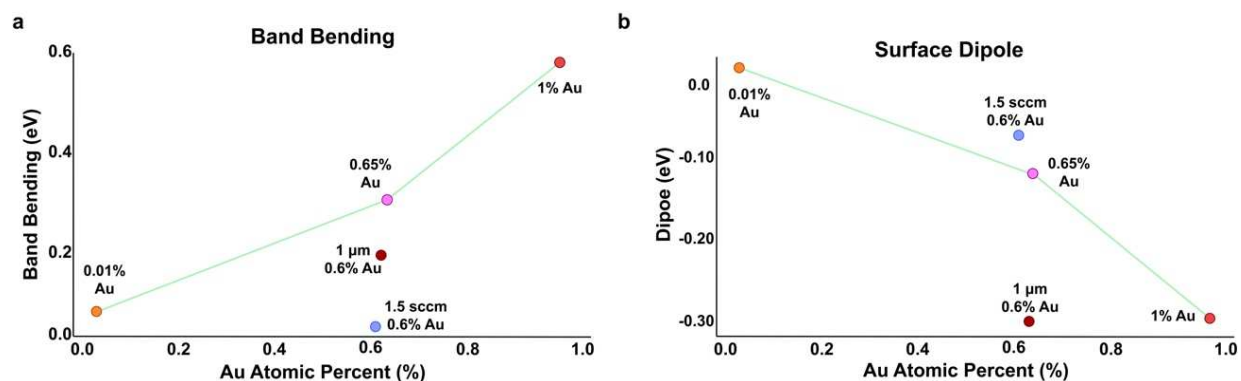


Figure 2-9. Calculated values for band bending and surface dipole for PIN SiNW samples. **a.** The band bending of the SiNW sample is shown to be linked to the atomic percent with higher gold incorporation resulting in more significant band bending. From this analysis we identify gold atomic percentage and phosphine doping ratio (periwinkle) to be the two key factors affecting band bending. **b.** The calculated surface dipole indicates that the more significant percent of gold at the surface the more negative the dipole. Additionally, the large diameter SiNWs (maroon) indicate that size is a key factor beyond gold atomic percent.

2.2.1.4 XPS and UPS band structure

Both the XPS core level electron spectra and UPS valence band spectra provided information regarding Si 2p BE shift and work function respectively. Integrating these two sets of data via the method defined the band bending and surface dipole can be calculated to identify band structure at the surface. Bulk VB and CB values are calculated from dopant concentration determined by gas flow. These properties are key to predicting how these materials will behave at the silicon vacuum interface. The fermi level of the sample is equilibrated to the fermi level of the instrument. Energy band structure calculations are based on methods previously outlined, and explored here for further investigation.^{15,16,18}

$$E_{\text{vbm}}^{\text{s}} = \text{BE}(\text{Si } 2\text{p}_{3/2}) - \text{BE}^{\text{V}}(\text{Si } 2\text{p}_{3/2}) \quad (1-1)$$

The $\text{BE}(\text{Si } 2\text{p}_{3/2})$ is the binding energy of the Si 2p peak measured from the XPS data. Literature values for the Si 2p peak fall within the range of 98.74 – 99.86 eV^{19,20} while $\text{BE}^{\text{V}}(\text{Si } 2\text{p}_{3/2})$ is the reference value of the Si 2p peak verified by literature to be 98.74.²¹⁻²³ The band bending of the silicon is calculated by determining the difference from the Fermi level to the bulk valence band ($E_{\text{vbm}}^{\text{s}}$) is a measure of the valence band minimum at the surface. The bulk valence band minimum in bulk ($E_{\text{vbm}}^{\text{B}}$) is the calculated from the doping ratio of the silicon samples.

$$E_{\text{bb}} = E_{\text{vbm}}^{\text{B}} - E_{\text{vbm}}^{\text{s}} \quad (1-2)$$

$$E_{\text{bb}} = E_{\text{vbm}}^{\text{B}} - \text{BE}^{\text{V}}(\text{Si } 2\text{p}_{3/2}) - \text{BE}(\text{Si } 2\text{p}_{3/2}) \quad (1-3)$$

Band bending of silicon can be determined (Figure 2-9 a) from the XPS core level measurements because the space charge region is relatively large compared to the depth from which these photoelectrons are generated. Therefore band bending has a direct impact on the BE of the Si 2p peak. A positive value for band bending (E_{bb}) indicates that the energy level increases from the fermi level. The degree of band bending for each sample is identified from the Si 2p BE determined from the XPS data.

Previous studies have used many factors such as surface functionalization¹⁵ to tailor band bending at the silicon surface. The variations examined here; Au percentage incorporation, nanostructure diameter, and doping ratio; each provide different methods of tuning silicon nanostructure band bending. Figure 2-9 demonstrates the increased band bending for samples with increasing Au atomic percentage at the surface of the p-i-n SiNWs based on varied synthetic conditions. The band bending is significant for the p-i-n SiNWs synthesized under 750°C + Vac with the highest Au percentage while the p-i-n SiNWs synthesized under 650°C + Vac with the

lowest Au percentage is almost flat band. The upwards band bending with increased Au atomic percentage at the surface provides novel potential for redox reactions.

Sample Type	Dopant	SECO		Work Function	
		Average	Stdev	Average	Stdev
p	10 sccm	17.27	0.00	3.94	0.00
pp	1.5 sccm	17.12	0.00	4.09	0.00
p membrane	1.5 sccm	17.07	0.01	4.14	0.01
n	2 sccm	17.17	0.00	4.04	0.00
nn	0.3 sccm	16.98	0.02	4.23	0.02
n membrane	1.5 sccm	17.16	0.02	4.05	0.02
pin membrane	1.5 sccm	17.15	0.05	4.06	0.05
pin 750 Vac	1.5 sccm	17.13	0.04	4.08	0.04
pin 750 VAC 1 um	0.3 sccm	17.32	0.13	3.89	0.13
pin 750 VAC	0.3 sccm	16.95	0.06	4.22	0.02
pin 650 : VAC	0.3 sccm	17.04	0.22	4.17645	0.22100561
pin 650 : H2	0.3 sccm	16.98	0.10	4.23174	0.10415872
Au Control		16.80		4.41	

Table 2-2. UPS data calculation of work function from SECO. SECO values are calculated from the intersection of the baseline and slope. Work function values are calculated by subtracting from the $h\nu = 21.21$.

For SiNWs with large diameters, (Figure 2-9 a) band bending is not consistent with what value would be expected if it was entirely dependent on the Au atomic ratio. This indicates that the diameter of the wire contributes a second component to the final value of band bending. Alternatively, band bending for samples with increased doping is close to the value expected for samples with minimal Au atomic incorporation at the surface. The band bending being minimal the structure that results is almost flat band.

$$WF_s = h\nu - SECO \quad (1-4)$$

The work function (WF_s) of the sample depends both on band bending and surface dipole. (Table 2-2) The WF_s is calculated by subtracting the SECO from the HeI value of 21.21 eV. The

surface electron affinity (χ^S) is calculated using the bandgap (E_g) of 1.12 eV for silicon. The bulk electron affinity (χ^B) is identified as 4.05 eV.¹⁵

$$\chi^S = WF_s - E_{cbm}^s = WF_s - (E_g - E_{vbm}^s) \quad (1-5)$$

$$\delta = \chi^S - \chi^B = WF_s - E_g + E_{vbm}^s - \chi^B \quad (1-6)$$

The surface dipole (δ) of the sample is calculated (Figure 2-9 b) from the work function measured by UPS and E_{vbm}^s calculated from the Si 2p shift determined via XPS. Surface dipole strength and orientation provide information as to how electrons pass a potential barrier with electrons either accelerated into vacuum or forced to pass a barrier.

Sample Type	Dopant	Electron Affinity (X)	Band Bending	Surface Dipole
p	10 sccm	3.35	-0.44	-0.70
pp	1.5 sccm	3.59	-0.53	-0.46
p membrane	1.5 sccm	3.58	-0.46	-0.47
n	2 sccm	4.06	-0.09	0.01
nn	0.3 sccm	4.07	0.14	0.02
n membrane	1.5 sccm	3.89	0.09	-0.16
pin membrane	1.5 sccm	4.03	-0.02	-0.02
pin 750 Vac	1.5 sccm	3.97	0.01	-0.08
pin 750 VAC 1 um	0.3 sccm	3.73	0.15	-0.32
pin 750 VAC	0.3 sccm	3.70	0.51	-0.35
pin 650 : VAC	0.3 sccm	4.06	0.01	0.01
pin 650 : H2	0.3 sccm	3.88	0.25	-0.17

Table 2-3. UPS data calculation of electron affinity, band bending, and surface dipole. Values are calculated from equations 1-5 and 1-6.

Understanding the magnitude and direction of this property will indicate the potential for charge transfer across the interface. The calculated surface dipoles for most samples have a negative values indicating that the dipole points inward accelerating electrons out from the surface.

For samples with varied Au atomic percentage at the SiNW surface, increasing the Au percentage resulted in a more negative dipole. Comparing this result to larger diameter SiNWs the dipole is more negative for the 1000 nm wires than simply what is predicted based on the ratio of Au on the surface. This indicates that the SiNW diameter is a critical component determining the electronegativity and surface dipole. The final component determining identified here that impacts the surface dipole is dopant density. For p-i-n SiNWs with increased phosphine doping have a more negative dipole than what would be expected solely based on the ratio of Au percentage at the surface. This indicates that the surface dipole is significantly impacted by the increase of doping.

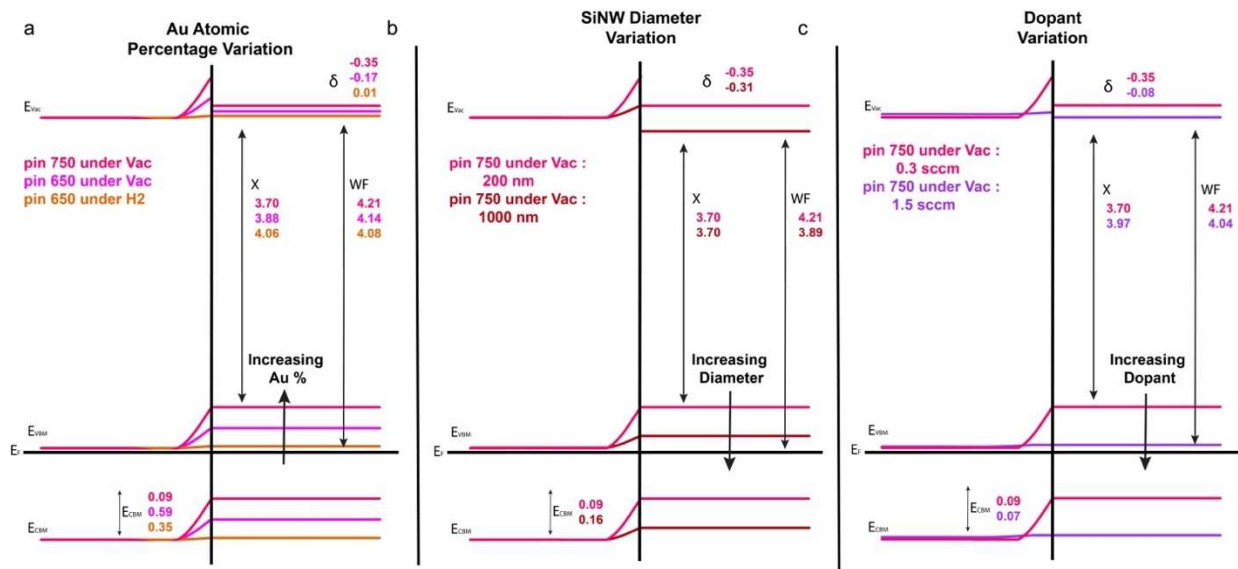


Figure 2-10. Calculated values for band bending, surface dipole, work function, and band bending are integrated into the band structure to visualize the effect of CVD variations on band structure. a. The band bending of the SiNW sample is shown to be linked to the atomic percent with higher gold incorporation resulting in more significant band bending. Included are values for BB, X , and dipole. **b.** Large diameter SiNWs (maroon) are plotted against the red trace of PIN sample from a. with the same synthetic conditions and the only variable being diameter. **c.** High phosphine doping SiNWs (purple) are plotted against the red trace of PIN sample from a. with the same synthetic conditions and the only variable being diameter.

Integrating this data for surface values and bulk values into band diagrams (Figure 2-10) provides insight into the effects of each of these factors on the surface band structure. Our ability

to tailor these interfaces will allow us to produce nanomaterials with higher sensitivity for effective photoelectrochemical, electronic, electrochemical, and optical signals for transduction from freestanding wireless electronics at the interface. We have previously demonstrated that photoelectrochemical properties of p-i-n silicon nanowires are significantly enhanced due to gold diffusion along the surface during the growth process. Through this surface modification, SiNWs were able to elicit action potentials in neurons.¹⁷ With a characterization method to study the effects of chemical and morphological surface changes we will be able to further understand the electronic properties driving how the gold becomes integral to photoelectric processes in biological conditions.

2.2.2 Implementation of XPS analysis methods to characterized nanostructures with CVD synthetic variations for specific applications.

With an understanding of the impacts of CVD synthetic alterations; gold incorporation, dopant ratio, and nanostructure sizes we can identify surface properties such as WF, band bending and surface dipole. With this understanding of how to control these factors we can leverage the CVD synthesis process to target specific physiochemical properties at the silicon surface. From here we can target materials to applications with specific requirements for the silicon device interface. Here we explore two such applications of different nanostructured tailored for optical stimulation specific biointerfaces.

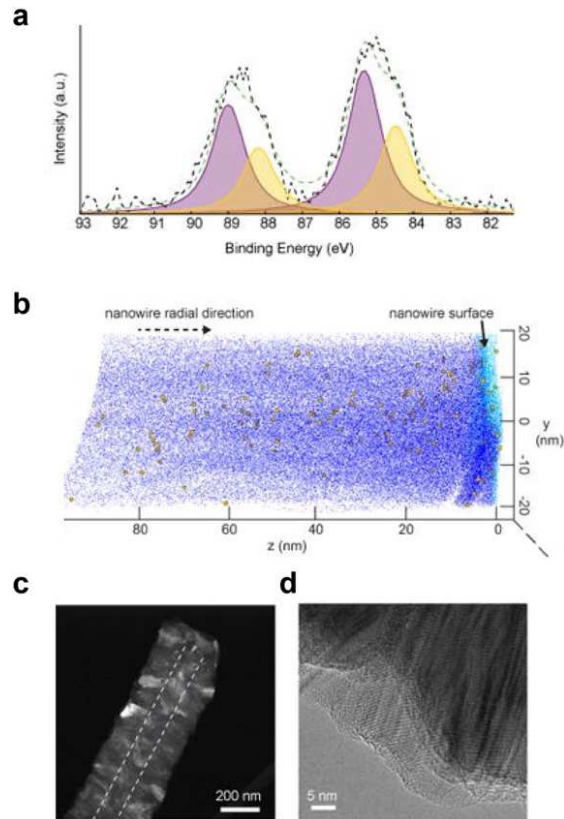


Figure 2-11. Characterization of PIN SiNW surfaces. **a.** XPS analysis indicated the presence of gold accumulation at the surface of the SiNWs by measuring the 10 nm depth at the surface. The fitting contains peaks at 84.5 eV indicating nanoclusters of gold while peaks at 85.4 eV provide evidence of atomic gold species. **b.** The XPS analysis is verified by 3D atom probe tomography (APT) analysis of PIN SiNWs with silicon (dark blue), oxygen (light blue), and gold (yellow). From this visualization of the SiNW surface the presence of atomic gold at the surface of the SiNW and through the center of the wire are visible. **c.** The SiNW structure is interrogated with High annular dark field (HAADF) STEM imaging of the structure. The p-type core is identified by the white line. The shell of the SiNWs is shown to be polycrystalline. **d.** The TEM images of the PIN SiNWs demonstrate the SiNW diameters for 64 wires fell between 200 – 250 nm. Reproduced from Ref. 17

2.2.3 Atomic gold at the surface of PIN SiNWs is key to photoelectrochemical stimulation at biointerfaces as demonstrated by neuronal stimulation

As we have demonstrated several different methods of incorporating varying ratios of gold at the PIN core-shell SiNW surface we can explore the potential applications of these nanostructures and the fundamental factors for these specific applications. Here we apply PIN SiNWs grown at 750 °C under Vac. We utilize these SiNWs to optically and wirelessly modulate primary rat dorsal root ganglion neurons. The coaxial SiNW neuron interface here is key to the

effective stimulation of neurons. Through this analysis we identify the role that the surface atomic gold plays in the light induced processes at the interface. We demonstrate the importance of the Au-Si component for the charge transfer process at the biointerface.

Sample	atomic-like 5/2 peak	atomic-like 7/2 peak	nanoclustered 5/2 peak	nanoclustered 7/2 peak
metallic Au				
p type SiNW	89.1	85.4	88.6	84.9
PIN-SiNW 1	88.8	85.1	88.3	84.6
PIN-SiNW 2	88.9	85.2	88	84.4
PIN-SiNW 3	88.9	85.2	87.9	84.3
PIN-SiNW 4	89	85.4	88.1	84.4
PIN-SiNW 5	89	85.4	88.1	84.5
PIN-SiNW 6	89	85.3	88.2	84.5

Sample	metallic 5/2 peak	metallic 7/2 peak
metallic Au	87.5	83.4
p type SiNW	87.7	84
PIN-SiNW 1		
PIN-SiNW 2		
PIN-SiNW 3		
PIN-SiNW 4		
PIN-SiNW 5		
PIN-SiNW 6		

Table 2-4. Calculated Au 4f binding energies for the studies of the gold ratio at the surface. Au 4f binding energies are compared for PIN SiNWs, p-type SiNWs, and metallic gold control. This provides in-depth understanding of the shift from metallic gold to atomic gold based on XPS binding energy analysis. Reproduced from Ref. 17

2.2.3.1 Identifying gold at the surface of PIN SiNWs by XPS

The conditions during shell growth and the SiNW diameter dictate the concentration of gold atoms that end up at the surface which can range from ~0.0% to ~1%. To identify the presence of atomic gold at the surface of these SiNWs available to participate in the charge transfer processes for photoelectrochemical stimulation we analyzed SiNWs by XPS. From this analysis we identified the shift from core p-type SiNWs with predominantly metallic gold shifts (84 eV) to PIN SiNWs with Au 4f peaks almost exclusively shifted to Au-Si gold shifts (85.4 eV). (Table 2-4) We compared this data to sputter cleaned gold control with an Au peak shift of 84 eV. This provides evidence that the SiNWs do have Au-Si at the surface available for charge transfer at the

interface. This analysis was verified by 3D chemical reconstruction from APT data demonstrating a majority of silicon atoms with silicon dioxide at the surface and a distribution of gold atoms from the surface towards the center up to 100 nm from the surface. The XPS data samples the top 10 nm, a key region for determining the surface band structure and the potential for surface gold atoms to participate in charge transfer at the interface. The region from 10 nm deep to 100 nm deep of APT data (Figure 2-10 b) shows a distribution of gold atoms through the SiNW indicates how the rest of the gold from the Au cap that isn't available at the surface for XPS calculations is arranged throughout the SiNW.

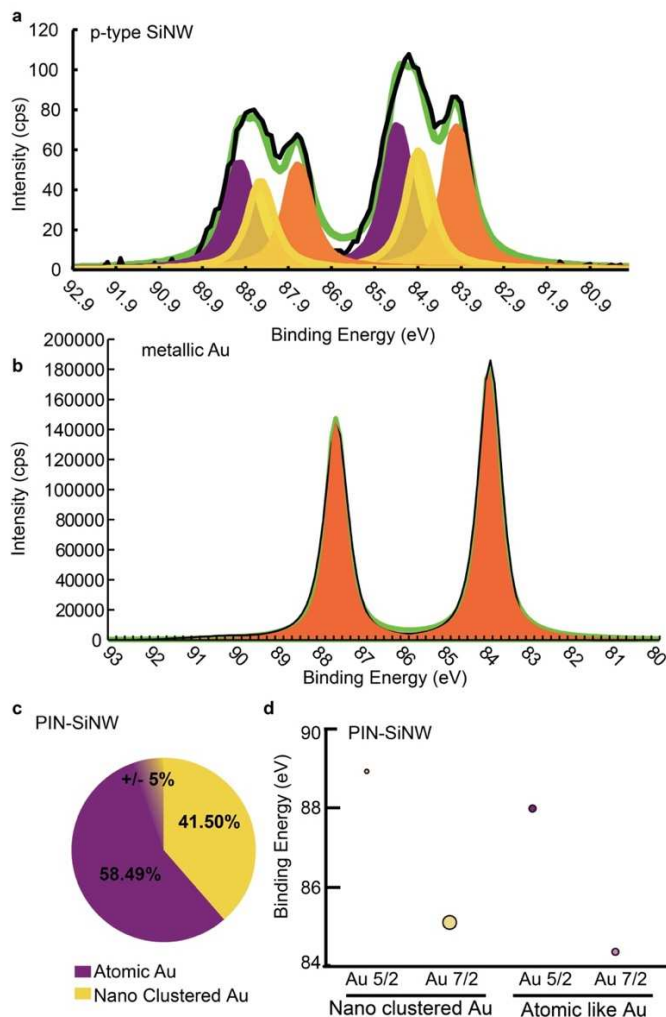


Figure 2-12. In depth analysis of XPS data collected for PIN SiNWs for neuron stimulation. a. The XPS analysis demonstrated Au 4f spectra for p-type SiNWs. This analysis was used for the calculations of values for

Figure 2-12 continued. table 2-4. From this data it is evident that the core p-type SiNWs are significantly heavier in metallic gold signal compared to core-shell SiNWs. **b.** XPS peak fitting and chemical identification was accomplished through comparison with metallic gold signal. The metallic gold shift was found to be 84 eV with an average peak width of 0.6 eV. **c.** Included is a pie chart depicting the percent of atomic like (purple) and gold nanocluster species (yellow) **d.** The average binding energies for peak shifts were calculated to verify assigned peak analysis falls within ideal range. Reproduced from Ref. 17

2.2.3.2 Optical stimulation at the PIN SiNW neuron interface is capable of eliciting an action potential

Based on the identification of atomic gold species at the PIN SiNWs (750 °C under Vac) surface and the demonstrated impact this gold ratio has on the potential for stimulation, we apply this material to primary dorsal root ganglion neurons. SiNWs were sonicated to remove from growth substrate and drop casted over the neuron culture. After settling for 20 minutes cells and SiNWs were found to form a close association with neuron membranes, localizing SiNWs to the cell surface without being internalized. Under 523 nm laser stimulation (Figure 2-11) the action potential of the neuron was monitored via patch clamp. We found that laser stimulation of the PIN SiNW neuron interface was sufficient to cause membrane depolarization triggering an action potential in the targeted cell. The minimum laser energy required to elicit an action potential from a neuron was an average of 6.44 μ J between 0.5 ms to 5 ms. For control experiments pure p-type or undoped SiNWs were only able to elicit sub-threshold depolarization.

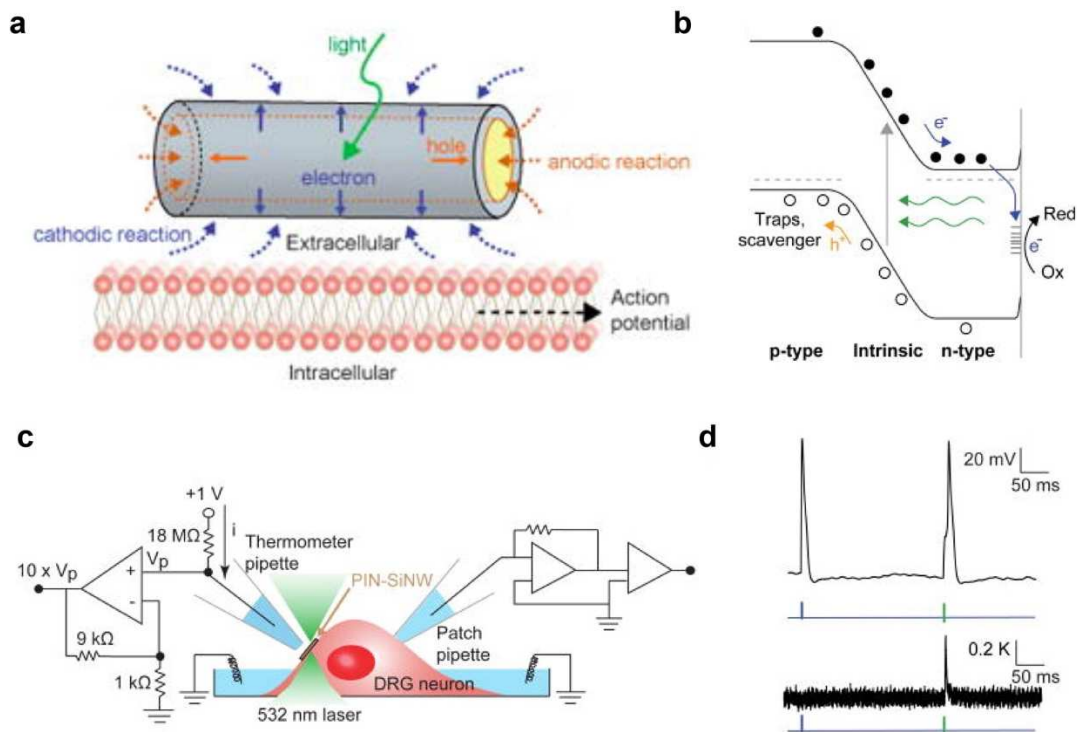


Figure 2-13. Function of SiNWs at cellular interfaces for neuronal stimulation. **a.** The PIN SiNW stimulation at the membrane interface proceeds through either a cathodic reaction or anodic reaction. The light stimulated faradic current at the SiNW – neuron interface results from the movement of electrons (blue) or holes (orange). The light stimulation is sufficient to produce an action potential at this extracellular interface. **b.** The band diagram of the PIN SiNW interface is key to understanding the stimulation method. From the XPS analysis the presence of gold at the surface is identified, and here shown to be a key component for reducing the kinetic barrier for photoelectrochemical reactions. **c.** The schematic outlined here is the setup for the measurement of the change in temperature and neuron action potential produced through injected current stimulation of SiNW light stimulation. **d.** Current trace of the membrane voltage for DRG neuron stimulation indicates that cells have a positive control response to injected current (blue) and PIN SiNW at the neuron interface stimulated by a 532 nm laser pulse. (green) Reproduced from Ref. 17

2.2.3.3 Atomic gold is an important component for photoelectric stimulation at the PIN SiNW

To distinguish how sensitive the optical stimulation process is to the atomic gold density at the surface is SiNWs were grown with lowered gold incorporation. SiNWs were fabricated with core growth times of 30 minutes and 10 minutes. For the shorter core growth times the resulting SiNW length is shorter, but the rest of the growth process is the same. For shorter SiNWs, during the gold diffusion process much of the gold diffuses down the surface of the wire onto the growth wafer causing a significant reduction in the atomic gold present at the surface of the SiNWs. For

the SiNWs with significantly reduced surface atomic gold, the average minimum laser energy that was required to stimulate action potentials was on average 19.26 μJ . This is about three times more than the minimum laser energy required for the typical PIN SiNWs with higher gold incorporation. From this analysis it is clear that PIN SiNWs efficiently stimulate the neuron SiNW interface and that the surface Au-Si ratio is key to the photoelectric effect

2.2.4 Silicon metal alloy interface dictates surface chemical patterning

The CVD gold assisted VLS process relies on the use of a liquid alloy for SiNW growth. The dynamics of this process are largely unexplored within the realm of the significant variations available for diameter, temperature, doping ect. The main benefit of the SiNW structures is the wide range of structural and chemical diversity available, but the impact of this is that there are still so many unknown effects of these synthesis variations especially during the VLS growth. Here we describe previously unexplored range of silicon structures with doping and size properties that result in periodic atomic patterning of gold on the SiNW sidewalls. The liquid alloy droplet serves as a reservoir of gold atoms at the SiNW cap used to deposit metal species on the SiNW sidewall. The deposition of the metal atoms is determined to be a result of oscillations during the VLS growth process similar to the classic coffee ring effects. This variability was found to be mainly dependent on high phosphine (n-type) doping ratios with a small dependence on SiNW diameter 100 – 500 nm. We identify a stick slip motion of the gold nanoparticle on the SiNW sidewall as a result of instability at the SiNW and liquid metal alloy. Based on the chemical interface between the silicon, dopant, and gold alloy, the droplet pins on the side wall and the SiNW elongation causes the instability leading to slipping at the droplets edge leaving periodic rows of atomic gold at the silicon surface at 5 nm gaps. This method provides an alternative approach to the core shell SiNW growth for localizing gold at the surface the nanowire.

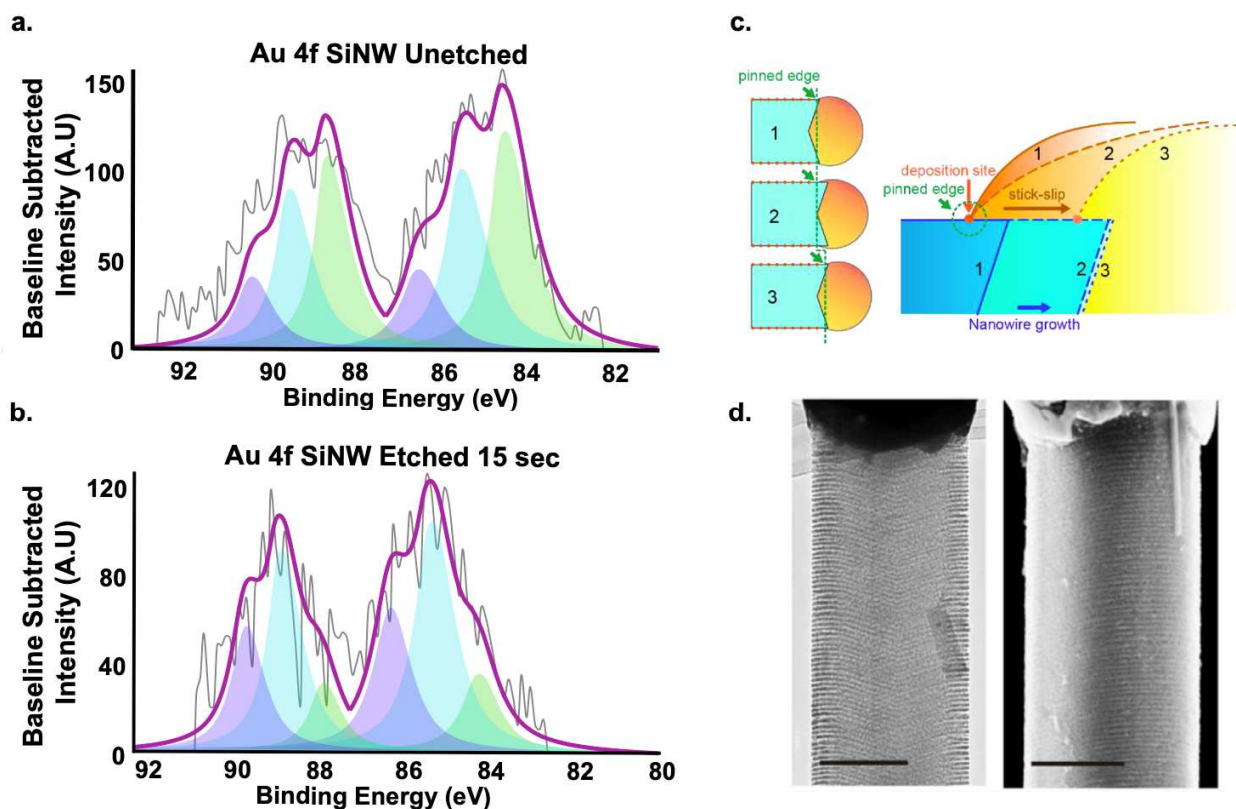


Figure 2-14. The presence of atomic gold is identified through peak analysis of the Au 4f signal. a. The p-type 200 nm high phosphine doped core SiNW samples demonstrate significant metallic gold peak (green) resulting from the gold cap. The intermetallic (blue) and gold silicide (purple) peaks indicate a high ratio of atomic gold corresponding to the increased gold deposition along the surface of the SiNW. **b.** After etching with gold etchant, the SiNWs metallic signal is significantly reduced. This demonstrates the predominant gold silicide presence remaining after gold etching. **c.** Diagram of the gold droplet pinning at the surface of the SiNW. This pinning and shifting instability results in periodic deposition of atomic gold along the surface as identified by XPS. **d.** TEM and SEM of SiNWs post metal assisted chemical etching (MACE) reveals the periodic porous structure. (Scale bar 200 nm) Reproduced from Ref. 10

2.2.4.1.1 Characterizing the rows of atomic gold at the SiNW surface by XPS

Metal assisted chemical etching (MACE) of highly doped n-type silicon reveals periodic trends indicating the instability periodically depositing gold on the SiNW surface is paired with a force that immobilizes the gold in the originally deposited location.¹⁰ (Figure 2-13) This atomic based MACE process is based on the classic MACE approach. This provided the primary evidence of the periodic atomic incorporation. XPS analysis provides evidence of the gold immobilized on the SiNW surface and provides insight into the gold environment. From the Au 4f peak analysis

we see a shift from predominantly metallic gold (84 eV) for unetched SiNWs to almost exclusively intermetallic Au-Si peaks for SiNWs treated with gold etchant. This process removes the metallic gold from the gold cap resulting in the loss of the metallic gold peak. The intermetallic gold remaining in wires treated with gold etchant indicates that excluding the gold present in the metallic cap (Au reservoir) the gold deposited periodically due to growth instability is trapped at the surface (top ten nm) and that it present in the Au-Si form. From this data we observe that this gold variation is determined to be isolated atoms in a clear chain perpendicular to the SiNW surface predominantly within the top 10 nm. From the UPS analysis of the SiNWs with the conditions unetched, Au etchant 15 seconds, and Au etchant 1 minute, we characterize the effect of high ratio of Au-Si local incorporation at the interface on the WF of the SiNW sample. From previous analysis of SiNWs with varieties of gold incorporation at the surface we see a high work functions corresponding to high gold ratios. For the samples with increased etching the gold ratio decreases and the WF has a corresponding decrease. This indicates that the significant atomic gold incorporation at the surface shifts the WF towards the WF of the gold control.

2.2.4.1.2 Phosphine effects on gold

The identification of this periodic atomic gold deposition for high dopant density n-type wires provided insight into the stick slip motion at the droplet edge during growth. When compared to p-type or intrinsic wires where no periodic atomic deposition occurs it becomes clear that the chemical composition is what is dictating the silicon – liquid alloy interface. When SiNWs were grown with vertical (vs coaxial PIN samples with horizontal) dopant modulated n-type / i-type / n-type (ect) segments the periodic atomic deposition halts during intrinsic segments and occurs during n-type segments. Previous investigations of surface chemistry provide insight into this variability. Boron has been shown to promote gold diffusion.¹⁰ This coffee ring like effect

necessitates the immobilization of gold or else the patterning would continue to diffuse until it is unrecognizable. Previous studies of intrinsic silicon has shown that the silicon interface is passivated with hydrogen, and when gold does deposit onto the sidewalls it de-wets from this interface resulting in aggregates in the form of gold nanoparticles.²⁴ In a similar manner this chemical reactivity would not promote the formation of this periodic atomic gold deposition. Alternatively, phosphorous (n-type) has been shown to interact strongly with both Si and Au.⁷ This strong interaction would promote the gold accumulation on the n-type sidewalls and would provide the immobilizing force required to trap the gold atoms at the surface. This understanding of chemical potential provides insight into how this silicon liquid metal-alloy interface dictates the structure of the wires from CVD growth.

2.2.4.1.3 Stick slip motion depends on the chemical environment at the silicon interface

From this analysis we can identify the growth mechanism for the periodic atomic gold arrangement on the heavily doped n-type SiNW surface. From the characterization of the gold deposition and the understanding of the chemical environment driving this activity during VLS growth we can provide a deeper insight into the conditions directing this sequential patterning process. The switching mechanism dictating the spacing is dependent on instability from the VLS growth process. The effect of sidewall wetting of the SiNW structure is an effect that has been predicted but not significantly explored. Here we see that the highly doped n-type SiNWs are likely promoting this type of robust sidewall wetting. The liquid alloy droplet edge pins on the sidewall of the SiNW. Initially the contact angle is large as the SiNW elongation occurs the contact angle decreases at the pinned location until it reaches a minimum point where the potential barrier forces the droplet edge to slip until it reaches another quasi-stable position where pinning occurs. At the stage where slippage occurs a row of gold atoms is left. This growth mechanism is then contact

angle dependent miming the “coffee ring effect”. Based on this growth mechanism we are able to identify the use of the stick slip motion and silicon liquid metal alloy interface as being novel mechanisms for three dimensional atomic printing on the SiNW sidewall.

2.2.5 Conclusions and Outlook

The established PES method to directly characterize the variation in surface properties that results from synthetic alterations. These studies have demonstrated the significant potential to use easily tailored CVD alterations to structure impacts the Si/vac interface. Samples either exhibited variations based on either Au atomic percentage incorporation, SiNW diameter, or doping ratio with each variable altering specific variables key to surface electronic band structure to different intensity. Further, we show that these moderate synthetic modifications cause large variation of the material chemical composition and electronic properties; Work function, surface dipole, band bending and these variations can be used as controls to modify one lever or another to tailor nanostructure devices for applications. Silicon nanomaterials have already been applied to a wide range of fields: electronics, bioelectronics, catalysis, optoelectronics, and more.²⁵ Understanding how the electrical and optical properties are impacted by surface changes and how these surfaces interact with their environment and will be integral to advancing nanomaterial applications and directing the targeted development of novel materials. Through this work we can: (a) establish a protocol based on PES to characterize our nanomaterials, (b) apply this characterization to fundamentally understand electronic properties of silicon nanostructures and how they interface with their environment, and (c) rationally design a wider range of nanomaterials with targeted applications. From this analysis we explore a series of structures with significant variation due to the contamination of gold at the SiNW surface during the CVD process. This occurred through two different mechanism to (1) stimulation neurons and (2) induce etching of periodic groves along

the surface the SiNWs based on the interaction between the phosphine and gold. From this series of analysis we are able to establish a platform of silicon nanomaterials with a wide functionality. Exploring a larger range of materials with the combinatorial XPS and UPS analysis to delve deeper into what factors tailor the chemical composition and electronic band structure resulting from the surface which is dominated by silicon interfaces.

2.3 Experimental

Material Synthesis : All silicon materials, membranes and SiNWs, were synthesized via CVD. Silicon growth was performed through either the VLS or VS method. VLS synthesis occurs at lower temperatures with a gold nanoparticle (AuNP) catalyst. This is always the first step of SiNW growth as it grows the NW core. Core SiNWs were synthesized at 470°C for p-type or 480°C for n-type. The AuNP dictates the core SiNW diameter and after VLS growth the majority of the gold remains trapped in the AuNP cap. Although, during the process of SiNW core growth a small portion of Au atoms can be deposited at the surface depending on doping ratio or pressure.¹⁰ Membrane or shell depositions were performed via the VS method at elevated temperatures of 650°C or 750°C. The shell growth conditions chosen result in deposition of the AuNP down the surface of the wire. Under these conditions silane shell growth occurs radially on the SiNWs, and the high diffusivity of gold in silicon allows it to float to the surface of the SiNWs. The specific conditions chosen for this growth dictate the ratio of atoms that reach the surface of the silicon. Based on this simple synthetic procedure, a range of variables can be easily applied to the nanostructure growth that we show to be key to tailoring surface chemical composition and electronic band structure. (1) Between VLS and VS growth, the ratio of gold incorporation at the surface is a condition that can be easily tailored based on synthetic conditions. (2) A second impact of the VS shell growth is significant variation of the wire diameter based on location of the growth

wafer in the CVD chamber. Across the profile of the CVD chamber the temperature of the gasses varies moderately and this variation changes the growth rate of silicon deposited via the VS method. Due to this growth rate variability wires of different sizes; 200 nm – 1000 nm can be synthesized by merely altering chip location in the chamber. (3) The doping ratio of materials are determined by the ratio of the silane to dopant flow rate of each individual gas. For the comparison of the effects of altering doping ratios the n-type samples are varied between a low flow rate of 0.3 sccm to a high flow rate of 1.5 sccm. Samples were cut and prepared for loading into the vacuum chamber in the clean rom. With this set of procedures carbon contamination of the sample surface was minimized. Using the XPS survey spectra the ratio of carbon atoms on the surface was calculated and determined to be below the acceptable threshold.

XPS Data Analysis : XPS data for SiNW samples were collected with the AXIS Nova (Kratos Analytical) with monochromatic Al K α X-ray source. The Al anode was powered at 10 mA and 15 kV. The instrument work function was calibrated to give an Au 4f_{7/2} metallic gold binding energy (BE) of 83.95 eV. Instrument base pressure was *ca.* 1×10^{-9} Torr. The analysis area size was 0.30.7 mm². For calibration purposes, the binding energies were referenced to Si 2p peak at 99.8 eV and/or C 1s peak at 284.5 eV. To improve reliability of the calibration. Survey spectra were collected with a step size of 1 eV and 160 eV pass energy. The high-resolution spectra of Si 2p and Au 4f were collected with a pass energy of 20 eV and 0.1 eV step size using 3 and 20 sweeps of 120 s for each sweep, respectively. XPS peaks were fitted with an asymmetric Gaussian/Lorentzian peak shape with linear background correction. Initial peak approximation model was based on the Au 4f peak modeling of the pure gold sample in order to better evaluate the asymmetric nature of the peak profile and the fit envelope.

2.4 Bibliography

- 1 Kempa, T. J. *et al.* Single and Tandem Axial p-i-n Nanowire Photovoltaic Devices. *Nano Letters* **8**, 3456-3460, doi:10.1021/nl8023438 (2008).
- 2 Tian, B. *et al.* Coaxial silicon nanowires as solar cells and nanoelectronic power sources. *Nature* **449**, 885, doi:10.1038/nature06181 (2007).
- 3 Cao, L. *et al.* Instability and Transport of Metal Catalyst in the Growth of Tapered Silicon Nanowires. *Nano Letters* **6**, 1852-1857, doi:10.1021/nl060533r (2006).
- 4 Tian, B., Xie, P., Kempa, T. J., Bell, D. C. & Lieber, C. M. Single-crystalline kinked semiconductor nanowire superstructures. *Nature Nanotechnology* **4**, 824, doi:10.1038/nnano.2009.304 (2009).
- 5 Zhang, B., Jie, J., Zhang, X., Ou, X. & Zhang, X. Large-Scale Fabrication of Silicon Nanowires for Solar Energy Applications. *ACS Applied Materials & Interfaces* **9**, 34527-34543, doi:10.1021/acsami.7b06620 (2017).
- 6 Zimmerman, J. F. *et al.* Free-Standing Kinked Silicon Nanowires for Probing Inter- and Intracellular Force Dynamics. *Nano Letters* **15**, 5492-5498, doi:10.1021/acs.nanolett.5b01963 (2015).
- 7 Luo, Z. *et al.* Atomic gold-enabled three-dimensional lithography for silicon mesostructures. *Science* **348**, 1451, doi:10.1126/science.1257278 (2015).
- 8 Dick, K. A., Thelander, C., Samuelson, L. & Caroff, P. Crystal Phase Engineering in Single InAs Nanowires. *Nano Letters* **10**, 3494-3499, doi:10.1021/nl101632a (2010).
- 9 Shin, N., Chi, M., Howe, J. Y. & Filler, M. A. Rational Defect Introduction in Silicon Nanowires. *Nano Letters* **13**, 1928-1933, doi:10.1021/nl3042728 (2013).
- 10 Fang, Y. *et al.* Alloy-assisted deposition of three-dimensional arrays of atomic gold catalyst for crystal growth studies. *Nature Communications* **8**, 2014, doi:10.1038/s41467-017-02025-x (2017).
- 11 Lay, G. L. Physics and electronics of the noble-metal/elemental-semiconductor interface formation: A status report. *Surface Science* **132**, 169-204 (1983).
- 12 Li, Y., Shi, W., Gupta, A. & Chopra, N. Morphological evolution of gold nanoparticles on silicon nanowires and their plasmonics. *RSC Advances* **5**, 49708-49718, doi:10.1039/C5RA06921A (2015).
- 13 Sohn, Y., Pradhan, D., Radi, A. & Leung, K. T. Interfacial Electronic Structure of Gold Nanoparticles on Si(100): Alloying versus Quantum Size Effects. *Langmuir* **25**, 9557-9563, doi:10.1021/la900828v (2009).
- 14 Zhao, L., Siu, A. C.-L., Petrus, J. A., He, Z. & Leung, K. T. Interfacial Bonding of Gold Nanoparticles on a H-terminated Si(100) Substrate Obtained by Electro- and Electroless Deposition. *Journal of the American Chemical Society* **129**, 5730-5734, doi:10.1021/ja070441j (2007).
- 15 Hacker, C. A. in *2009 International Semiconductor Device Research Symposium*. 1-2.
- 16 Gleason-Rohrer, D. C., Brunschwig, B. S. & Lewis, N. S. Measurement of the Band Bending and Surface Dipole at Chemically Functionalized Si(111)/Vacuum Interfaces. *The Journal of Physical Chemistry C* **117**, 18031-18042, doi:10.1021/jp401585s (2013).
- 17 Parameswaran, R. *et al.* Photoelectrochemical modulation of neuronal activity with free-standing coaxial silicon nanowires. *Nature Nanotechnology* **13**, 260-266, doi:10.1038/s41565-017-0041-7 (2018).
- 18 Schlaf, D. R. Tutorial on Work Function.

- 19 Constantin Logofatu, C. C. N., Rodica V. Ghita, Florica Ungureanu, Constantin Cotirlan, Cornelui Ghica Adrian Stefan Manea and Mihai Florin Lazarescu *Study of SiO₂/Si Interface by Surface Techniques, Crystalline Silicon - Properties and Uses, Prof. Sukumar Basu.* (InTech, 2011).
- 20 J-W. He, X. X., J. S. Corneille, D. W. Goodman. X-ray photoelectron spectroscopic characterization of ultra-thin silicon oxide films on a Mo(100) surface. *Surface Science* **279**, 119-126 (1992).
- 21 Himpsel, F. J., Hollinger, G. & Pollak, R. A. Determination of the Fermi-level pinning position at Si(111) surfaces. *Physical Review B* **28**, 7014-7018, doi:10.1103/PhysRevB.28.7014 (1983).
- 22 He, T. *et al.* Silicon/Molecule Interfacial Electronic Modifications. *Journal of the American Chemical Society* **130**, 1699-1710, doi:10.1021/ja0768789 (2008).
- 23 Hunger, R. *et al.* Electronic Structure of Methoxy-, Bromo-, and Nitrobenzene Grafted onto Si(111). *The Journal of Physical Chemistry B* **110**, 15432-15441, doi:10.1021/jp055702v (2006).
- 24 Connell, J. G. *et al.* Identification of an Intrinsic Source of Doping Inhomogeneity in Vapor–Liquid–Solid-Grown Nanowires. *Nano Letters* **13**, 199-206, doi:10.1021/nl3038695 (2013).
- 25 Peng, F. *et al.* Silicon Nanomaterials Platform for Bioimaging, Biosensing, and Cancer Therapy. *Accounts of Chemical Research* **47**, 612-623, doi:10.1021/ar400221g (2014).

Chapter 3 : Exploring the post-synthetic tuning of silicon nanostructures for specific bio interfaces

3.1 Introduction

It is clear that we are able to tailor silicon nanostructure morphologies during synthesis including dopant modulation¹, core-shell structures, SiNW diameter and tapering², kinked SiNWs³, gold incorporation⁴. Here we use XPS to interrogate the post synthetic alterations that can be employed to alter silicon surfaces after the CVD synthesis process. These post-synthetic alterations provide us with the ability to target more specifically desired biointerfaces for applications to a variety of cellular systems. This will include surface functionalization of photoactive compounds for stimulating cardiac cells, functionalization with T-cell targeting antibodies, etching to produce photothermal properties for optical neuron stimulation, and varied metal coating to track redox reactions occurring during intracellular applications. From this work we will be able to understand the impacts of different surface modification approaches to varied silicon – biological interfaces to more specifically target materials for required tasks.

3.2 Results and discussion

3.2.1 Silicon chemistry employed for surface functionalization

Silicon surface chemistry has been a well explored method for functionalizing silicon surfaces for a variety of applications ranging from cellular targeting to surface protection from oxidation. The high surface area of silicon nanostructures allows for a high density functionalization. Refinement of these procedures and the ability to directly track the surface variations resulting from the different schemes will provide for more significant surface tailoring for various applications.

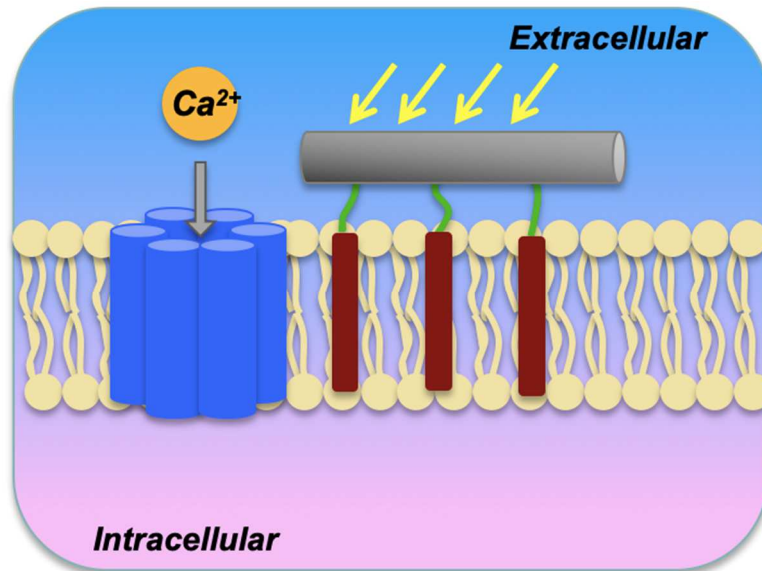


Figure 3-1. Functionalization scheme for APTES based linkage of molecular photodiode to SiNW For this approach, SiNWs are buoyed at the cellular membrane. SiNWs (grey) are linked to molecular photodiode (red) through APTES linkage (green). This process tethers the material to the membrane and localizes the material to target voltage gated calcium channels. Under light illumination charge separation triggers the voltage gated calcium channels for cellular stimulation.

3.2.1.1 APTES based functionalization of SiNW surface with molecular photodiode for targeting cell membranes

This functionalization approach implements a silanization reaction to functionalize the surface for further reaction with a molecular photodiode for interaction with cell membranes.⁵ Linking the molecular photodiode to the surface of a SiNW provides a “raft” that would localize at the cell membrane with a high density of molecules concentrated in the cell membrane. (Figure 3-1) By targeting a patch of the cell membrane with a molecular photodiode under light exposure charge separation within the molecule will stimulate the voltage gated ion channel triggering a cellular response. The functionalization process is key to concentrating a high density of molecules in one patch at the cell surface.

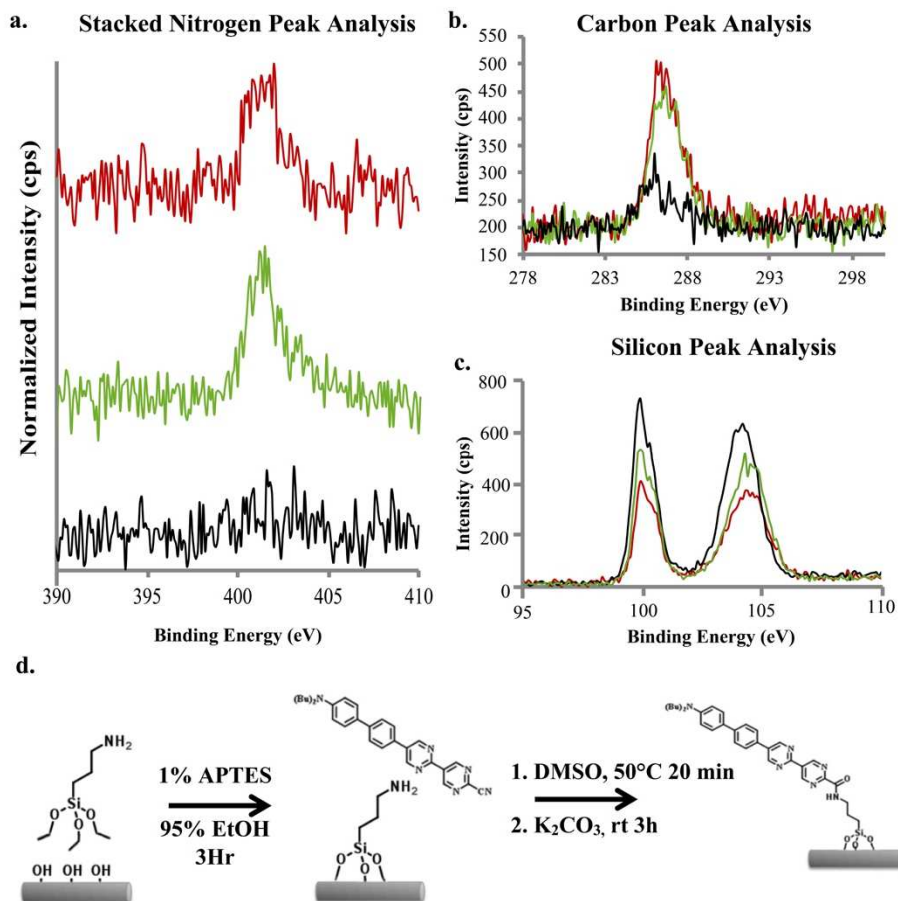


Figure 3-2. Functionalization scheme analyzed by XPS analysis. a-c. XPS analysis of nitrogen, carbon, and silicon peaks indicates the success or failure of different functionalization approaches, the unfunctionalized plasma cleaned SiNW (black), SiNWs with APTES (green), and SiNWs-O-APTES-Dye (red). **a.** The Increase in nitrogen signal from the unfunctionalized plasma cleaned SiNW to the APTES functionalized SiNWs indicated the successful functionalization process based on the nitrogen group. **b.** Increases in the carbon signal from the black adventitious carbon signal indicates successful functionalization. **c.** With each successive step in the procedure the silicon peak analysis shows no variation indicating no change to the silicon at the surface. Significant oxide peak at 105 eV is a result of the plasma cleaning OH functionalization success.

This process involved first reacting a plasma cleaned SiO₂ SiNW surface with APTES and then reacting the amine functionality on APTES with the nitrile group on the molecular photodiode. The key experiment verifying if this functionalization process was successful was we XPS analysis to measure changes in carbon and nitrogen ratio on the surface of the SiNW. Data compares plasma cleaned SiNW with -OH functionality, SiNW-APTES, SiNW-APTES-Molecular Photodiode. From this data we see an increase in nitrogen signal from no measured nitrogen signal for the SiNW-OH to significant nitrogen signal for SiNW-APTES. The SiNW-

APTES-Photodiode exhibits a broader nitrogen peak indicating multiple species of nitrogen as opposed to the narrower peak for the APTES functionalized samples with just an amine group. The carbon signal also dramatically increases for functionalized surfaces. SiNW-OH samples have only adventitious carbon on the surface. Similarly each subsequent functionalization step shows attenuation of the silicon signal. Through this analysis we were able to characterize the success of the APTES functionalization method.

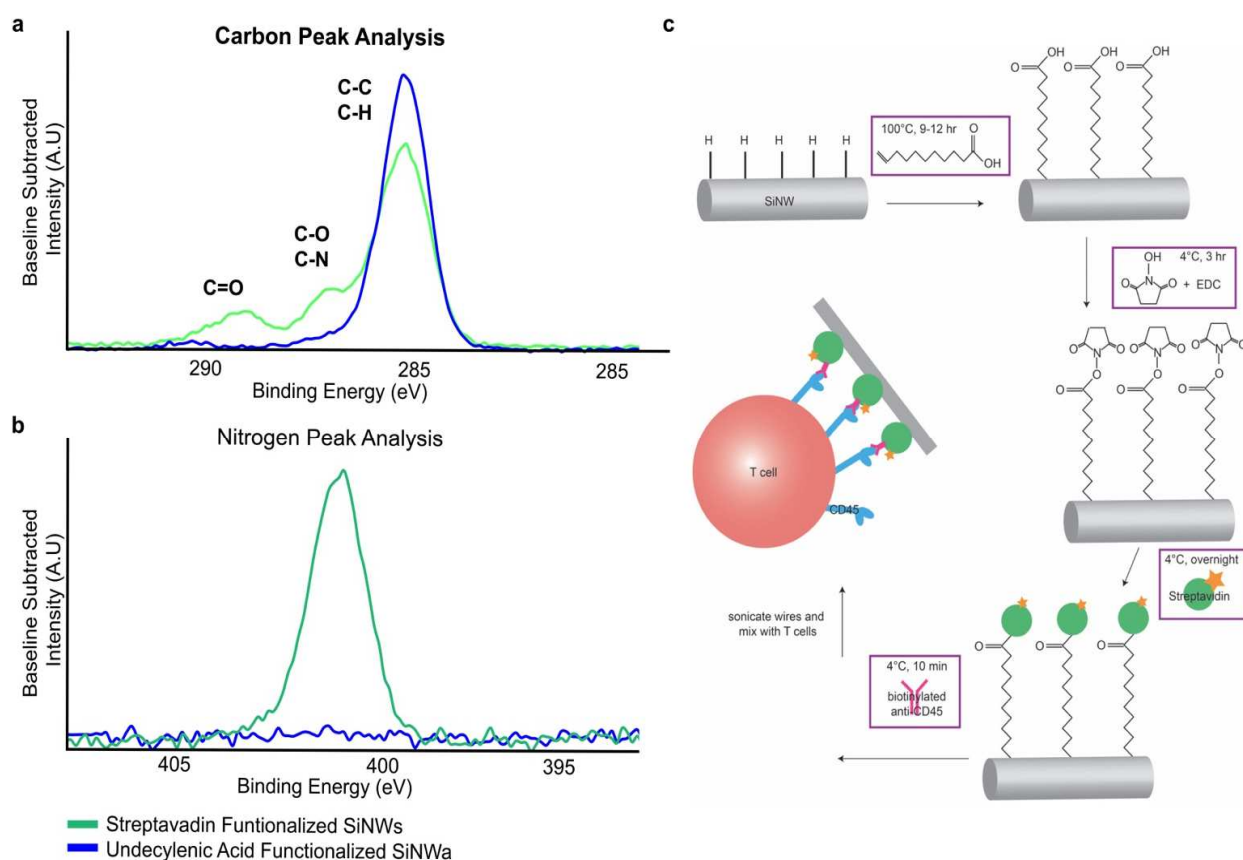


Figure 3-3. Functionalization scheme linking antibodies to the surface of the SiNW based on undecylenic acid linkage. a-b. XPS analysis of nitrogen, carbon peaks indicates the success of functionalization. For this approach the linkage is based on silicon hydride surfaces. **a.** The carbon peak shows increased complexity resulting from the functionalization of the streptavidin protein. This results from the evolution of C=O and C-N peaks typical of protein groups. The undecylenic acid SiNWs (blue) has a significant carbon peak. **b.** The nitrogen peak analysis clearly shows the development of nitrogen signal from no signal to significant signal for streptavidin protein. **c.** Functionalization scheme for linking Anti-CD45 antibody to the surface of the SiNW. This scheme is based on hydrosilylation of HF cleaned SiNW surfaces at 100°C. After functionalization with the antibody, SiNWs can be easily localized at the T cell surface for optical stimulation.

3.2.1.2 Undecylenic Acid functionalization of SiNWs for antibody based targeting to T Cells

Understanding fundamental properties controlling T Cell activation provides insight into treatment of autoimmune diseases. Current therapeutic approaches rely on cytotoxic monoclonal antibodies or various other non-specific approaches. To study this problem we developed a method of targeting SiNWs with photovoltaic properties to the surface of T cells. This surface specificity was accomplished by functionalizing SiNWs with antibodies that bind to T cells.

Hydrogen terminated PIN SiNWs were produced by removing the oxide layer with 10% HF followed by a DI H₂O rinse. The hydrogen terminated silicon surface was reacted with the double bond functionality of undecylenic acid under elevated temperatures.⁶ Following this step 1-ethyl-3-(3-dimethylaminopropyl)carbodiimide (EDC) and N-hydroxysuccinimide (NHS) is reacted with the carboxylic acid groups on the surface. In the final step SiNWs are reacted with APC labeled Streptavidin. The primary amino groups form amide bonds with the carboxylic acid group on undecylenic acid. Through this nucleophilic attack the streptavidin complex replaces the NHS intermediate. The SiNWs are then treated with a biotinylated antibody, anti-CD45. Finally the antibody functionalized SiNWs are introduced to the T cells and provide a driving force binding the SiNWs to the cell surface. Through this functionalization method the SiNW surface is protected from oxide layer growth due to surface functionalization. This prevents the negative side effects of the oxide layer including impedance of the production of photocurrents.

We used XPS to characterize the functionalization at different steps in this procedure. This allowed us to alter the procedure and measure changes in the functionalization in an iterative process to fine tune the synthetic scheme. From elemental composition information at various stages in the process we found that the nitrogen peak present at 401 eV was not present with the hydrosilylation reaction as expected, but that there was significant increase in the nitrogen signal

for streptavidin functionalized SiNWs due to the nitrogen contribution of the protein. Additionally, with each functionalization step the carbon signal becomes more complicated with evolution of a C-O and C-N peak appearing with the streptavidin complex due to the complex protein structure.

Using this functionalization method, PIN SiNWs were confirmed to be strongly localized at the T cell interface. Using Flow cytometry the photovoltaic nature of the PIN SiNWs were employed to optically depolarize T cell populations. Membrane depolarization by the SiNW activated the T cell through the TCR. From highly localized stimulations such as this, fundamental studies on alterations in the TCR-CD3 complex conformation can be accomplished.

3.2.2 Etching SiNWs to advance photothermal properties for stimulating retinal cells

In addition to the photoelectric properties of silicon, we are able to take advantage of the photothermal processes that can occur under illumination for stimulation at cellular interfaces. Although there are many materials including gold, carbon nanotubes, mesoporous silicon useful for photothermal therapy. Silicon is especially useful in photothermal therapies because it is biodegradable in physiological conditions, has low toxicity, low cost, easy fabrication of 1D nanostructures on the scales of cellular interfaces, and methods of dispersal for therapeutic applications.

The photothermal process in silicon occurs by the recombination of light generated carriers converting the photon energy to vibrational energy of the silicon lattice. This process dissipates heat through the silicon and at a silicon water interface it can locally increase the temperature of the surrounding water. This effect has been shown to be dependent on the presence of point defects in the crystal lattice serving as recombination sites. Previously, porous silicon with nanosized pores has been demonstrated ignite under illumination with silicon temperatures exceeding 600 K.⁷ From this study the key components affecting photothermal activity were identified to be the extent of

porosity, optical absorption and thermal conductivity.⁸ To enhance these photothermal properties in SiNWs for cellular stimulation, we intentionally introduced surface point defects into the structure via post synthetic modifications of SiNWs : MACE to produce porous structures. The photothermal properties of these porous SiNWs has been demonstrated by measuring local temperature changes in solution. These were introduced to retinal cell culture, and the neuron-SiNW interface under illumination was shown to photothermally interact at the cellular interface.

3.2.2.1 XPS analysis of SiNW identifying gold during the MACE etching process

We characterized the gold in the MACE process using XPS analysis to identify the presence of gold and the potential for extensive etching.⁹ We examined samples as synthesized with gold on the SiNW sidewall, SiNW treated with gold etchant, SiNWs post MACE etching, and SiNWs treated with gold etchant and then MACE. In the first sample we found a clear metallic peak with a high percentage of gold indicating large portions of the surface will be readily etched by MACE. Samples treated with gold etchant indicated the majority of the metallic gold is removed and the majority of the gold is present on the SiNW surface. The remaining gold was then protected atomic gold in the form of gold silicide. This indicates that the gold present on the surface of the SiNW will be key to successful MACE processes. For SiNW samples treated with the MACE process indicates the evolution of multiple gold peaks shifting from majority metallic gold to intermetallic and atomic gold peaks. Though the gold percentage drops, it is still significantly higher than samples treated with gold etchant. From this analysis we see the MACE process has significant redistribution of the gold resulting from the etching process as the gold etches into the silicon surface to produce a modified distribution of peaks. As a control, SiNWs were first treated with gold etchant and then MACE to identify the changes in the chemical composition on the surface if there is no metals to catalyze the MACE process. For these samples we see minimal gold

percentage. In addition to most of the gold being removed, the gold signal shifts to exclusively one peak, the opposite of the process for the SiNWs treated with just MACE. This indicates the process could be rearranging gold to larger nanoclusters.

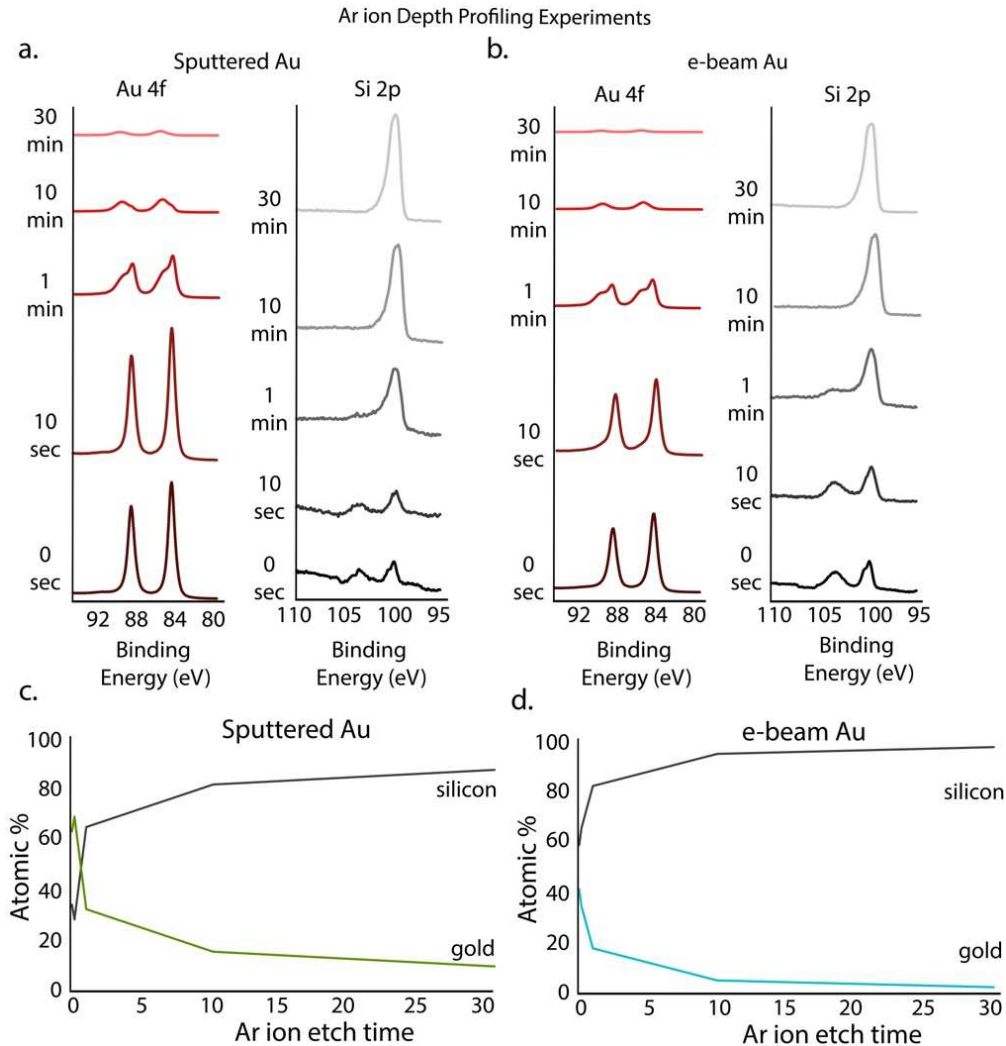


Figure 3-4. Depth profiling reveals the interface variations for sputter coated and e-beam evaporated gold layers on the PIN SiNW surface. a-b. Repeated Ar ion depth cycles followed by XPS analysis. **a.** Etching time vs binding energy for gold and silicon with gold sputter coated samples. Gold shifts from metallic 84 eV to 86 eV gold silicide samples. From this depth profiling it is clear that there is significant intermixing at the interface. This is visualized through the dual peak at 1 min of etching. Au 4f peaks in red and Si 2p peaks are grey. After 10 sec of etching the oxygen of SiO₂ samples are completely etched away. **b.** Depth profiling is compared to e-beam evaporated samples. The variation for this sample indicates intermixing as early as 10 seconds of etching as the Au 4f peak shifts towards 85 eV. **c.** Gold ratio analysis of sputtered samples indicates a predominantly gold surface before etching. After 1 min of etching the majority of the ratio has switched to predominantly silicon. **d.** Atomic ratio of depth profiling for e-beam evaporated gold samples begin as predominantly silicon. The ratios indicate that this surface is significantly different than other gold surfaces.

3.2.3 Silicon nanostructures modified with varied metal coatings; gold, titanium, aluminum, for modifying silicon water interface to tailor redox reactions

The photoelectrochemical processes at the silicon electrolyte interface has been demonstrated to be dependent on the gold contamination of nanostructures during the CVD growth process. This demonstrated surface gold enhanced hydrogen peroxide (H_2O_2) at the silicon electrolyte interface. We employed XPS to characterize the chemical identity of the gold structures on the surface of the silicon. This gold can present as atomic gold, gold nanoclusters, or metallic gold and this is easily identified via XPS chemical analysis. Understanding the ratios of metallic composition at the surface provides deeper insight into potential charge transfer mechanisms occurring at the interface for production of H_2O_2 . We compare this information to silicon coated with metal oxides to tailor the electrochemical properties at the surface.

XPS analysis during etching experiments (Figure 3-4) investigated the intermixing of the gold and silicon interface. The understanding of the cross-section of this interface is key to determining the charge transfer processes that occur for photoelectrochemical stimulation. From etching experiments we identify an initial layer of metallic gold islands. Attenuation of the silicon signal indicates that the majority of the surface is metallic gold. Sputter coated gold has significantly higher coverage with a ratio of 67.32 % Au : 32.68 % Si. The ratio for e-beam evaporated gold surfaces showed a less significant surface coverage with a ratio of 41 % Au : 59 % Si. The ratio for PIN SiNWs with native gold was 0.05 % Au : 99.95 % Si. Upon further etching, an interface of gold silicide is identified. After 30 minutes of etching for sputter coated samples and 10 minutes for e-beam evaporated samples the gold percentage drops to about 3%. This indicates that the gold over-layer in sputter coating is more significant.

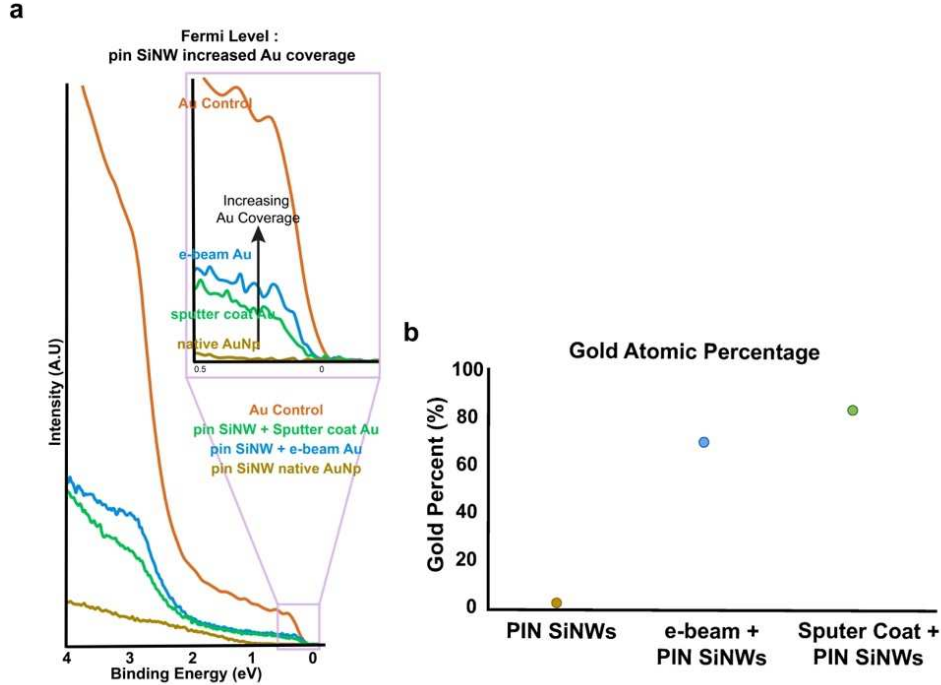


Figure 3-5. UPS characterization of electron density at the fermi edge of PIN SiNWs modified with gold.
a. UPS fermi edge shifts from metallic step for gold control (orange) to sloping semiconductor (yellow). The intermediate cases of sputter coated gold and e-beam evaporated gold have significant electron density at the surface resembling gold control. **b.** Atomic percentages indicate the shift from PIN SiNWs with native gold from CVD contamination around 1% while e-beam evaporated gold and sputter coated gold with approximately 80% and 90% respectively.

3.2.3.1 Metallic gold sputter coating and e-beam deposition shift structure and fermi edge

The UPS analysis provides information about the electron density at the fermi edge and the work function from the SECO. Semiconductors typically show a gentle decline to 0 at 1-2 eV. With metals, and the Ar⁺ ion sputter cleaned Au control the sample approaches 0 intensity with a sharp drop off at 0 eV. In Figure 3-5 the fermi edge shifts from semiconductor like surface to metallic like surface can be seen from the comparison of SiNWs with native atomic gold incorporation (<1% of surface atoms Si : Au) to SiNWs with native atomic gold incorporation with either subsequent e-beam deposition of gold or sputter coating of gold. The clear evolution towards a structure similar to the Au control is clear with increasing gold coverage. Native gold from PIN SiNW synthesis introduces < 1% atomic gold at the surface of the outer core of the SiNWs. As

examined previously, increasing the gold percentage at the surface shifts the work function towards that of atomic gold while remaining in the range expected for semiconductors. Alternatively, both sputter coating and e-beam deposition add metallic gold at the surface of the SiNWs. This shifts the work function towards that of metallic gold control 4.8 eV. The WF shifts from native gold PIN SiNWs 3.7 eV, sputter coated gold 4.3 eV, and e-beam evaporated gold 4.8 eV. This indicates that despite the fact that there is more metallic gold deposited from sputter coated gold the WF indicates that sputter coated gold produces a more metallic like sample. This variation significantly shifts the fermi level of the sample from a semiconductor like curve to a step structure similar to metallic gold. This indicates the addition of electron density at the fermi level based on the metallic layer.

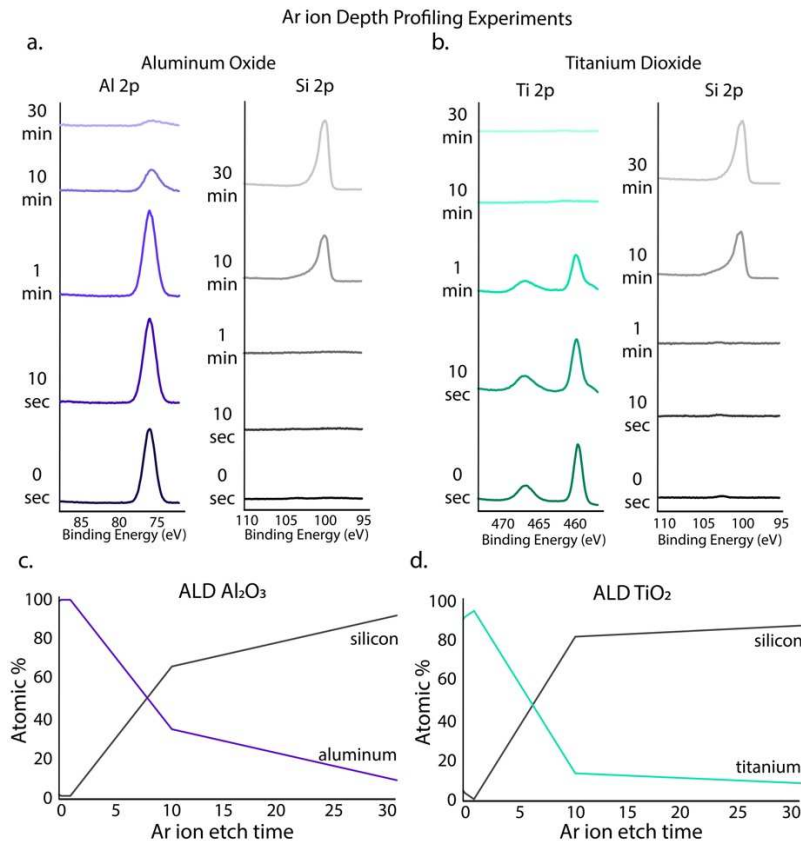


Figure 3-6. XPS depth of PIN SiNWs modified with metal oxides. a. Ar ion etching steps for aluminum (purple) and silicon (grey) indicate an intermixed interface at 10 minutes due to the steady decline in alumina

Figure 3-6 continued. signal while the silicon peak evolves. **b.** Depth profiling on titanium dioxide coated samples indicate titanium (green) and silicon (grey) over Ar ion etching steps. Depth profiling indicate a sharp interface with minimal intermixing. This is evident from the immediate shift from no silicon signal to silicon peak at 10 minutes. **c.** The atomic ratio calculated for alumina surface supports the steady decrease in atomic percentage due to interface intermixing. **d.** The atomic ratio calculation for titanium dioxide supports the sharp interface due to the dramatic drop in Ti signal.

3.2.3.2 ALD of TiO₂ on PIN SiNWs

Titanium dioxide has been shown to photoelectrochemically produce H₂O₂.¹⁰ As the PIN SiNW with native atomic gold also produce H₂O₂ this modification was studied to determine if it enhanced or limited the photocatalytic reactions. From Ar⁺ ion etching experiments (Figure 3-6 b) it was revealed that the TiO₂ as fabricated covered a majority of the SiNW surface.^{11,12} Before etching the ratio is 94.26 % Ti : 5.74 % Si indicating significant coverage of the silicon surface. After etching it is revealed that there is moderate intermixing at the interface. In the first ten minutes of etching the Ti : Si ratio increases indicated silicon is not exposed initially. This could indicate some significant intermixing of the TiO₂ and silicon during synthesis segregating a layer of silicon above the TiO₂. With further etching past 10 minutes the Ti signal decreases drastically. This indicates that there is not significant intermixing across the buried TiO₂ and silicon interface. The calculated work function of the TiO₂ – SiNW structures are 3.8 eV compared to a literature value of 4.06 eV. This indicates that the TiO₂ layer does not significantly shift samples from the PIN SiNW control.

3.2.3.3 ALD Al₂O₃ on PIN SiNWs

The surface modification of alumina on silicon is particularly interesting via ALD. The nature of the process provides significant intermixing at the interface. The alumina reactant used for ALD is highly reactive and this intermixing can be visualized by the depth of the Al signal identified by Ar ion etching. (Figure 3-6 a) The chemical ratio at 0 sec of etching, 97.62 % Al : 2.38 % Si, indicates almost complete coating of alumina over the SiNWs.^{13,14} The Ar ion etching

experiments interrogated the interface from ALD synthesis. The etching experiments showed a more gradual profile of chemical composition variation compared to gold or TiO₂ etching. The work function of Al₂O₃ – SiNWs is 2.7 eV, significantly shifted from the native SiNWs.

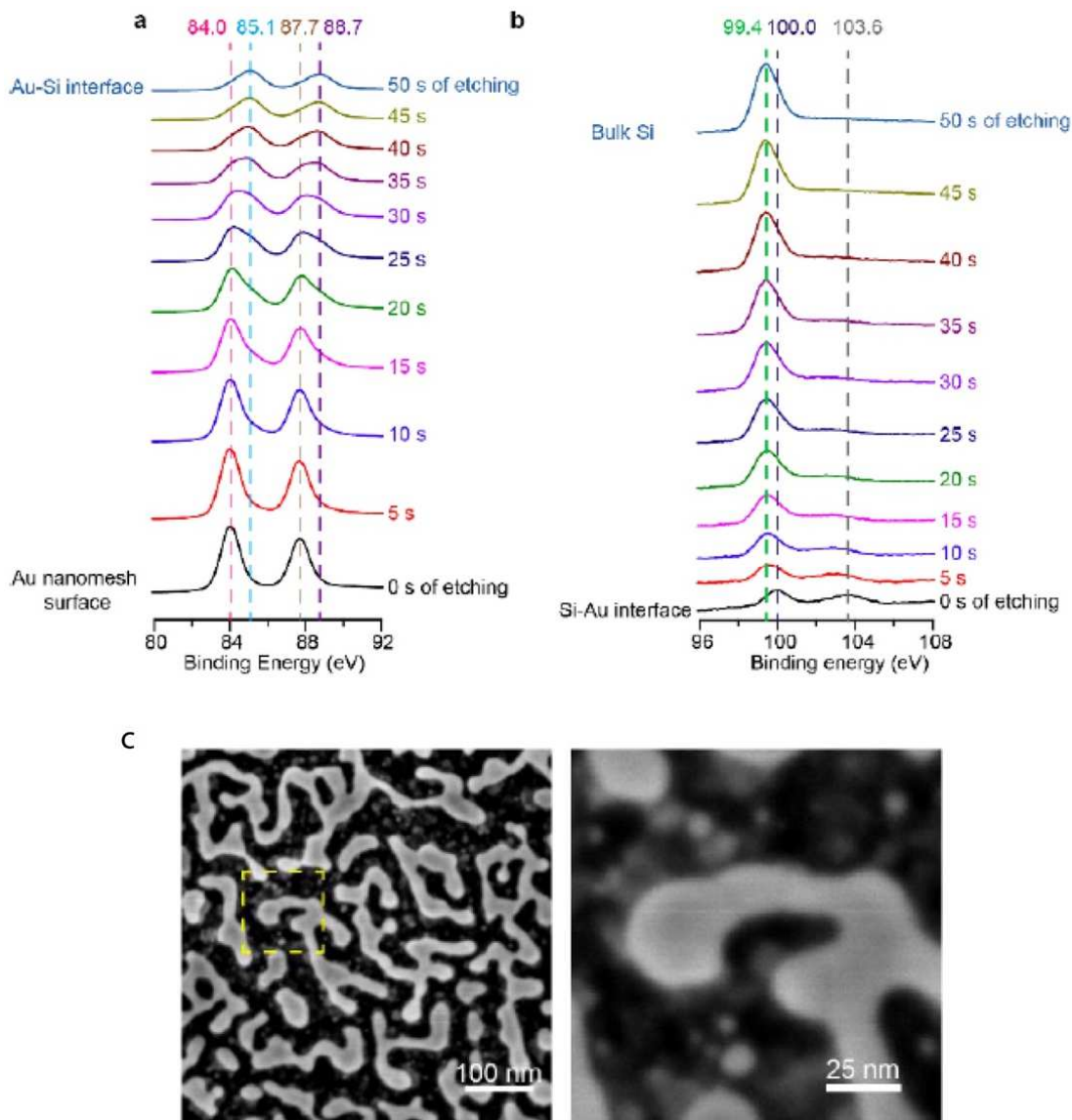


Figure 3-7. XPS depth analysis of gold nanomesh on silicon wafers. **a.** Ar⁺ ion etching was performed on wafers with gold islands. This reveals the intermixing of the Au-Si interface and metallic gold islands. The metallic sample occurs with predominantly 84 eV. After 15 sec of etching the gold silicide peak begins to evolve. **b.** The silicon peak under depth profiling indicates significant gold coverage before etching. This is clear from the attenuation of the silicon signal. After 10 seconds of etching the SiO₂ at the surface is completely removed. **c.** SEM images of the gold nanomesh over the surface of the silicon wafer. This confirms the presence of the metallic gold islands at the surface. Reproduced from Reference 1

3.2.4 Characterizing gold silicon interface of gold nanomesh on silicon heterojunction for optical stimulation at biointerfaces

To develop silicon nanostructure materials for new applications, especially biophysical purposes or biomedical devices, we need to fill in knowledge gaps regarding the physiochemical processes occurring under stimulation. These processes result from electrical, electrochemical, and thermal pathways under light exposure. We have characterized a range of silicon materials to quantitatively measure the different components of these physiochemical pathways to rationally design materials for biological applications. To accomplish this, we focused on a series of light induced processes at silicon and silicon-gold material interfaces in saline. These materials were then applied to optically controlling intracellular calcium dynamics and cellular excitability in vivo. For this study we measured silicon membranes with the as fabricated silicon heterojunction surface and compared it to gold nanomesh covering the silicon heterojunction. The gold nanomesh surface was fabricated via electroless deposition.¹⁵

3.2.4.1 Gold nanomesh structure provides evidence of an Au-Si interface promoting photoelectrochemical processes

The nature of the Au and Si interface will be key to understanding the photoelectrochemical processes at biointerfaces. To characterize this interface, we visualized the gold nanomesh silicon heterojunction through SEM and XPS depth profiling for chemical composition. SEM images demonstrate the nanomesh has interconnected large gold meshes surrounded by smaller nanoparticle sized isolated gold islands. The Au-Si interface is clearly variable based on the island structure. The nature of the gold silicon interface from this synthesis will be illuminate the potential charge transfer pathways between the Au and Si.

XPS depth profiling was used to identify the chemical composition at the Au and Si interface. For this experiment gold nanomesh silicon heterojunctions were measured before Ar ion etching and then intermediately at five second intervals up to 50 seconds of etching. The Au 4f signal shifted from predominantly metallic gold (84 eV) signal to intermetallic Au-Si alloy at 85.1 eV over the course of etching. It has been previously demonstrated that the shift in Au to higher BE can result from substrate effects, quantum size effects, and alloying effects; likely the reason dominated the BE shift in this case.^{16,17} This indicated that the structure was likely exclusively metallic gold islands at the surface. At about 25 seconds of etching the peak broadness indicated both the metallic (84 eV) and intermetallic Au-Si (85.1 eV), proof for a region of intermixing where part of the gold on the surface is metallic and part of the gold has been etched away revealing Au-Si alloy. This indicated that, as expected, the gold islands are not of uniform height and as the Au-Si interface is reached at different etching times. Additionally, the evolution of a second peak during etch experiments, while metallic gold signal is still present, indicates that the shift is truly an alloying effect and not a quantum size effect. At 50 seconds of etching the Au signal is predominantly intermetallic Au-Si. The extent of the gold at significant etching times indicates a region of predominantly Au-Si alloy. Examining the depth profiling effect on Si 2p signal provide information about the extent of gold coverage. The attenuation of the gold signal at 0 seconds of etching compared to the 50 second etching indicates that the gold layer does not completely cover the silicon surface. The structure is likely more gold isolated to nano-islands sat above the Au-Si regions surrounded by regions of exposed exclusively silicon. Additionally a second Si peak at 104 eV results from the SiO₂ signal. The relative height ratio of the Si to SiO₂ signal is close to one to one indicating significant oxidation at the surface. Within 10 seconds of etching this SiO₂

peak is almost entirely removed indicating the oxidation is isolated to the surface of the silicon heterostructure.

3.2.4.2 The measurements of photoresponse of silicon nanomeshes in solution provide insight into the effect on biointerfaces

The photoresponse of the various silicon heterojunction structures was measured via glass micropipette in PBS under light illumination. This allows us to measure two components of the photoresponse (1) photoelectric effects and (2) photothermal effects at biointerfaces. The photoelectric effect results in photogenerated charge carrier accumulation at the surface affect local surface potential and therefore ions in the media. For the photothermal effects the recombination of the photogenerated carriers transfer adsorbed photon energy into the vibrational energy of the Si lattice heating up the solution at the interface.

From analysis of the gold nanomesh on the silicon heterojunction we identified the presence of a transient capacitive charging and discharging processes at the Si/electrolyte interface and a secondary longer lived reduced amplitude current indicating faradaic current producing redox reactions at the Si/electrolyte interface. For metal free heterojunctions the major contribution was from the capacitive charging/discharging process with negligible contribution from the faradaic components. This indicates that there is minimal photothermal response for metal free samples. The significant amplitude of gold nanomesh silicon heterojunction indicates the gold provides a method of charge injection into the solution at the interface. This is likely tied to the identified Au-Si intermixing layers providing charge transfer pathways between the Au and Si. Additionally, increasing the metallic layer above the studied nanomesh reduced the amplitude of both the faradaic and capacitive currents due to the blocked light absorption and buried Si interface. This indicates that generated photoresponse in physiological solutions can be tailored by the

metallic interface but this effect is sensitive to the gold species, intermixing, and extent of coverage.

3.2.5 Conclusions and Outlook

Based on this series of XPS and UPS characterization methods we have been able to develop several methods of modifying the surface interactions of the SiNWs for photoelectric, photothermal, and photoelectrochemical stimulation. Two different approaches for functionalized SiNWs were developed through repeated cycles of XPS characterization. These methods utilize two different tethers, APTES and undecylenic acid. The APTES approach is based on plasma treated SiNWs with -OH groups for functionalization. In the second approach the hydrosilylation reaction is based on the HF treatment of SiNWs to produce a surface with -H groups. The two different methods result in significantly different SiOH signals and could be useful for photoresponsive applications that would benefit from either an insulation -OH surface or an -H surface for photovoltaics. For photothermal methods, we explored the impact of MACE etching on the surface of the SiNWs. This approach relied upon the deposition of metallic gold on the surface of the nanowires which was used to preferentially etch specific regions on the SiNW to increase the photothermal activity of the nanostructure. Finally, XPS depth profiling was demonstrated to be key to understanding the interface of both nanowires and wafers treated with gold or varied metal oxides. These structures can be used to alter photoelectrochemical activity at the silicon interface or to increase the photothermal activity of the structures for cellular stimulation. Based on the range of surface modifications explored here and the XPS and UPS based characterization outlined we have a wider platform of materials for photoresponsive activity at a variety of interfaces.

3.3 Experimental

XPS analysis : XPS data for SiNW samples were collected with the AXIS Nova (Kratos Analytical) with monochromatic Al K α X-ray source. The Al anode was powered at 10 mA and 15 kV. The instrument work function was calibrated to give an Au 4f_{7/2} metallic gold binding energy (BE) of 83.95 eV. Instrument base pressure was *ca.* 1×10^{-9} Torr. The analysis area size was 0.30.7 mm². For calibration purposes, the binding energies were referenced to Si 2p peak at 99.8 eV and/or C 1s peak at 284.5 eV. To improve reliability of the calibration. Survey spectra were collected with a step size of 1 eV and 160 eV pass energy. The high-resolution spectra of Si 2p and Au 4f were collected with a pass energy of 20 eV and 0.1 eV step size using 3 and 20 sweeps of 120 s for each sweep, respectively. XPS peaks were fitted with an asymmetric Gaussian/Lorentzian peak shape with linear background correction. Initial peak approximation model was based on the Au 4f peak modeling of the pure gold sample in order to better evaluate the asymmetric nature of the peak profile and the fit envelope.

Depth Profiling : After the initial survey spectrum and high resolution spectrum were collected, Ar⁺ ion etching was performed to measure the sample interface. The etching size was 3 mm² while the XPS analysis region was 300 x 700 μm^2 . The surface was bombarded with Ar⁺ ions for 10s, 30s, 10 min, and 30 min with XPS spectra collected after each cycle of etching. Etching was performed with Ar ion acceleration of 3 keV with beam currents of 1 mA. The relative ratios of gold and silicon were calculated from survey spectra after each round of etching to determine the elemental ratios with depth profiling.

3.4 Bibliography

- 1 Kempa, T. J. *et al.* Single and Tandem Axial p-i-n Nanowire Photovoltaic Devices. *Nano Letters* **8**, 3456-3460, doi:10.1021/nl8023438 (2008).
- 2 Cao, L. *et al.* Instability and Transport of Metal Catalyst in the Growth of Tapered Silicon Nanowires. *Nano Letters* **6**, 1852-1857, doi:10.1021/nl060533r (2006).
- 3 Tian, B., Xie, P., Kempa, T. J., Bell, D. C. & Lieber, C. M. Single-crystalline kinked semiconductor nanowire superstructures. *Nature Nanotechnology* **4**, 824, doi:10.1038/nnano.2009.304 (2009).
- 4 Luo, Z. *et al.* Atomic gold-enabled three-dimensional lithography for silicon mesostructures. *Science* **348**, 1451, doi:10.1126/science.1257278 (2015).
- 5 Pasternack, R. M., Rivillon Amy, S. & Chabal, Y. J. Attachment of 3-(Aminopropyl)triethoxysilane on Silicon Oxide Surfaces: Dependence on Solution Temperature. *Langmuir* **24**, 12963-12971, doi:10.1021/la8024827 (2008).
- 6 Khung, Y. L., Ngalm, S. H., Scaccabarozzi, A. & Narducci, D. Thermal and UV Hydrosilylation of Alcohol-Based Bifunctional Alkynes on Si (111) surfaces: How surface radicals influence surface bond formation. *Scientific reports* **5**, 11299-11299, doi:10.1038/srep11299 (2015).
- 7 Ohkura, Y., Weisse, J. M., Cai, L. & Zheng, X. Flash Ignition of Freestanding Porous Silicon Films: Effects of Film Thickness and Porosity. *Nano Letters* **13**, 5528-5533, doi:10.1021/nl403114g (2013).
- 8 Roder, P. B., Smith, B. E., Davis, E. J. & Pauzaskie, P. J. Photothermal Heating of Nanowires. *The Journal of Physical Chemistry C* **118**, 1407-1416, doi:10.1021/jp4078745 (2014).
- 9 Leontis, I., Botzakaki, M. A., Georga, S. N. & Nassiopoulou, A. G. Study of Si Nanowires Produced by Metal-Assisted Chemical Etching as a Light-Trapping Material in n-type c-Si Solar Cells. *ACS Omega* **3**, 10898-10906, doi:10.1021/acsomega.8b01049 (2018).
- 10 Yang, H.-Y., Rho, W.-Y., Lee, K. S., Kim, H. S. & Hahn, Y.-B. TiO₂ Nanoparticles/Nanotubes for Efficient Light Harvesting in Perovskite Solar Cells. *Nanomaterials* **9**, doi:10.3390/nano9030326 (2019).
- 11 Methaapanon, R. & Bent, S. F. Comparative Study of Titanium Dioxide Atomic Layer Deposition on Silicon Dioxide and Hydrogen-Terminated Silicon. *The Journal of Physical Chemistry C* **114**, 10498-10504, doi:10.1021/jp1013303 (2010).
- 12 Wei, D. *et al.* *Influence of Atomic Layer Deposition Temperatures on TiO₂/n-Si MOS Capacitor*. Vol. 2 (2013).
- 13 Igor Iatsunskiy, M. K., Mariusz Jancelewicz, Karol Załęski, Stefan Jurga, Valentyn Smyntyna. Structural and XPS characterization of ALD Al₂O₃ coated porous silicon. *Vacuum* **113**, 52-58 (2015).
- 14 Mandia, D. J. *et al.* The effect of ALD-grown Al₂O₃ on the refractive index sensitivity of CVD gold-coated optical fiber sensors. *Nanotechnology* **26**, 434002, doi:10.1088/0957-4484/26/43/434002 (2015).
- 15 Coluccio, M. L. *et al.* Electroless deposition and nanolithography can control the formation of materials at the nano-scale for plasmonic applications. *Sensors (Basel, Switzerland)* **14**, 6056-6083, doi:10.3390/s140406056 (2014).

- 16 Sohn, Y., Pradhan, D., Radi, A. & Leung, K. T. Interfacial Electronic Structure of Gold Nanoparticles on Si(100): Alloying versus Quantum Size Effects. *Langmuir* **25**, 9557-9563, doi:10.1021/la900828v (2009).
- 17 Zhao, L., Siu, A. C.-L., Petrus, J. A., He, Z. & Leung, K. T. Interfacial Bonding of Gold Nanoparticles on a H-terminated Si(100) Substrate Obtained by Electro- and Electroless Deposition. *Journal of the American Chemical Society* **129**, 5730-5734, doi:10.1021/ja070441j (2007).

Chapter 4 : Polymer composite with heterogeneous nanowire incorporation for free-standing silicon mesh

Reproduced from Parameswaran R*, Koehler K*, *et al.PNAS*2018¹

4.1 Introduction

The development of polymer – nanostructure composites has previously produced devices with properties beyond what is accessible for either one of the individual materials. The highly tunable nature of these materials including electrical, chemical, physical, and optical properties can be used to produce active photo-responsive materials. This structure takes advantage of the significant surface area of nanostructures for extensive polymer nanostructure interfaces. This high surface area provides properties such as entanglement with polymer chains or extended overlapping interface for accommodating stress and fractures.

Here we integrate PIN SiNWs with photoelectric properties^{2,3} into SU-8 polymer mesh that is photolithographically patterned. Specifically the integration process results in a heterogeneous profile of the polymer shifting to almost pure SU-8 at the base to a high density of nanowires in SU-8 at the surface. Additionally, as the structure is a grid with large window regions we produced a durable high density mesh of almost exclusively SiNW freestanding network. This resulted from the interaction at the SiNW polymer interface during UV exposure. We found evidence of thin filaments of SU-8 polymerized throughout the window region supporting the SiNW mesh stretched across a long window. This evidence suggested that a minimal base of SU-8 was polymerized due to the UV light at the surface of the SiNW which was acting as a thermal or optical guide.⁴ From this unique interaction we were able to fabricate a polymer-SiNW mesh with photoelectric properties, alterations in mechanical properties, and high water adhesion.

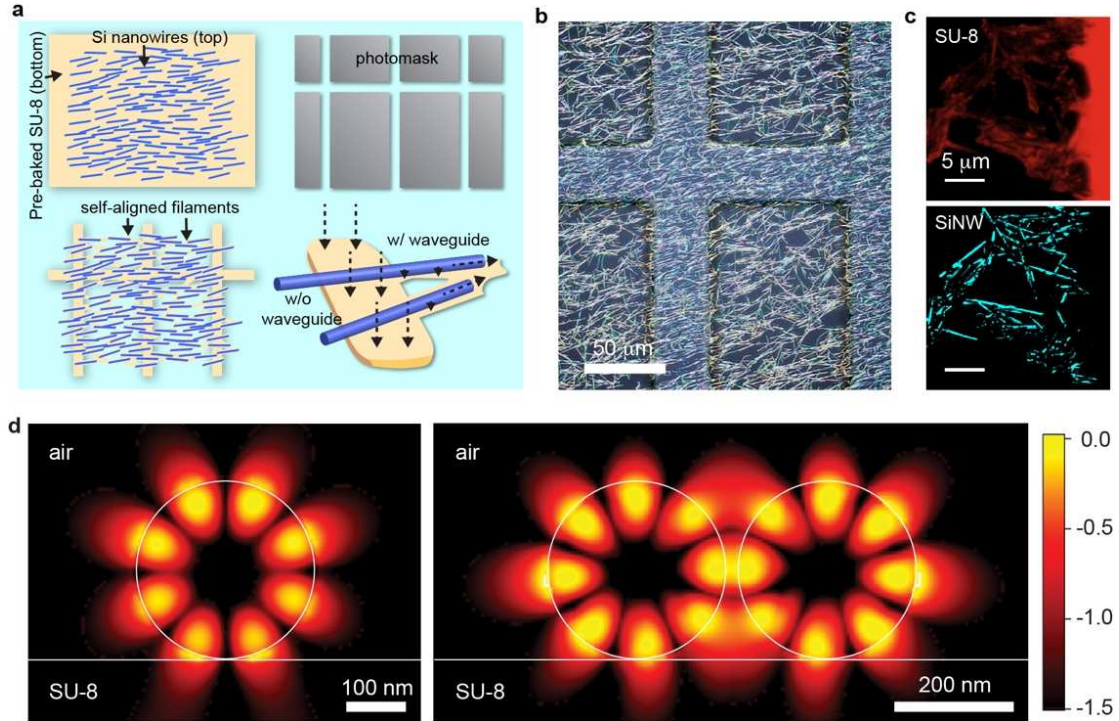


Figure 4-1. SU-8 scaffold fabrication produced a robust SiNW mesh due to SiNW waveguiding. **a.** Diagram demonstrates SiNW integration into SU-8 structure. During photolithography aligned SiNW direct UV light for polymerization of filaments through the window region. **b.** Laser scanning confocal color image of high density SU-8 PIN mesh. SiNW mesh can be visualized bridging the pattern gaps. Color image shows 3D reconstruction of height profile of SU-8-PIN mesh. **c.** Confocal microscopy image of thin SU-8 Film around SiNWs in SU-8-PIN gaps resulting from waveguiding properties of SiNWs. SU-8 is stained with Rhodamine 6G (red) SiNWs are shown in reflection channel (blue). **d.** Modeling of waveguiding effects of SiNWs in two arrangements, isolated SiNWs and parallel SiNWs, during photolithographic patterning with 365 nm exposure. Reproduced from reference 1

4.2 Results and Discussion

4.2.1 High density PIN SiNW mesh synthesis

To produce this high density PIN SiNW mesh we took advantage of the surface properties of the SiNWs on the silicon growth wafer. Core-shell SiNWs were synthesized via the previously discussed CVD method. We selected for PIN SiNWs on the small diameter range as this provided the highest density integration.⁵ SiNWs grown on the wafer were broken off the chip into the polymer substrate. This formed a high density network of SiNWs generally aligned across the surface. (Figure 4-1) During photolithography regions that were not exposed to light are not cross-linked. But taking advantage of the silicon nanowire surface and the light exposure can occur

minimally throughout the window regions. This results in a robust high density SiNW mesh that stretches between the SU8 bars. This mesh is linked together by thin ribbons of SU-8 stretching through the window region allowing for transfer of the substrate without nanowire loss. The result of this high density mesh is a modulated water interaction.

4.2.2 Nanowire polymer incorporation heterogeneous structure

The composite mesh structure that was fabricated had a heterogeneous profile with SiNWs segregated to the top of the 5 μm SU-8 polymer. This polymer formed a grid pattern with SiNWs on the surface of the polymer bars and window regions 86 μm x 424 μm with no substantial polymer and a mesh of SiNWs stretched across. The SiNWs were PIN SiNWs grown via CVD on the surface of a silicon wafer. Several different methods of SiNW integration were explored including drop casting, fabrication on the silicon wafer surface, and spin coating with SU-8 mixed with substrate free SiNWs. These other methods tended to result in either a very low density NW integration or a weak and damaged SU-8 polymer. For this reason we utilized mechanical transfer to integrate SiNWs into the polymer surface as it resulted in a high density NW incorporation and a heterogeneous structure with the NWs segregated and aligned at the surface. SU-8 photoresist was spin coated onto a glass slide and pre baked to remove solvent. Then the silicon growth wafer with the SiNWs was inverted and placed on the surface of the polymer. With a moderate amount of pressure and translation of the NW chip across the surface of the polymer, SiNWs are able to break off the wafer and are transferred in a semi-aligned manner to the surface of the polymer.

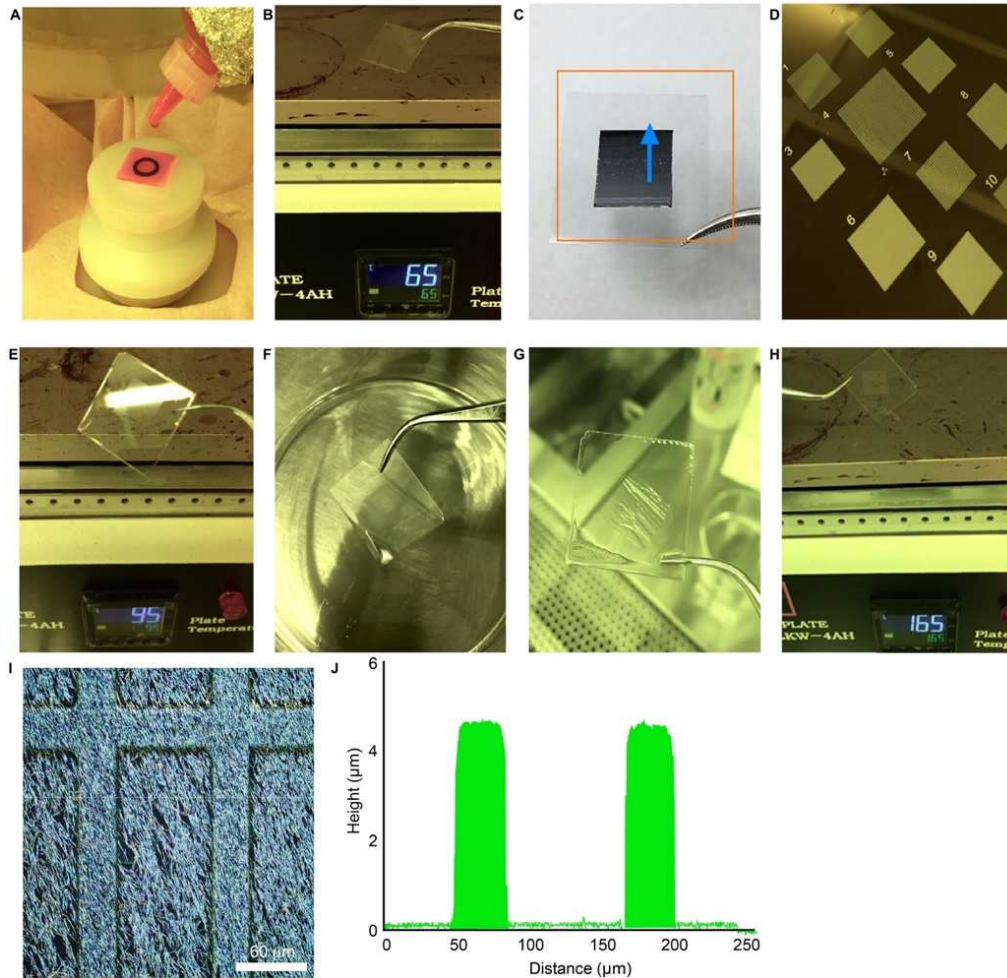


Figure 4-2. SU-8/SiNW meshes are prepared via a photolithographic patterning. SU-8 grid structure is fabricated via photolithography. **a.** SU-8 2005 precursor is spun onto a glass slide at 2500 rpm for 5 sec and 3500 rpm for 55 sec to form a 5 μm thick SU-8 layer on the glass slide. **b.** SU-8 precursor is heated to 65 $^{\circ}\text{C}$ for 180 sec and then 95 $^{\circ}\text{C}$ for 180 sec. **c.** After this pre-bake step, SiNWs are mechanically translated from the original growth wafer onto the surface of the SU-8. Orange box denotes glass slide with SU-8. SiNW growth wafer (SiNWs face glass slide) is translated across SU-8 surface in the direction of blue arrow, and SiNWs break off growth substrate and become embedded in the SU-8 surface. **d.** Samples are patterned via a chrome photolithography mask and hard contact lithography using a UV light exposure dose of 175 mJ. **e.** After exposure, samples are baked again at 65 $^{\circ}\text{C}$ for 180 sec and 95 $^{\circ}\text{C}$ for 180 sec for the post-bake step to crosslink SU-8. **f,g** Samples are developed in SU-8 developer for 30 seconds, rinsed in IPA for 15 sec, and dried under N_2 . **h.** Finally a post-bake step is performed at 165 $^{\circ}\text{C}$ for 20 min. **i.** Confocal reflected light microscope image showing a high density SU-8/PIN-SiNW mesh. **j.** Corresponding height profile from confocal reflected light 3D reconstruction of image (i) showing 5 μm height of SU-8/PIN-SiNW mesh. These height profile scans are representative of 30 scans from 30 different samples. Reproduced from reference 1

4.2.3 Photolithography and waveguiding

During the photolithographic process, after the SiNWs are incorporated, the SU-8 is exposed to UV light. (Figure 4-2) As SU-8 is a negative photoresist areas under direct illumination

are cross-linked and the window region, where light is blocked by the chrome mask no crosslinking occurs. In this window region the photoresist dissolves during the development stage. With the mask a grid with window regions of $86\ \mu\text{m} \times 424\ \mu\text{m}$ was produced. When the SiNWs were integrated we discovered the presence of extremely thin filaments of SU-8 supporting the SiNW mesh stretching across this large window region. Confocal microscopy (Figure 4-1 c) demonstrated the presence of these filaments. In this window region typically no polymerization would occur because there was no exposure to UV, but the SiNWs acted as an optical guide for minimal amounts of light exposure across the unexposed window region. (Figure 4-1) When no SiNWs were incorporated the polymer produced clean side walls with no filaments across the window region and no evidence of light leakage. To further demonstrate this effect, the UV exposure was increased to 400 mJ significantly higher than that required for the fabrication of $5\ \mu\text{m}$ thick structures. (Figure 4-3) With this drastically increased light exposure, the waveguiding effects of the SiNWs introducing UV light into surrounding regions increased significantly. From this we were able to produce measurable amounts of SU-8 in the window regions. (Figure 4-3, d,f,g,h) In the absence of the SiNWs no SU-8 crosslinking in the window regions occurred. (Figure 4-3 c,e) The combination of visualized polymer ribbons supporting the SU-8 structure and the visualization of the exaggerated effect with higher UV exposure both occurring with SiNWs and disappearing without indicates that the nanostructure surface was key to introducing the optical waveguiding effect. The significant crosslinking in the window region in Figure 4-3 g,h with low SiNW loading dose due to higher diameter SiNWs opens up questions regarding the effect of SiNW structural variability on the wave guiding effects during photolithography.

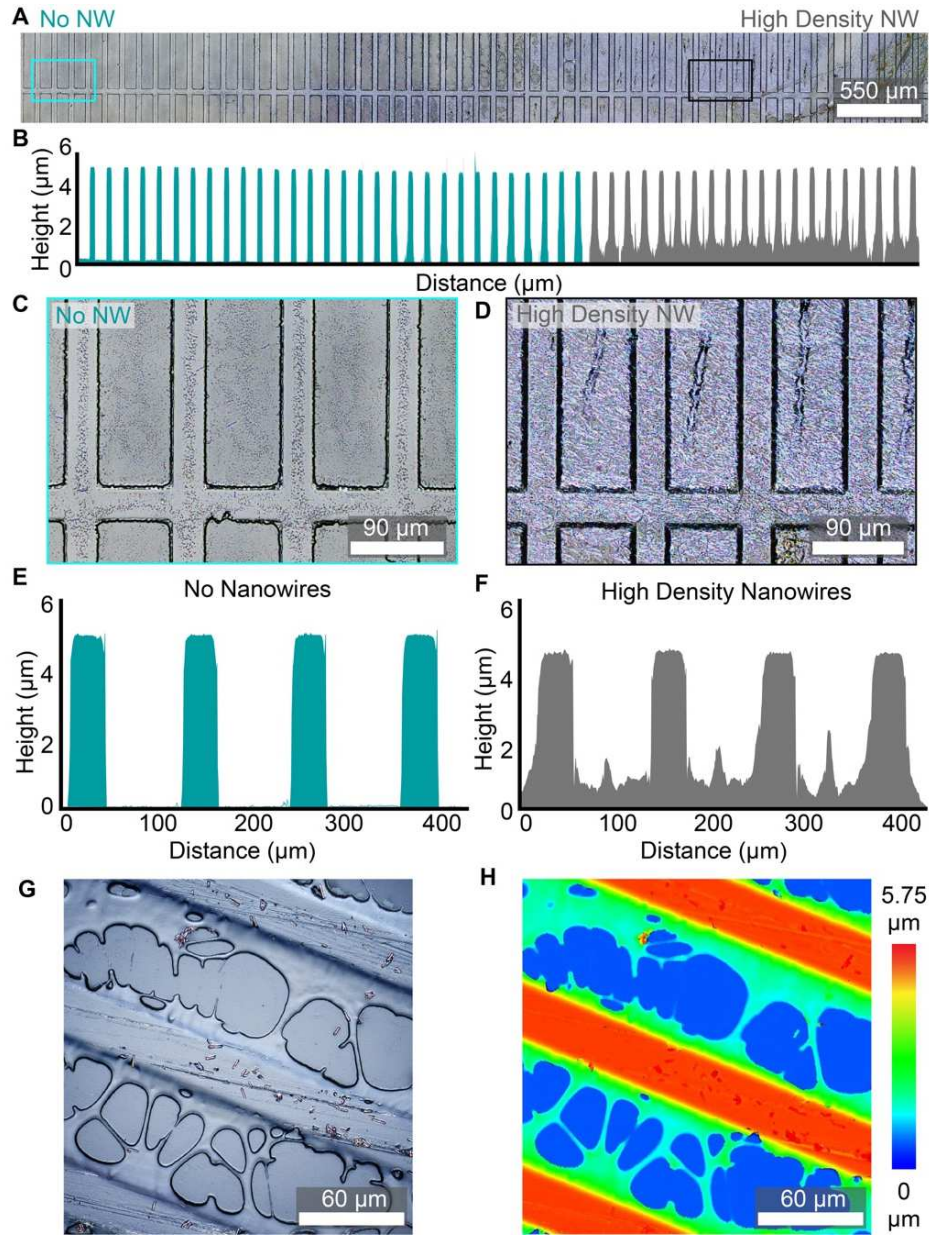


Figure 4-3. SiNWs waveguide light during the UV exposure. **a.** Confocal 3D reflected light microscopy widefield color image of SU-8 mesh with a very high UV exposure dose (400 mJ) fabricated with SiNWs only present in the right half. A higher exposure dose was intentionally used here (higher than that of normal sample preparation in all other parts of the text) to enhance the over-exposure of the SU-8 film in the window regions, so that it is detectable in 3D reconstruction. This higher exposure dose does not cause excessive SU-8 crosslinking in the window regions in the absence of nanowires. **b.** Height profiles reconstructed from confocal 3D data of the SU-8 mesh in (A). This displays the existence of SU-8 film in the mesh window regions in the presence of high density SiNWs (gray traces) and minimal SU-8 in the window regions with negligible SiNWs (blue traces). These are representative traces of 4 different meshes. **c,d.** Zoomed in confocal 3D images of the SU-8 mesh from (A) in the presence of SiNWs (black box inset from (A)) and in the absence of nanowires (blue box inset from (A)). **e,f.** Height profiles reconstructed from laser scanning confocal 3D data of SU-8 mesh regions in (C) and (D), respectively. **g,h.** Laser scanning confocal color image and 3D reconstruction of the effect of low loading dose of SiNWs with higher UV exposure from previous samples. Reproduced from reference 1

4.2.4 Modeling light transfer to surrounding regions

To understand the impact of the NWs serving as optical guides during the lithography process we performed finite-difference time-domain (FDTD) simulations to model the extent of light leakage. The FDTD model demonstrated that the SiNWs in a mesh structure operate synergistically to guide UV light towards neighboring SiNWs. This UV exposure produces an evanescent field of light that is waveguided around the surface of the SiNW and results in the SU-8 polymerization of polymer ribbons to support the aligned high density SiNW mesh. The FDTD simulations of the waveguide modes were used to calculate the intensity profiles for single and multiple nanowires sitting on an SU-8 substrate. For these simulations the SiNWs were estimated to be 300 nm based on the core-shell SiNW structure. Examining two parallel SiNW in the x-y plane separated by 20 nm, we found that a dipole source on the left SiNW produced waveguide modes coupled to the adjacent SiNW at $\pm 7 \mu\text{m}$ in the x plane.

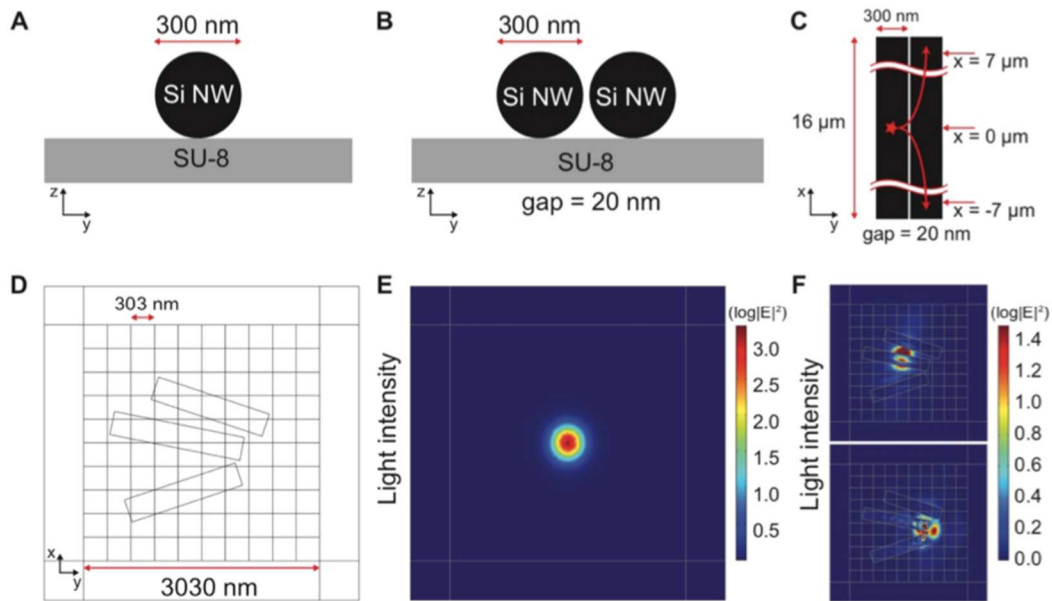


Figure 4-4. 3D FDTD and FEM Simulations demonstrate nanowire waveguiding. a-c. 3D FDTD simulations to calculate intensity profiles of waveguide modes in single and double SiNWs on the SU-8 substrate. The SiNWs with a diameter of 300 nm are positioned along the x-axis in the calculation domain with a size of $16000 \times 1200 \times 550 \text{ nm}^3$. Cross-sectional views of **a.** a single SiNW and **b.** double SiNWs with a gap

Figure 4-4 continued. of 20 nm. **c.** Top-view of the double SiNWs. Dipole sources are introduced in the $x=0$ plane in the left SiNW. Waveguide modes are coupled to the right SiNW and detected in the $x=\pm 7$ nm plane. The time-averaged intensity profile of the waveguide mode with the strongest intensity. **d-f.** 3D FEM simulations to calculate light absorption in SiNWs. **d.** Simulation domain with a size of $3030 \times 3030 \times 3000$ nm³ which is digitized by 10×10 pixels in the x - y plane. Three SiNWs with diameters of 300 nm are introduced. The surrounding is water with a refractive index of 1.33. **e.** Horizontally-polarized Gaussian beam with a wavelength of 514 nm and a spot size of 520 nm, which scans across the calculation domain. **f.** Calculated light intensity ($\log |E|^2$) for two different pump positions (top and bottom). The field profiles are shown in the $z=0$ plane. Reproduced from reference 1

4.2.5 Photoelectric effect

The choice of PIN SiNWs for integration into SU-8 mesh was based on the previously demonstrated photoelectric properties of core-shell SiNWs with this doping profile. Under light exposure, two parallel processes; photoelectric and photothermal can occur in the SiNWs.^{2,3,6} The photoelectric process results in light generated carriers accumulating at the surface of the SiNW. The coaxial PIN SiNWs are designed with two components facilitating photoelectric process. The first is a core shell doping profile which integrates a diode junction to support efficient charge separation of photogenerated carrier. The photoelectric effect of these PIN SiNWs was previously demonstrated by the stimulation of dorsal root ganglion neuron cells.² The second is the presence of atomic gold surface states from the CVD growth process which can act as a catalyst for reducing the barrier to photoelectric processes at the surface. Under light illumination, generated holes and electrons are pushed towards the p-type core while the electrons are swept into the n-type shell. The carriers accumulated at the surface creating a photogenerated potential at the silicon water interface can attract or repel ions in media creating ionic currents. Alternatively, photoelectrochemical processes can occur at the surface based on this current generation. The gold can reduce the potential barrier for these photoelectrochemical processes by facilitating electron injection at these surface states into the electrolyte solution through a cathodic reaction (reducing protons). The photogenerated holes instead move to the p-type core and are either consumed in recombination events or by chemical reaction at the exposed surface at the end of the wire. This

process is significantly slower as the surface area of the p-type core is drastically smaller than the n-type shell surface as well as the lack of gold catalyst in this region.

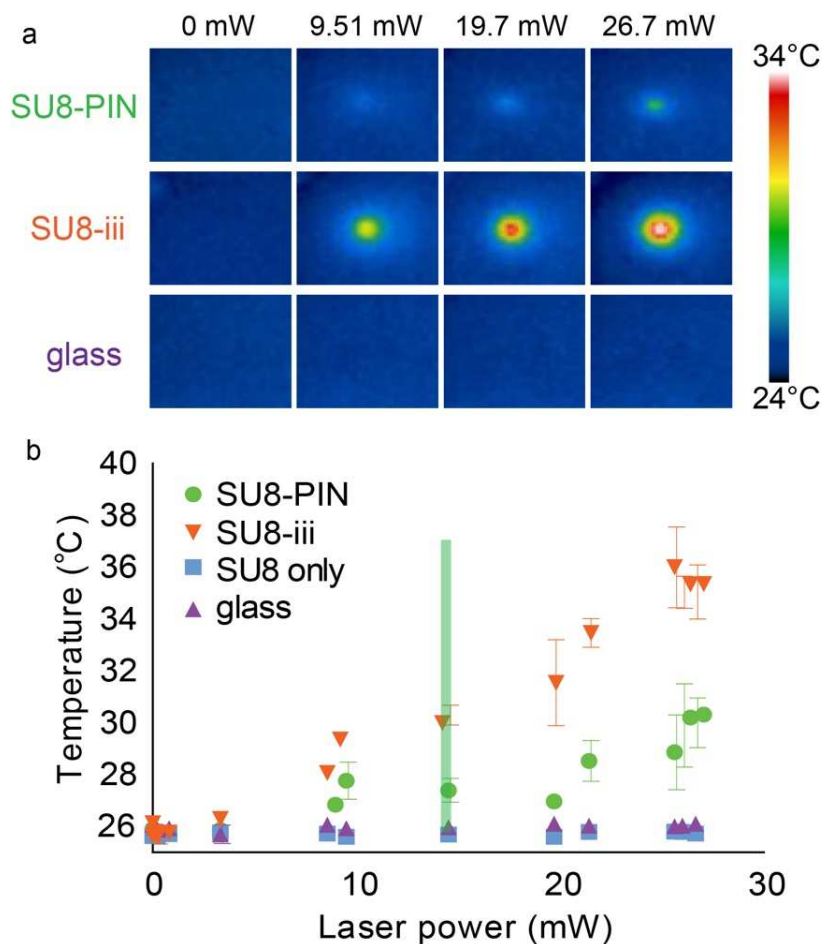


Figure 4-5. Photothermal response of PIN SU-8, III SU-8, SU-8 only, and glass. a. IR camera images of the SU-8-PIN mesh being exposed to 532 nm laser light focused through a 5X objective at various laser powers. **b.** Graph indicates photothermal response of each sample with a series of laser powers. The laser power used for *ex vivo* heart training is highlighted in green. Reproduced from reference 1

The alternative process is photothermal. In this process the generated carriers experience recombination events converting the input energy of the photon into vibrational energy in the silicon lattice. In solution we have measured this energy as dissipated heat through the silicon into the surrounding electrolytes based on elevated local temperatures. With this choice we were able to fabricate an active material for optical and wireless photoelectric or photoelectrochemical

stimulation at the device surface. We also characterized the photothermal contribution to understand which of these two parallel processes dominated at the device interface under illumination. (Figure 4-5) Using an infrared camera, we assessed the temperature increase caused by laser stimulation of the SU-8-PIN mesh. The PIN SU-8 mesh under 19.7 mW laser stimulation had a 1.1 °C increase in temperature at the stimulated region. We compared this to III SiNW SU-8 mesh structures because this SiNW doping profile has no built in photodiode junction to support the photoelectric process. For III SiNW SU-8 meshes we observed a temperature increase of 5.4°C. This indicates that the primary mechanism for the PIN SiNW SU-8 mesh is photoelectric with a smaller component of photothermal response due to the minimal temperature increase induced by laser stimulation.

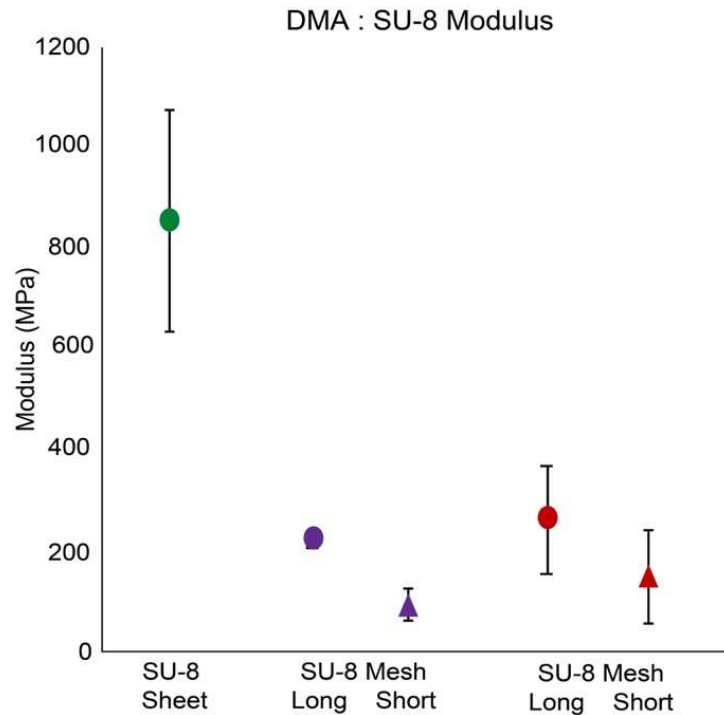


Figure 4-6. Reduction of SU-8 Modulus after fabrication with microstructure and nanostructure. The modulus of the SU-8 structures were assessed via dynamic mechanical analysis. Modulus for each sample was calculated from the average values of the region of linearity within 0.01% - 15% strain.

4.2.6 Mechanical measurements

SU-8 is a well explored polymer for photolithography applications because it is rugged and durable with a Young's modulus of 2 Gpa.⁷ In the typical fabrication conditions SU-8 structures are very inflexible. In addition to the waveguiding properties and increased water adhesion the SiNW integration into the SU-8 and the patterned grid structure provided significant flexibility to the SU-8 SiNW mesh without compromising the durability. To further explore the impact on the mechanical properties we measured the reduction of modulus. The modulus of SU-8 structures were measured via DMA (Figure 4-6) to calculate the modulus of PIN SU-8 mesh and SU-8 sheet. We found that SU-8 PIN mesh showed significant reduction in average Young's modulus, 2.6×10^8 (horizontally) and 1.2×10^8 (vertically) as compared to 7.1×10^8 Pa for a SU-8 sheet. This demonstrates the fabrication method reduces both structures from the traditional modulus for SU-8 and that the gridded structure and nanostructure integration further reduces the modulus compared to the SU-8 sheet. This type of modulus reduction makes the SU-8 SiNW mesh useful for applications to soft biological surfaces where the polymer interfaces with soft low modulus tissues. Additionally, dynamic mechanical analysis tests confirmed the stability of the mesh during repeated cyclic stretching, indicating that the reduction of modulus does not compromise the durability of the fabricated structures.

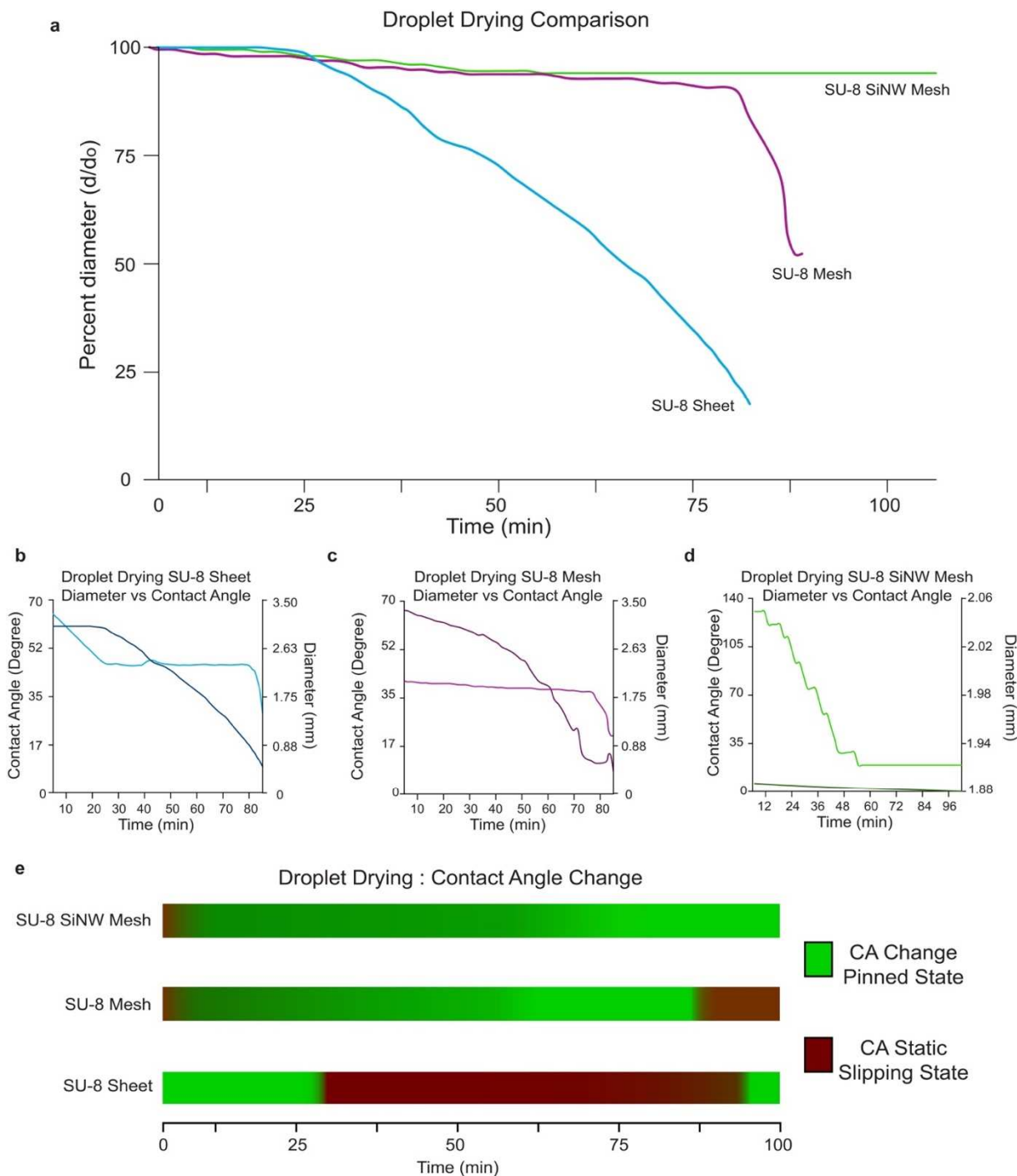


Figure 4-7. Droplet adhesion measured through pinning of droplet edges during drying. **a.** Drying of 2-3 μL droplets of DI water on SU-8 sheet (purple), SU-8 grid (blue) and SU-8/PIN-SiNW mesh (green). Drop diameters are tracked during the drying process to identify the pinned and slipping regimes. Droplet diameter is scaled by plotting the ratio of diameter/max diameter for each sample. (representative of $N=4$ samples for each type of SU-8 structure.) **b-d.** Each individual droplet drying experiment is plotted with both diameter and contact angle versus time. SU-8 sheet (purple), SU-8 grid (blue) and SU-8/PIN-SiNW mesh (green). Light graph corresponds to contact angle and dark graph corresponds to droplet diameter. The static contact angle indicates slippage and the changing contact angle indicates pinning. **e.** The data for contact angle change is integrated into horizontal graph for visualizing the alteration of adhesion with each successive change in micro or nanostructure.

4.2.7 Increased water adhesion properties based on nanostructured surface

Nanostructured surfaces have been well explored for the potential to increase water adhesion due to pinning of the water droplet.⁸ This is similar to the biomimetic effect exploited based on the hierarchal nanostructured rose petal surface. The basis of this strong adhesion and pinning is a result of van der Waals and capillary forces at the nanostructure water interface. From this basis we can identify micro and nano patterned surfaces with strong water pinning interactions.

To characterize the water nanostructured-polymer water interface we measured contact angle variations based on the SiNW SU-8 mesh, SU-8 mesh with no SiNWs, and SU-8 sheet. We observe a shift from hydrophilic SU-8 sheet with a contact angle of 72.88° to 114.51° for the hydrophobic SiNW SU-8 mesh. The hydrophobic / hydrophilic nature of a materials surface can be dictated by chemical composition or surface structure. The shift from SU-8 sheet to SiNW SU-8 mesh changes mainly the structure of the surface with minimal impact on chemical composition as the SU-8 synthesis process does not change.

To get a deeper understanding of the water adhesion at that interface we observed the drying of a water droplet on the surface of the SiNW polymer device.⁹⁻¹³ This allows for an interrogation of the pinning of the water droplet to the nanostructures on the surface. Droplets of 2-3 μm were placed on the surface of SiNW SU-8 mesh, SU-8 mesh no SiNWs, and SU-8 sheet. For samples with high adhesion, during the drying process, the edges of the droplet pin to the surface and the droplet diameter change is minimal until the volume of the droplet was too small to support the large surface area. At this point droplet edges slip inwards. For samples with low adhesion the height of the droplet does not change during drying, but the edges continually slip inwards in the absence of pinning. For SU-8 sheet samples there is no nanostructure or microstructure to provide pinning effects. The droplet edges on SU-8 sheet slip inwards

continually until the droplet is fully evaporated. For both samples of SU-8 mesh (either with or without SiNWs) show stable droplet diameter almost until the droplet is 100% evaporated indicating the microstructure photolithographic pattern provides adhesion for droplet edge pinning. The mesh samples without SiNWs slip significantly during the last 5% of droplet drying while the mesh with SiNWs show no significant diameter change through the entirety of the drying process. From this comparison we observe that the nanostructured surface provides a secondary component aiding in droplet pinning. Examining a more detailed analysis of the SU-8 SiNW mesh we observe the small diameter changes occur in a step wise fashion as droplet edges jump from one pinned region to the next. From this water-device interface analysis we can identify the different contributions of microstructure of the patterned SU-8 polymer and the nanostructure of the SiNW integration.

4.2.8 Conclusions and Outlook

Based on this work, we have established a unique material with mechanical, photoelectric, and water – material interfaces with properties that directly result from the microstructure and nanostructure of the SU-8 SiNW mesh. The integration of PIN SiNW with previously demonstrated photoelectric properties provides not only photoresponsive properties, but also provides for a durable and flexible mesh that is stable under significant strain. Additionally, the microstructure and SiNWs pins water to the surface of the material to significantly increase material adhesion to water. These unique functionalities make this material ideal for cellular stimulation or tissue interfaces. Specifically, the integration of PIN SiNWs makes this material especially useful for interfacing with electrically responsive cells such as cardiomyocytes or neurons.

4.3 Experimental

SU-8 SiNW Mesh Synthesis : Coaxial pin silicon nanowires (PIN-SiNWs) were synthesized as previously described by Parameswaran et al. using a gold (Au) nanocluster-catalyzed chemical vapor deposition (CVD) process. iii-SiNWs, consisting of intrinsic Si cores and intrinsic Si shells, were synthesized using the same growth process as that of PIN-SiNWs except with only silane and hydrogen carrier gas, and 30 min growth time for core growth and 30 min for shell deposition. SU-8 structures were fabricated using SU-8 2005 (MicroChem) permanent epoxy negative photoresist via photolithographic patterning. SU-8 precursor was deposited onto IPA and acetone-cleaned glass coverslips via a two-step spin coating (add company) protocol: (1) 5 sec at 2500 RPM (2) 55 sec at 3500RPM. Samples were pre-baked at 65°C for 180 s and 95°C for 180 sec. PIN-SiNWs or iii-SiNWs attached to their growth substrate were cleaned in a 10% HF solution for 90 sec, rinsed in DiH₂O, and dried under N₂ (g) in order remove the oxide layer. SiNWs were subsequently integrated into the pre-baked SU-8 precursor via mechanical translation. During mechanical translation, SiNW wafers were laid atop the SU-8 surface such that the SiNWs and SU-8 precursor were in direct contact and translated with light pressure across the surface. An EVG 620 semi-automatic double side mask aligner was used to photolithographically pattern samples. UV light source for exposure was 365 nm with a 175 mJ exposure dose. A quartz mask fabricated at Argonne National Labs with various grid patterns. A post-exposure bake of the sample was subsequently performed at 65°C for 180 sec and 95°C for 180 sec. Samples were developed in SU-8 developer solution (MicroChem SU-8 Developer) for 30 sec and rinsed in IPA for 15 sec. A final post-bake was then performed at 165°C for 20 min. Quality of 2 samples from each batch was assessed by a profilometer (Bruker Dektak XT-S Profilometer) to check 5 μm height of the resultant SU-8-SiNW mesh and integrity of the sidewalls of the mesh.

Dynamic Mechanical Analysis (DMA) : SU-8-PIN meshes were first lifted off of the glass slides they were fabricated on by HF etching with 48% HF for 20 s at room temperature. The SU-8-PIN mesh were rinsed six times in 3 mL of DI water to remove all HF from solution. They were then transferred to a film tension clamp adapter of Dynamic Mechanical Analyzer (RSA-G2 TA Instruments) and adhered to the tensile testing clamp with Scotch tape. The samples were tested over a range of 0.01% - 15% strain. Modulus data was calculated from the average values of the region of linearity within 0.01% - 15% strain.

Drop Shape Analysis (DSA) : SU-8 structures were lifted off glass slide in similar manner to that in the DMA experiments above. Samples were deposited onto acrylic scaffolds with a laser cut 6 cm diameter hole. The meshes were positioned above the gap and were loaded onto the drop shape analyzer (Kruss DSA100). Sessile drops of 2-3 μL were formed on the DSA needle above the SU-8 structures. Drops were brought into contact with the SU-8 and the needle was pulled away to leave the drop on the surface of the material. Contact angles are measured with the sessile drop method. An average of at least 10 samples were measured from different synthesis batches to ensure consistency. Droplet pinning was analyzed by recording a video of the drying process of 2-3 μL sessile drops. Contact angle and drop diameter are tracked through the process to identify pinning of water during droplet evaporation for at least three of each type of sample.

Analysis of NW waveguide film : SU-8 structures were fabricated as described above, except samples were positioned in such a way that the region exposed contained 50% pristine SU-8 and 50% with integrated SiNWs within one pattern. To visualize a more expansive film the dosage was raised to 400 mJ because at this dose, SU-8 with NW has an easily visualized film but SU-8

with no nanowires has clean sidewalls and expected height. Samples from one synthesis and exposure with SiNWs integrated into only one half were analyzed by laser scanning confocal to visualize and profile the transition from pristine SU-8 with clean sidewalls to SU-8 with 1 μm film. For visualization of the true minimal SU-8 film present around NW due to waveguiding, SU-8 with the highest density of Rhodamine 6G (Sigma Aldrich Cas #989-38-8) was made by adding excess Rhodamine 6G, sonicating for 5 min to dissolve the maximum amount and removing supernatant SU-8 precursor. SU-8-PIN mesh with high density Rhodamine 6G was fabricated by the previously described method. The presence of Rhodamine 6G impacted the minimal dose required for films stable to development so a dosage test was performed and analyzed by laser scanning confocal to find the minimal dose for stable samples with vertical sidewalls and 5 μm height. This minimal dose with the addition of Rhodamine 6G was found to be 600 mJ. SU-8-PIN Rhodamine 6G mesh with vertical sidewalls, 5 μm height, and no presence of macroscale film were visualized on Leica SP5 confocal (63x lens 1.4 NA). SU-8 shell around SiNW in the gaps of the pattern was visualized with the Texas Red channel and the 514 notch filter to ensure no reflection was captured and SiNWs were visualized in reflection mode on the 514 nm laser line.

Temperature measurements : An infrared camera (FLIR E8) was used to measure temperature changes in SU8-PIN-SiNW meshes on glass coverslips, SU8-iii-SiNW meshes on glass coverslips, SU8 grids on glass coverslips, and glass substrates alone upon illumination with a 532 nm DPSS laser (LaserGlow). For each sample, laser light was increased from low to high power in even increments. Infrared images of the samples were taken with the laser light on approximately 30 sec after the power was increased.

4.4 Bibliography

- 1 Parameswaran, R. *et al.* Optical stimulation of cardiac cells with a polymer-supported silicon nanowire matrix. *Proceedings of the National Academy of Sciences* **116**, 413, doi:10.1073/pnas.1816428115 (2019).
- 2 Parameswaran, R. *et al.* Photoelectrochemical modulation of neuronal activity with free-standing coaxial silicon nanowires. *Nature Nanotechnology* **13**, 260-266, doi:10.1038/s41565-017-0041-7 (2018).
- 3 Tian, B. *et al.* Coaxial silicon nanowires as solar cells and nanoelectronic power sources. *Nature* **449**, 885, doi:10.1038/nature06181 (2007).
- 4 Ding, J. S. a. J. (IntechOpen, 2011).
- 5 Silva, E. C. C. M., Tong, L., Yip, S. & Van Vliet, K. J. Size Effects on the Stiffness of Silica Nanowires. *Small* **2**, 239-243, doi:10.1002/smll.200500311 (2006).
- 6 Zhang, J. *et al.* Photovoltaic Performance of Pin Junction Nanocone Array Solar Cells with Enhanced Effective Optical Absorption. *Nanoscale Research Letters* **13**, 306, doi:10.1186/s11671-018-2727-7 (2018).
- 7 MicroChem. SU-8 Permanent Photoresists.
- 8 Law, J. B. K., Ng, A. M. H., He, A. Y. & Low, H. Y. Bioinspired Ultrahigh Water Pinning Nanostructures. *Langmuir* **30**, 325-331, doi:10.1021/la4034996 (2014).
- 9 Bussonnière, A. *et al.* Universal wetting transition of an evaporating water droplet on hydrophobic micro- and nano-structures. *Soft Matter* **13**, 978-984, doi:10.1039/C6SM02287A (2017).
- 10 Wang, F. & Wu, H. Molecular origin of contact line stick-slip motion during droplet evaporation. *Scientific Reports* **5**, 17521, doi:10.1038/srep17521 (2015).
- 11 Park, S.-G. *et al.* Surface Energy-Controlled SERS Substrates for Molecular Concentration at Plasmonic Nanogaps. *Advanced Functional Materials* **27**, 1703376, doi:10.1002/adfm.201703376 (2017).
- 12 Li, H., Fowler, N., Struck, C. & Sivasankar, S. Flow triggered by instabilities at the contact line of a drop containing nanoparticles. *Soft Matter* **7**, 5116-5119, doi:10.1039/C1SM05097D (2011).
- 13 Annavarapu, R. K., Kim, S., Wang, M., Hart, A. J. & Sojoudi, H. Explaining Evaporation-Triggered Wetting Transition Using Local Force Balance Model and Contact Line-Fraction. *Scientific Reports* **9**, 405, doi:10.1038/s41598-018-37093-6 (2019).

Chapter 5 : Novel x-y plane scanning based stimulation method paired with photovoltaic polymer - SiNW composite for optical stimulation of isolated cardiac cells.

Reproduced from Parameswaran R*, Koehler K*, *et al.PNAS*2018¹

5.1 Introduction

The disruption of electrical conduction system for cardiomyocytes is a potentially fatal issue for patients suffering from these disorders. These failures can come in the form of disconnected beating or general slowing of cardiac beating frequency. Understanding how to address and interrogate electrical conduction between cardiomyocytes will be key to the development of new therapeutic solutions. To investigate this we study the stimulation of isolated neonatal rat cardiomyocytes to beat at target beating frequencies. Previous studies have demonstrated the significant potential for optogenetic therapies to tailor cardiomyocyte beating frequencies.^{2,3} Additional approaches have shown the potential of implementing a 534 nm picosecond laser stimulation paired with gold nanoparticles for photothermal based changes in beating frequency of HL1 cells as well as neonatal rat cardiomyocytes.⁴

Here we develop a novel x-y scanning based stimulation method paired with a photovoltaic SU-8 PIN SiNW mesh for an effective low radiance method of altering isolated neonatal rat cardiomyocyte beating frequency. This method benefits from the fact that it is a non-genetic approach for optical stimulation and provides effective stimulation without the requirement for high intensity laser irradiance. For this scanning based approach the high density SiNW scaffold is key as it provides a large number of cardiomyocytes nanowire interfaces key to cellular stimulation. For this approach we take advantage of the high density of SiNW cellular interfaces.

The moving laser input scans the silicon-biointerfaces producing a high frequency moving stimulation interface mimicking the natural inputs cells see from many different sources in vivo.

For this stimulation approach cells experience periodic (low frequency) pulse trains (high frequency) at intervals of the desired final beating frequency. During one stimulation event cells do not experience the typical one to one laser stimulation input, but instead the x-y movement of the laser produces a high frequency series of pulses. Over a period of time the cellular beating frequency slowly increases to periodic (low frequency) targeted frequency. Target frequencies were based on baseline beating frequency of the isolated cells. The result of these periodic pulse trains is the ability to utilize a significantly low-radiance optical stimulation series to produce an increase in cellular beating to the target frequency that is not phase locked with laser pulses.

The general approach is (1) identifying baseline beating frequency through florescence imaging (2) Stimulating with the x-y moving laser in ON/OFF cycles of pulse trains at the target frequency (3) Measuring post-stimulation beating frequency via florescence imaging as feedback for identifying if another cycle of measurement-stimulation-measurement is required. Once the step (3) indicates cells have reached target frequencies cells were monitored to identify the memory effect duration.

5.2 Results and Discussion

5.2.1 Cell – material interface

For this stimulation method we utilize both a large stimulation large area of light exposure and small laser spot size and as a result this method avoids pitfalls of other stimulation methods. Addressing the first component without any prior understanding of the bio interface it avoids the issue of missing the cell-material interface region for optimal stimulation. The integration of the

biocompatible high density SiNW mesh ensures that there are many options for cell-material interfaces with strong interactions that would be ideal for stimulation. Secondly, it allows for reduced laser irradiance required to produce a cellular response compared to other methods. The estimated average stimulation radiant exposure is $\sim 1.3 \text{ mJ/cm}^2$ for each training frame. This is on the lower range of most non-genetic biological modulation methods.^{1,4-15} This takes advantage of the extensive network of SiNWs providing a wide region capable of absorbing laser light and stimulating a contraction while reducing the phototoxic response produced at high laser exposure. Taken together this moving laser stimulating many different cell-material interfaces and the waveguiding effect of the SiNWs providing low light intensity based on random interface junctions provide a biomimetic approach to stimulation. Typically, cellular events are triggered when many stimuli are detected by receptors and membrane proteins. The cardiac cells are able to integrate the stimuli from chemical, mechanical, thermal, or electrical signals that are highly transient and arrive from diverse regions across the cell to direct cellular function. Most synthetic cellular stimulation methodologies are not able to recapitulate this type of random, small, and spatially diverse inputs. From this method integrating a high density SiNW network capable of producing a photoelectric response from two levels of light exposure including (1) a fast moving illumination source and (2) a waveguiding effect from the SiNW clusters.

5.2.2 Stimulation method

Here we replace one single high intensity pulse with a high frequency pulse train resulting from the laser scanning rows of pixels. In parallel to this the scanning laser passes across a high density mesh of SiNWs previously demonstrated to produce a waveguiding effect. This effect distributes lower intensity light pulses to regions outside of the defined laser spot. The moving laser stimulus ensures that every cell-SiNW interface is illuminated at a high frequency with varied

intensity over a time period significantly shorter than the period of cellular contraction. This stimulation method is able to produce two levels of light illumination at the SiNW surface providing a random, fast, transient and spatially distributed burst of light generated physiochemical responses because the SiNW network is combined with the (1) x-y movement of the stimulation laser combined with the (2) waveguiding of light from SiNW network to surrounding regions at reduced intensities.

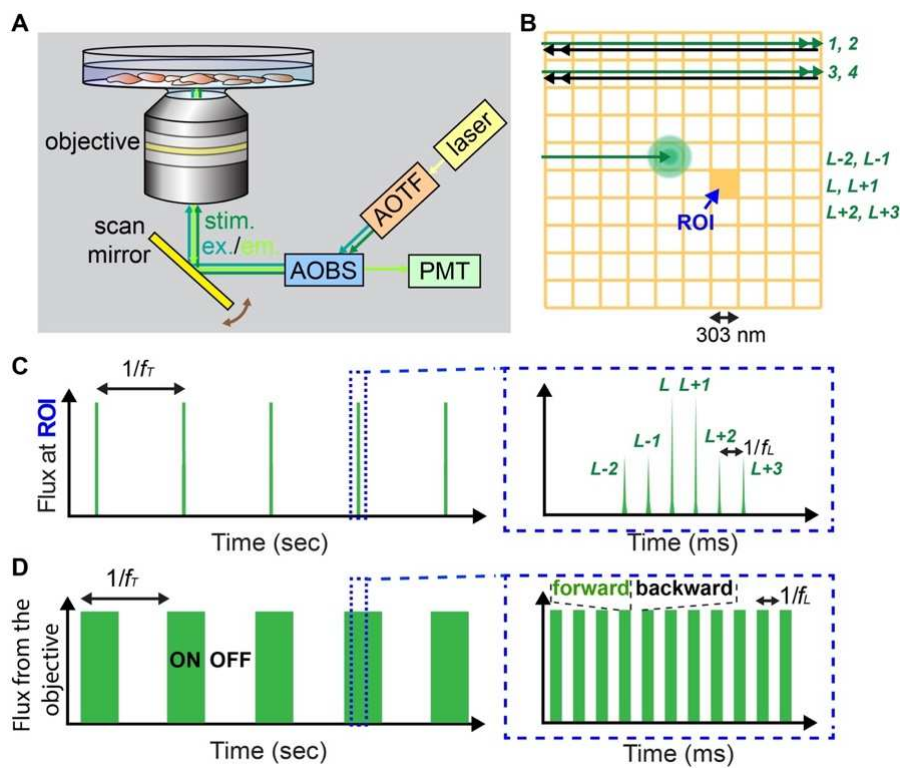


Figure 5-1. x-y scanning based stimulation method for altering cellular activity. **a** Confocal microscopy set up used to stimulate primary neonatal cardiomyocytes cultured on SU-8-PIN mesh. Laser light originates from the laser source and passes through the acousto-optical tunable filter (AOTF) (green horizontal arrow) where the 514 nm laser line is selected and attenuated to desired intensity. This is focused through the 40x objective lens (green vertical arrow) to a point on the sample. For Fluo-4 calcium imaging, the fluorescence emission and reflection from the sample (orange arrow) pass back through the acousto-optical beam splitter (AOBS), removing reflection and selecting desired emission wavelength. This beam passes through the pinhole, to remove out of focus light, to the photomultiplier tube (PMT) detector, where the signal is converted to an analog photon count resulting in greyscale pixel values for pixels of 303 nm x 303 nm (gray pixel grid). During stimulation of the cells, the 514 nm laser spot (green spot) with an airy disk diameter of 500 nm. **b.** Laser is scanned line by line at 1 kHz (black arrow on top of green spot). The resulting overlap of an airy disk radius larger than the pixel height causes a series of varied intensity high frequency laser pulses **c.** Schematic of stimulation scheme, where laser is set to scan at a desired frequency by programming a set “on” period where the laser scans the full area pixel by pixel and then a set “off” period where no laser scanning occurs. Here, “on” and “off” period times are set so there is a gap between stimulations giving a stimulation frequency with a duty cycle of 50%. Within one

Figure 5-1 continued. scanning “on” period, (blue dashed inset) one pixel will experience a series of 1kHz pulses of direct laser intensity when the laser is directly focused on that specific pixel (green trace schematic). These direct pulses are in a pattern of 2 low (L-2, L-1), 2 high (L, L+1), and 2 low (L+2, L+3) intensity pulses based on the line being scanned and the overlap of the airy disk with the pixel of interest. In the 1 ms gaps between direct laser events (green trace schematic) **d**. The diagram here demonstrates the flux over the entire pixel grid resulting in the 50% duty cycle for training. $1/f_T$ is the frequency of stimulation based on frame time, and is generally between 0.5 Hz – 2 Hz. Blue inset demonstrates the forward and backwards ‘on’ and ‘off’ scan of the laser across the pixel grid (yellow). $1/f_L$ gives the line scan frequency which is set at a constant 1000 Hz based on laser scanning rate. Reproduced from Reference 1

5.2.2.1 Scanning stimulation in the x-y plane

The scanning stimulation paces cells to a specific frequency required stimulation ON and OFF periods with the ON/OFF durations at a frequency (f_F) set by the target beating frequency (0.5 - 2 Hz) and duty cycle (50%). During the ON period the laser scans over an area of $\sim 0.09 \mu\text{m}^2$ at a frequency of 1-kHz per line (f_L). Within this on period there are series of shorter windows where the laser is on in the forward direction and off in the backwards direction. Essentially this results in the laser scanning line by line on in the forward direction off in the backwards direction with a line scan of two for the entirety of the ON period. Following this there is an OFF period where there is no stimulation and no scanning. During the ON period the stimulation laser was a $0.6 \mu\text{W}$ 514 nm laser with a diffraction limited spot of approximately 500 nm diameter is scanned line by line. The region illuminated was about $\sim 0.09 \mu\text{m}^2$ or 1,024 pixels with a pixel size of 303 x 303 nm. Based on the line scan rate of 1-kHz and the pixel size, the pixel scan rate is 1.024 mHz.

Addressing just the ON period we can interrogate the flux at one specific pixel to approximate the stimulation at a single cell-SiNW interface. During one ON period a single pixel will have six primary incident fluxes resulting from the fact that a pixel is 303 nm and is smaller than the diffraction limited airy disk diameter of the laser. This means that one pixel will experience a primary incident flux for the line before the pixel, the line of the pixel, and the line after the pixel with varying intensity depending on the location of the center of the airy disk. To ensure that any stimulative effect is efficient each line is scanned twice. With two scans per line

and three lines providing overlap with the laser spot, that results in six primary incident fluxes at a distribution of $1/f_L$ or 0.001 seconds.

After this ON then the designated OFF period occurs when there is no stimulation or scanning. Then the ON/OFF cycle will begin again for the designated stimulation period. Through this combination of high frequency inputs it is possible to produce a periodic (low frequency) series of pulse trains (high frequency) that effectively pace cells to the targeted periodic frequency while requiring a low laser radiance. We identified the radiant exposure over the full stimulation region to be $\sim 1.3 \text{ mJ/cm}^2$. This is significantly lower than what was required for wide field illumination of cardiomyocyte SiNWs system and is more effective than single point illumination.

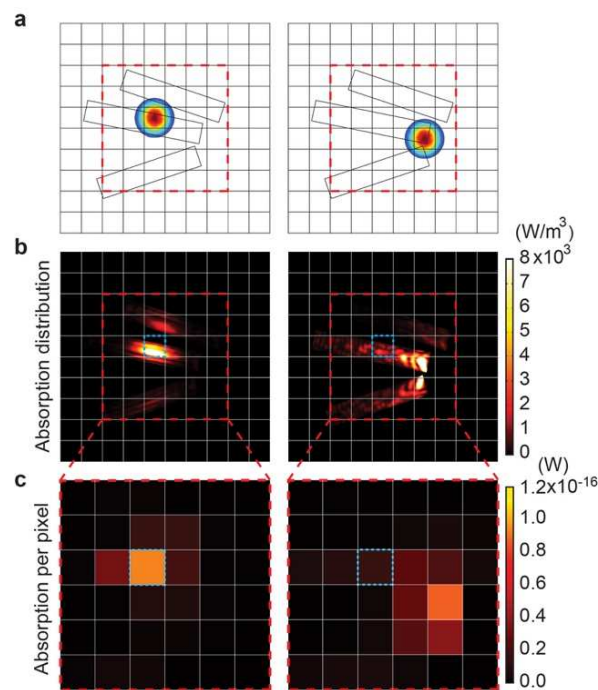


Figure 5-2. Simulations demonstrate nanowire waveguiding during scanning based stimulation. a-c. FEM simulation to calculate a map of light absorption in regions with SiNWs in a pixel grid. **a.** Three 300-nm-diameter SiNWs are introduced for proof-of-concept demonstration, and two different pump positions are examined. **b.** The wavelength and spot size of the pump light are set to 514 nm and 520 nm, respectively. **c.** The calculated absorption distribution in each pump position is used to plot the 6 x 6 digitized absorption matrix. In the bottom panel, the absorption per pixel is calculated by integrating the absorption distribution in each single pixel with a volume of $303 \times 303 \times 400 \text{ nm}^3$. We also mark the same pixel as a blue dotted box for a clear comparison of the pump position-dependent absorption. Reproduced from Reference 1

5.2.2.2 Simulating the waveguiding properties of SiNW network

In concert with the scanning based stimulation providing a range of transient laser inputs spatially distributed across the cell surface, the SiNW network contributed to We preformed 3D finite element method (FEM) analysis of SiNW groups under optical illumination. For 3D FEM simulations a cluster of 300 nm SiNWs were investigated in water with a refractive index of 1.33. The laser parameters were a 514 nm wavelength, a spot size of 520 nm, and horizontally polarized Gaussian beam based on parameters from the confocal laser used for cellular stimulation. As the stimulation laser rasters across the x-y plane we calculated light intensity for the laser at two different regions. Comparing the laser spot size in a region with no SiNWs to the laser spot when it is located on top of the nanowires it is clear that SiNW waveguiding effect produces large more variable light spot distributions. Specifically, we found that the position of the laser and the SiNWs can produce drastically different effects based on both the laser spot location on SiNWs (ie end vs center of SiNWs) and the orientation of SiNWs adjacent to stimulated SiNW. From this simulation data we can identify how the laser rastering over the x-y plane of the high density SiNW mesh can produce low level laser stimulation in pixels outside of the region directly under stimulation.

5.2.3 Demonstrated cellular viability on PIN SiNW scaffold

To demonstrate the method of stimulation combining the x-y scanning based stimulation with the PIN SiNW mesh we cultured neonatal rat ventricular cardiomyocytes on the substrate. Composite meshes were coated with fibronectin and seeded with isolated cardiomyocytes. The grid structure promoted alignment of cells along the long grid axis mimicking the orientation of cells grown in vivo. Alignment of cells in this manner has been shown to support contractile activity and expression of gap junctions at physiologically relevant locations. This cellular orientation was verified via immunofluorescence staining for cardiac troponin (red) demonstrating that cells align within the mesh and are geometric external to the mesh due to no structural

direction. Electrical connectivity is demonstrated by staining for gap junction staining are visualized by connexin-43 (green). To confirm the formation of a solid biomaterial interface between cells and SiNWs we visualized cells grown on the scaffold via SEM. Cells were shown to wrap around SiNWs forming tight junctions. This indicates that there will be many PIN SiNW – cardiomyocyte interfaces ideal for stimulation. The biocompatibility of the scaffold is verified via a live/dead viability assay. The viability assay demonstrated that cellular viability is not impacted by growth on the fibronectin coated PIN SiNW SU-8 scaffold vs fibronectin coated glass. We also found that there was no light induced phototoxicity based on equivalent cardiomyocyte percent viability for cells before and after laser stimulation.

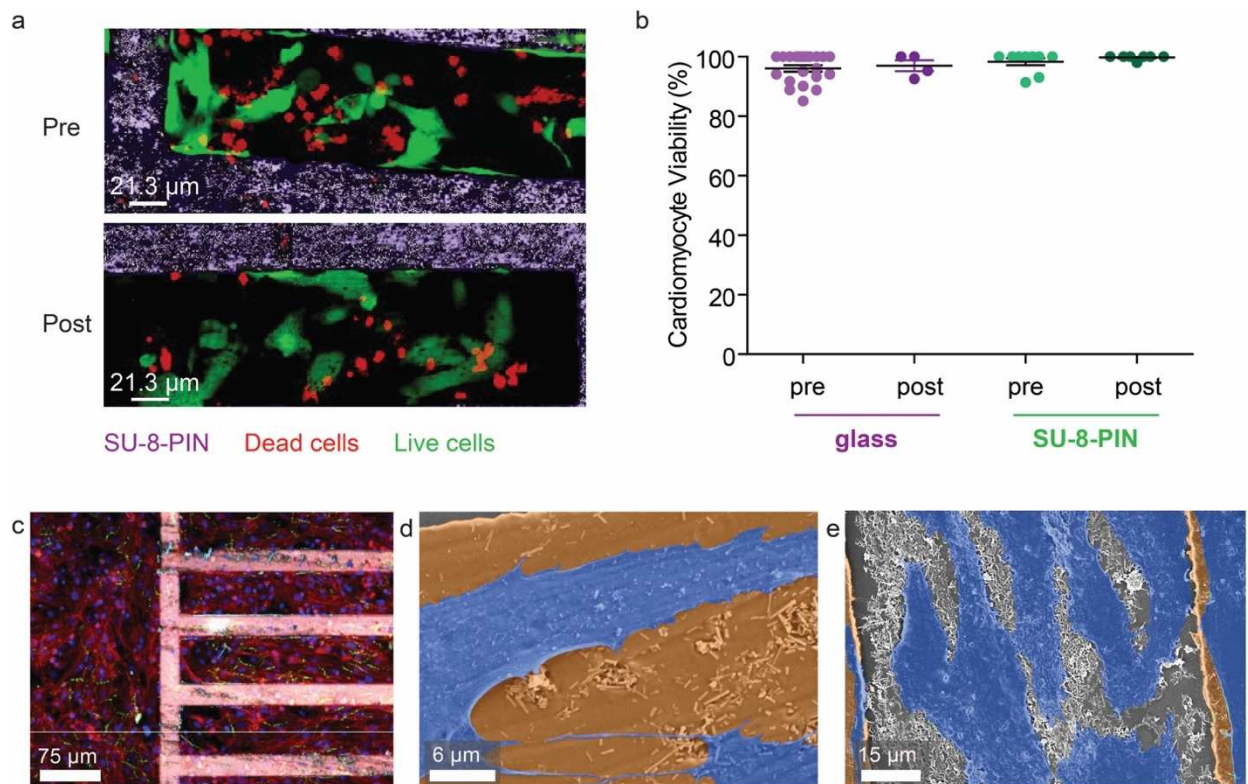


Figure 5-3. Biocompatibility is demonstrate by viability assay and cellular alignment on the SU-8 substrate. a. Live/Dead staining of cardiomyocytes and cardiac fibroblasts cultured on fibronectin coated SU-8/PIN-SiNW meshes before optical training (top) and after optical training (bottom). Live cells are green, dead cells are red, and the SU-8/PIN-SiNW mesh is purple. **b.** Percentage of live cardiomyocytes cultured on glass (purple) and the SU-8/PIN-SiNW mesh (green) before and after optical training (lighter dots and darker dots,

Figure 5-3 continued. respectively). Only cardiomyocytes were counted (not fibroblasts) and cardiomyocytes were distinguished from fibroblasts by cell morphology. Each point represents the percent viability from one image taken from a total of 4 different glass samples and 3 different SU-8/PIN-SiNW meshes. Percent viability was calculated from 21, 4, 9, and 7 images for glass pre training and post training, and SU-8/PIN-SiNW pre-training and post-training, respectively. Averages and standard error are indicated with a black horizontal line and black bars above and below average, respectively. **c.** Confocal microscopy image of primary neonatal cardiomyocytes cultured partly on a fibronectin-coated SU-8-PIN mesh and partly on fibronectin-coated glass. Mesh is stained with Rhodamine B (pink) and cardiomyocytes are stained with anti-troponin (red), anti-connexin 43 (green), and DAPI (blue). **d-e.** Scanning electron microscopy image of primary neonatal cardiomyocytes (blue) cultured on a fibronectin-coated SU-8-PIN mesh (SU-8 grid in orange and PIN-SiNWs in white). Association between cells and SiNWs indicated a high density of cell – SiNW material interfaces. Reproduced from reference 1

5.2.4 Optical stimulation of cardiomyocytes to alter cardiac beating frequency

This stimulation method as defined previously was then used to stimulate cardiomyocytes to beat at the designated target frequency. Generally, the stimulation procedure involved (1) pre-stimulation identification baseline cardiomyocyte beating frequency using immunofluorescence and (2) scanning based stimulation with defined ON/OFF cycles at the target frequency then (3) measuring post stimulation beating frequency as a feedback. After one cycle the change in the baseline beating frequency is measured, this feedback is used determine if more stimulation cycles are required. For the immunofluorescence monitoring of beating frequency cells were stained with Fluo-4 to track intracellular calcium flux. Based on this measured baseline beating frequency the target frequency is identified. To demonstrate the potential of this stimulation method, we visualize one representative experiment targeting cells to a beating frequency of 700 mHz. The pre-stimulation beating frequency of cells fell between the range of 0 – 669 mHz. After four stimulation cycles separated by 2 minute breaks cells trended towards the target frequency of 700 mHz. With each cycle the average beating frequency increased towards the target frequency and importantly the frequency distribution narrowed as cells began to beat in phase as opposed to the random distribution of the baseline cells.

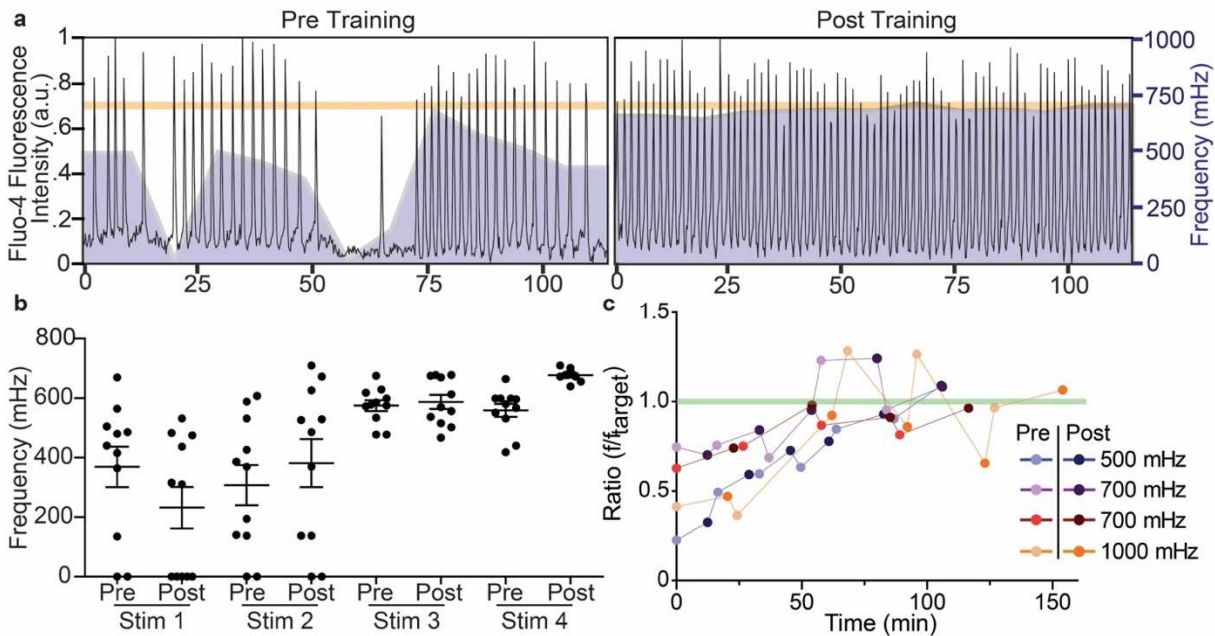


Figure 5-4. Cellular stimulation with defined x-y scanning method demonstrates effective pacing of cells. **a.** Fluo-4 calcium imaging traces (black traces) depicting pre training and post training beating patterns for a single cell for a span of 107.8 seconds from a group of eleven cardiomyocytes that were trained to beat at 700 mHz (yellow line). A running average of frequencies every 18 seconds were plotted (11 data points total) behind the black traces to show how consistently the cell was beating before and after the training (purple mountain plot). Fluorescence trace indicates that cells after four cycles of training pace up to targeted beating frequency and become more consistent. **b.** Average frequencies for each 18 second interval for the cell depicted in part a above are shown for each stimulation period throughout the training. The stimulation periods were 20.98, 25.64, 25.64, and 25.64 minutes between each pre and post 1-4, respectively. 11 frequencies are plotted for each pre and post condition. **c.** Average beating frequencies were plotted as ratios of the beating frequency to the target beating frequency over time for cells from four different training experiments. 14 cells were used in the 500 mHz experiment (blue), 2 cells in the first 700 mHz experiment (purple), 5 cells in the second 700 mHz experiment (red), and 7 cells in the 1000 mHz experiment (orange). Pre optical stimulation and post optical stimulation beating frequencies are depicted with lighter colored dots (pre) and darker colored dots (post). The green line indicates the target frequency. Connections between dots do not represent real data and are included as a way to visualize the trend. Reproduced from reference 1

To verify that the stimulation method did not itself produce this pacing effect, we measured cardiomyocyte control on SU-8 meshes, SU-8 III SiNW meshes, as well as on a glass substrates. (Figure 5-5) III SiNWs lack a significant photoelectric response due to the lack of built in electric field from photodiode structure. For all control samples cells did not trend towards targeted stimulation frequency. As an additional control we measured the stimulation effects observed for SU-8 PIN SiNW meshes. For these experiments we found that we were able to stimulate cells

adjacent to the laser spot to beat close towards the target beating frequency. The required radiant exposure to elicit this response was significantly higher than the scanning based stimulation method at about $\sim 44 \text{ mJ/cm}^2$ per pulse, compared to the $\sim 1.3 \text{ mJ/cm}^2$ for scanning based stimulation. The cost of this higher intensity exposure was significantly cytotoxicity at the laser spot region.

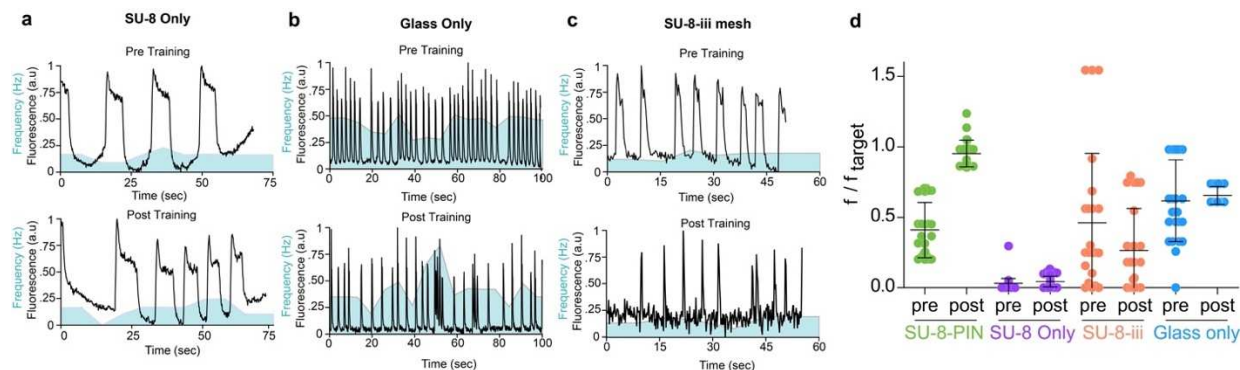


Figure 5-5. Optical stimulation of cardiomyocytes on SU-8 grids, glass, and SU-8/III-SiNW meshes do not result in training. a-c. Fluo-4 calcium imaging traces (black traces) depicting pre- and post- training beating patterns for a single cell from groups of (a) 9 and (b) 8 cardiomyocytes that were trained to beat at 700 mHz for (A) 42.24 min (4 stimulation periods) and (b) 42.25 min (4 stimulation periods) of total stimulation time on fibronectin-coated a SU-8 only, b glass only, and c SU-8/III-SiNW mesh. A running average of frequencies every 18 seconds were plotted behind the black traces to show how consistently the cell was beating before and after the training (blue mountain plot). These are representative traces of 6 different experiments with a total of 65 cells for the glass condition and 5 different experiments with a total of 34 cells for the SU-8/III-SiNW condition. d. Comparison of optical stimulation of cardiomyocytes on various substrates and with various stimulation break times. Comparison of optical training efficacy of cardiomyocytes cultured on fibronectin-coated SU-8/PIN-SiNW meshes (green), SU-8/III-SiNW meshes (orange), or glass (blue). Efficacy was determined by plotting the ratio of the beating frequency of individual cells ($N=29$ for SU-8/PIN-SiNW pre and post; $N=23$ for SU-8/III-SiNW pre and post; $N=25$ for glass pre and post) to the target beating frequency before and after optical training (pre and post, respectively). These values were taken from 4 separate stimulation experiments for the SU-8/PIN-SiNW condition in which cells were paced to 500, 700, or 1000 mHz; 3 for SU-8/III-SiNW condition that were all paced to 700 mHz, and 2 for the glass condition that were paced to 700 or 476 mHz. Points with the same values are sometimes overlaid. Reproduced from reference 1

5.2.5 Importance of break times for cellular stimulation

One key component we identified during this process was the break time between stimulation cycles. During this period, the feedback from the previous stimulation is tracked to determine the parameters for the next cycle. Additionally, we showed that this two minute break time was key to cellular memory of stimulation. We observed that on most cases the post

stimulation beating frequency of one cycle was significantly lower than the next pre-stimulation beating frequency. From this information we identified the 2 minute rest period to be key to the slow increase towards the target frequency. When the break time was lengthened to 10 minutes cardiomyocytes were unresponsive to stimulation and did not increase to targeted frequency. This inability to alter beating frequency with longer break times indicated that this period interfered with the target cells ability to “remember” the previous stimulation cycle.

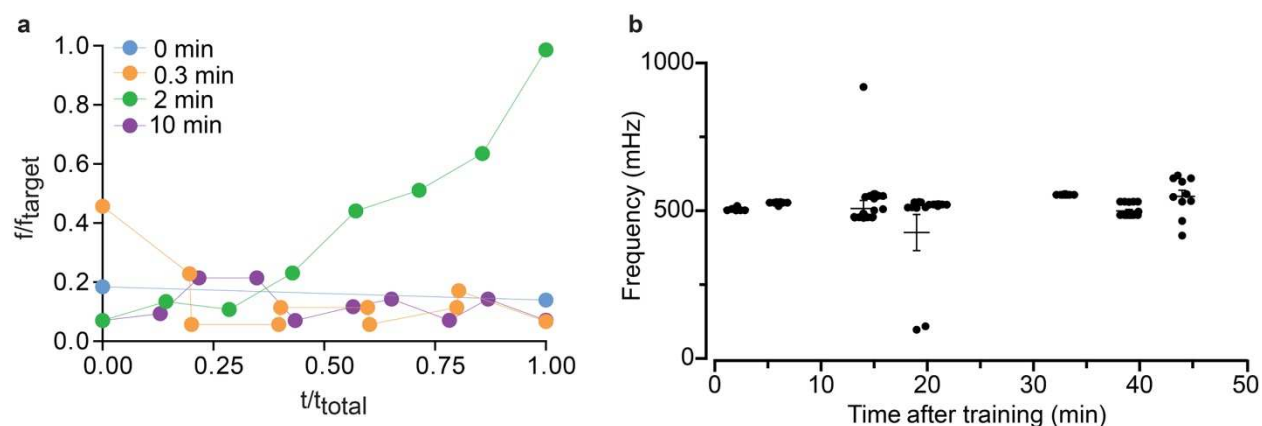


Figure 5-6. Break time is key to effective pacing of cardiomyocytes to continue to beat at target frequency. **a.** Average beating frequencies were plotted as ratios of the beating frequency to the target beating frequency over time for cells from 4 different training experiments with varying break times between optical stimulation periods (no break –blue; 0.3 min break – orange; 2 min break – green; 10 min break – purple). 4 cells were used in the 0 min break experiment (blue), 6 cells in the 0.3 min break experiment (orange), 6 cells in the 2 min break experiment (green), and 8 cells in the 10 min break experiment (purple). Connections between dots do not represent real data and are included as a way to visualize the trend. **b.** Beating frequencies of cells were measured for 45 minutes after training at 500 mHz. Cells effectively maintained stable trained beating frequency for about 45 minutes before starting to diverge back to baseline frequency. Beating frequencies of a total of 124 cells were measured here. Reproduced from Reference 1

5.2.6 Memory effect resulting from scanning based cellular stimulation

The scanning based stimulation approach efficiently stimulated cells to the target beating frequency. This effect was not a one-to-one phase locked cell beat paired with laser pulse and instead was a slow increase to targeted beating frequency. One main result of this mechanism of stimulation was a significant memory effect with cells maintaining the targeted beating frequency for significant periods of time after the light stimulus is removed. (Figure 5-6 a) For memory effect

experiments, calcium imaging limited experiment measurement time frames based on the photobleaching over time. Instead, differential interference contrast (DIC) imaging was used to visualize cellular beating base on change in pixel intensity. Based on this method we identified that cardiomyocytes were able to maintain the targeted beating frequency for as long as 45 minutes without additional stimulation. (Figure 5-6 b)

5.2.7 Conclusions and Outlook

In summary, we have developed a polymer-semiconductor composite material and a combinatorial optical training approach that together can mimic normal physiological signaling inputs by providing multipoint stimulation for target cardiomyocytes. The basis of this training approach is a variable light stimulus intensities achieved via SiNW waveguiding and optical scanning in the XY plane. This method combined with the high density material requires an optical stimulus with an energy density that, although larger than some optogenetic approaches, is four orders of magnitude less than more localized stimulation approaches. We integrated this material and low intensity stimulation to optically train cultured cardiomyocytes to beat at target frequencies. This allows for the training of groups of cardiomyocytes to synchronize and maintain their beating frequency at the target level for long periods of time after the optical stimulus is removed. This has implications for both fundamental multi-cell bioelectric studies as well as photo-responsive cardiac therapeutics in the clinic.

5.3 Experimental

SU-8 mesh preparation for cardiomyocyte culture : SU-8 mesh is adhered to glass bottom petri dishes for cell culture via functionalization of glass surface with APTES¹⁶ and crosslinking SU-8

epoxy groups with APTES functionalized surface.¹⁷ Glass bottom petri dishes (Cellvis, 35 mm Glass bottom dish with 20 mm micro well #1 cover glass #D35-20-1-N) were plasma cleaned for 2 minutes (100 W). Plasma cleaned glass bottom dishes are coated with 1 mL APTES ((3-Aminopropyl)trimethoxysilane Sigma Aldrich Cas # 13822-56-5) for 2 min to functionalize the surface. SU-8 mesh samples are lifted off via the process described for mechanical measurements and transferred to functionalized dishes with NW oriented upwards. Chemical bonding of SU-8 to APTES is achieved by heating dishes to 80°C with a weight of 5.5 g to press SU-8 into glass surface. SU-8 mesh in glass bottom culture dishes are sterilized under UV for 24 hours. SU-8 mesh is coated with fibronectin as previously described and cardiomyocytes are seeded onto the surface of the patterns at a concentration of 500000 cells/dish.

Cell culture protocol : Hearts were excised from P1 neonatal rats into HBSS without Ca or Mg on ice and washed 6 times to eliminate red blood cells. Atria were subsequently removed from each heart and remaining ventricles were minced into 3-4 pieces. Ventricles were incubated on a shaker overnight at 4°C in a 0.05 mg/mL trypsin solution in HBSS. They were then transferred to a 37°C water bath and the activity of the trypsin enzyme was inhibited with a 2 mg/mL soybean trypsin inhibitor solution in HBSS. Hearts were then further digested in 1 mg/mL collagenase type II in L15 medium for 45 min in a 37°C water bath with manual shaking every 5 min. Gentle mechanical trituration of the digested hearts was next performed with a plastic pipette ten times in a tissue culture hood and the resulting cells were passed through a 70 µm filter and incubated at room temperature for 30 min. Cells were then resuspended into DMEM + 10% FBS + 100 U/mL penicillin + 100 µg/mL streptomycin cardiac culture medium and then plated onto 10 cm treated petri dishes in 37°C 5% CO₂ incubator for 2 hours to exclude excess smooth muscle and fibroblasts

from the cardiomyocyte culture. Cardiomyocytes from the supernatant were then plated at a concentration of 500000 cells/dish onto fibronectin coated SU-8-PIN mesh scaffold on glass bottom petri dishes.

Scanning electron microscopy : Cardiomyocytes were cultured onto the SU-8-PIN mesh scaffold coated with fibronectin on a glass coverslip for 48 hours, changing media at the 24 hour timepoint. The culture was subsequently fixed with 4% paraformaldehyde and stained with 1% osmium tetroxide for 1 hour at room temperature. The sample was then critical point dried before being sputter coated with 8 nm of Platinum/Palladium metal. Images were taken on a Carl Zeiss Merlin FEI-SEM.

Immunofluorescence : SU-8-PIN meshes were made with SU-8 precursor solution containing Rhodamine B (Sigma Aldrich Cas# 81-88-9) at about 0.1 mg/mL SU-8. Cardiomyocytes were cultured onto glass bottom petri dishes, or Rhodamine B (Sigma Aldrich Cas #81-88-9) stained SU-8-PIN meshes on a glass bottom petri dish and after three days of culture, were fixed with 4% paraformaldehyde for 10 minutes, permeablized with 0.2% Triton-x solution for 5 minutes, and blocked for an hour with 3% BSA solution. Samples were then stained with anti-cardiac Troponin I primary antibody (Abcam ab47003) (1/400 in 3% BSA), and anti-connexin 43 primary antibody, clone (Millipore Sigma MAB3067) (1/100 in 3% BSA) overnight at 4°C. Cells were next stained for 1 hr with AlexaFluor 594 goat anti-rabbit IgG secondary antibody (Molecular Probes #A11037) and AlexaFluor 488 goat anti-mouse IgG secondary antibody (Molecular Probes #A1101) in the dark for 1 hr at room temperature. Cells are lastly stained with DAPI (Sigma Aldrich CAS Number

28718-90-3) at room temperature for 5 minutes. Samples were visualized on the Caliber I.D Confocal Scanner microscope. Nanowires were visualized via a reflection channel.

Cell viability assay : Cardiomyocytes cultured on either fibronectin coated glass bottom petri dishes alone or glass bottom petri dishes with SU-8-PIN meshes were stained after 3 days of culture with a LIVE/DEAD cell viability assay kit (ThermoFisher Scientific #L3224) and the numbers of live cells in culture on the mesh or on glass were counted. Cells optically trained on the SP5 confocal system were also stained for viability on either glass or the SU-8-PIN mesh.

Optical training of cardiomyocytes : Cardiomyocytes cultured for 3 or 4 days were trained to beat at a target beating frequency using a Leica SP5 Laser Scanning Confocal Microscope. Cells cultured atop a fibronectin-coated glass bottom petri dish, SU-8 grid, SU-8-PIN mesh, or SU-8-iii mesh were stained with Fluo-4 AM intracellular calcium dye (Fluo-4, AM, cell permeant Thermo Fisher #F14201) at a concentration of 0.1 $\mu\text{g}/\mu\text{l}$ for 20 min at 37°C. Cells were subsequently washed twice in modified Tyrode's buffer (NaCl 132 mM, KCl 4 mM, MgCl₂ 1.2 mM, CaCl₂ 1.8 mM, HEPES 10 mM, glucose 5.5 mM, pH 7.4). Cells were then kept in 3 mL of modified Tyrode's buffer at 37°C incubator on the microscope stage for the duration of the experiments. The Argon laser line used for both recording and stimulation was set to 30% of the maximum power. Pre-stimulation cellular beating frequency was determined and recorded by a 488 nm laser at 5% to monitor Fluo-4 calcium flux prior to stimulation using the 40X objective (NA 1.3). The images were recorded at a size of 512 x 512 pixels with bidirectional scanning at 1,000 Hz and a line average of 2. Cells were then stimulated with a 514 nm laser line set to 3% power by imaging one frame and then setting a determined gap time between the next frame to the proper frequency. For

instance, 700 mHz was achieved by turning the stimulation laser on for 714 ms with a corresponding gap time of 714 ms. During stimulation, the 514 nm laser was rastered at a frequency of 1,000 Hz over the entire frame line by line, thus exposing the laser to the whole field of view. During stimulation, the line average was set to 2 with the bi-directional feature off. The measured power out of the 40X objective of the stimulation laser was 0.615 μ W. The stimulation laser spot size diameter was 500 nm and stimulation durations ranged from 8-20 minutes. After stimulation, a post-stimulation cellular beating frequency was determined and recorded by a 488 nm laser at 5% to monitor Fluo-4 calcium flux. Samples were allowed to rest for 2 minutes and the full pattern of training (pre-stimulation recording, stimulation, and post-stimulation recording) were repeated. 4-8 times per sample to measure changes in beating frequency as a result of each repeated stimulation. For the experiments assessing the effects of break time (0 min, 0.3 min, and 10 min) between stimulation cycles, cardiomyocytes were not stained with Fluo-4 and instead recorded via DIC imaging, as many of the experiments were too long in length to avoid significant Fluo-4 photobleaching.

Analysis of cardiomyocyte beating frequency : For all experiments in which cardiomyocytes were stained with Fluo-4 calcium dye, calcium oscillations were analyzed with a Fast Fourier transform in python according to the protocol outlined by Uhlen in 2004. For all experiments in which cardiomyocyte beating was recorded via bright field imaging, we determined beating frequencies by watching the recorded videos of the beating cells and counting the number of contractions each cell experienced during the duration of the video.

Photocurrent measurements : PIN-SiNWs and iii-SiNWs were synthesized as described above using a gold (Au) nanocluster-catalyzed chemical vapor deposition (CVD) process. Nanowires were then sonicated into modified Tyrode's buffer (NaCl 132 mM, KCl 4 mM, MgCl₂ 1.2 mM, CaCl₂ 1.8 mM, HEPES 10 mM, glucose 5.5 mM, pH 7.4) and the nanowire solution was syringe injected into borosilicate glass pipettes that were pulled using CO₂ laser micropipette puller (Sutter Instruments P-2000). The solution was then lyophilized off and the remaining nanowires remained in clumps on the inside of the pipettes. The pipettes, which had resistances of 2.5 MΩ, were then filled with the modified Tyrode's buffer and mounted onto an electrophysiology setup with an Axopatch 200B amplifier (Molecular Devices). The output voltage signal was digitized at 16-bit resolution by an Innovative Integration SBC-6711-A4D4 data acquisition board. The digital analogue converter (DAC) of the data acquisition board supplied the command voltage to the amplifier. Current recordings were performed in voltage-clamp mode at 0 mV with a 532 nm DPSS laser (UltraLasers) focused onto nanowire clumps positioned ~10-30 μm from the tip of the pipettes, thus minimizing any changes in pipette resistance due to increases in temperature produced by light absorption. This laser beam was modulated with an acousto-optic modulator (NEOS Technologies, Gooch & Housego, PLC) and power adjusted via a series of neutral density filters. Laser pulses between 1 and 20 ms durations and 63.6 and 250 mW powers were used.

Single nanowire stimulation PIN-SiNWs were sonicated for 10 seconds off of the growth substrate into a modified Tyrode's bath solution (NaCl 132 mM, KCl 4 mM, MgCl₂ 1.2 mM, CaCl₂ 1.8 mM, HEPES 10 mM, glucose 5.5 mM, pH 7.4). These wires were then drop casted on top of the cultured cardiomyocytes that were stained with Fluo-4 calcium dye (using aforementioned protocol) and allowed to settle for 20 minutes. Cells were imaged on an upright microscope

(Olympus BX51WI). Cells visually interacting directly with a single nanowire were then chosen to be tested for the generation of action potentials by laser pulses from a 532 nm laser focused through a 20X objective (NA 0.5 Olympus UPlanFL N) onto the cell-nanowire interface. A GFP filter cube was used to read out the Fluo-4 calcium dye before, during, and after the target cell was being illuminated with laser light.

5.4. Bibliography

- 1 Parameswaran, R. *et al.* Optical stimulation of cardiac cells with a polymer-supported silicon nanowire matrix. *Proceedings of the National Academy of Sciences* **116**, 413, doi:10.1073/pnas.1816428115 (2019).
- 2 Lapp, H. *et al.* Frequency-dependent drug screening using optogenetic stimulation of human iPSC-derived cardiomyocytes. *Scientific Reports* **7**, 9629, doi:10.1038/s41598-017-09760-7 (2017).
- 3 Wang, Y. *et al.* Optogenetic Control of Heart Rhythm by Selective Stimulation of Cardiomyocytes Derived from Pnmt+ Cells in Murine Heart. *Scientific Reports* **7**, 40687, doi:10.1038/srep40687 (2017).
- 4 Gentemann, L. *et al.* Modulation of cardiomyocyte activity using pulsed laser irradiated gold nanoparticles. *Biomed Opt Express* **8**, 177-192, doi:10.1364/boe.8.000177 (2017).
- 5 Parameswaran, R. & Tian, B. Rational Design of Semiconductor Nanostructures for Functional Subcellular Interfaces. *Accounts of chemical research* **51**, 1014-1022, doi:10.1021/acs.accounts.7b00555 (2018).
- 6 Parameswaran, R. *et al.* Photoelectrochemical modulation of neuronal activity with free-standing coaxial silicon nanowires. *Nature Nanotechnology* **13**, 260-266, doi:10.1038/s41565-017-0041-7 (2018).
- 7 Jiang, Y. *et al.* Rational design of silicon structures for optically controlled multiscale biointerfaces. *Nature Biomedical Engineering* **2**, 508-521, doi:10.1038/s41551-018-0230-1 (2018).
- 8 Jenkins, M. W. *et al.* Optical pacing of the adult rabbit heart. *Biomed Opt Express* **4**, 1626-1635, doi:10.1364/boe.4.001626 (2013).
- 9 Smith, N. I. *et al.* A femtosecond laser pacemaker for heart muscle cells. *Opt. Express* **16**, 8604-8616, doi:10.1364/OE.16.008604 (2008).
- 10 Jiang, Y. *et al.* Heterogeneous silicon mesostructures for lipid-supported bioelectric interfaces. *Nature Materials* **15**, 1023, doi:10.1038/nmat4673 (2016).
- 11 Shoham, S., O'Connor, D. H., Sarkisov, D. V. & Wang, S. S. H. Rapid neurotransmitter uncaging in spatially defined patterns. *Nature Methods* **2**, 837, doi:10.1038/nmeth793 (2005).
- 12 Carvalho-de-Souza, J. L., Pinto, B. I., Pepperberg, D. R. & Bezanilla, F. Optocapacitive Generation of Action Potentials by Microsecond Laser Pulses of Nanojoule Energy. *Biophysical journal* **114**, 283-288, doi:10.1016/j.bpj.2017.11.018 (2018).

- 13 Mathieson, K. *et al.* Photovoltaic retinal prosthesis with high pixel density. *Nature Photonics* **6**, 391, doi:10.1038/nphoton.2012.104 (2012).
- 14 Ghezzi, D. *et al.* A hybrid bioorganic interface for neuronal photoactivation. *Nature Communications* **2**, 166, doi:10.1038/ncomms1164 (2011).
- 15 Savchenko, A. *et al.* Graphene biointerfaces for optical stimulation of cells. *Science Advances* **4**, eaat0351, doi:10.1126/sciadv.aat0351 (2018).
- 16 Nagendra Kumar Kamisetty, S. P. P., Mitsuru Nonogawa, Kamakshai Charyulu Devarayapalli, Tsutomu Kodaki, Keisuke Makino. Development of an efficient amine-functionalized glass platform by additional silanization treatment with alkylsilane. **386** (2006).
- 17 Ren, Y. *et al.* A Simple and Reliable PDMS and SU-8 Irreversible Bonding Method and Its Application on a Microfluidic-MEA Device for Neuroscience Research. *Micromachines* **6**, doi:10.3390/mi6121465 (2015).

Chapter 6 : Altering cardiac tissue beating frequency through the application of the PIN SiNW SU-8 mesh and scanning stimulation in the z-plane.

Reproduced from Parameswaran R*, Koehler K*, *et al. PNAS* 2018¹

6.1 Introduction

Coordinated cardiac contractile activity and proper heart functioning relies on the establishment and maintenance of the electrical conduction system. Failures in the electrical conduction system of the heart lead to often fatal cardiac conduction disorders such as local delays in mechanical contraction or slowed contractions in the whole system resulting in bradyarrhythmia (slow heart rates). Therapeutics are applied to resynchronize the isolated components or increase the beating frequency of the system. Pacemakers are the standard approach for treating bradyarrhythmia or cardiac resynchronization.² Despite the fact that electronic pacemakers are the standard approach, there are some challenges which new therapeutic developments could address including immunogenic responses resulting in inflammation and infection, the requirement of physical wires, low spatial resolution, accessibility of desired therapeutic location, and biofouling of device surfaces at the tissue interface which can impede device performance or undesired electrochemical reactions. Many promising alternative approaches for therapeutic treatment have been developed.³⁻⁹ Optogenetics has been demonstrated as a successful method for pacing rat cardiac tissue with blue light illumination.⁵ Optical pacing with via infrared laser light has also effectively been implemented to pace adult rabbit hearts.⁴ In another approach graphene biointerfaces were exploited for the increase in zebrafish heart rates.³ Soft flexible solutions have been employed in the form of low modulus implantable based on a sleeve implanted around the heart to support cardiac contractions.¹⁰

Here we implement a silicon polymer composite as an alternative therapeutic approach for optical non-genetic stimulation of tissue interfaces. We applied a flexible polymer-SiNW mesh to the surface of an ex vivo rat heart for stimulation to beat at an increased target frequency. This mesh was easily applied to the surface of the heart in a suture free and adhesive free manner. The mechanical properties of this material provide a significant benefit over the traditional pacemaker and the ability to adhere the device to the wet tissue interface. We apply the previously demonstrated scanning based stimulation method paired with the high density PIN SiNW mesh for photovoltaic cellular stimulation. In this approach we take advantage of contractile motion of the heart to apply z-plane based scanning functionality. This method effectively increased cardiac beating frequency to the targeted laser stimulation frequency.

6.2 Results and Discussion

6.2.1 Water adhesion properties

The materials properties resulting from the high density SiNW SU-8 mesh provide significant water adhesion to the device interface.¹¹⁻¹⁴ This adhesive property is key to determining the tissue device interface as the wet tissue surfaces typically provide significant materials challenges for devices in therapeutic applications. To study this water adhesion, we compared the effects of inversion of SU-8 samples on adhered water droplets. To test this, droplets were added to the SiNW SU-8 mesh surface, SU-8 mesh surface, and 5 μm thick SU-8 sheet with no structure. Then the device was inverted, if the device supported the droplet a larger droplet was added. With the addition of successively larger droplets under the effect of gravity we are able to test the adhesion of the water droplets to the different nanostructured and microstructure surfaces. From these experiments we observe that the SU-8 sheets support a maximum droplet volume of 16 μL .

under inversion compared to the SiNW SU-8 surface which supports a droplet volume of 24 μL . The increase of 8 μL is supported by the integration of the microstructure by photolithographic patterning and the nanostructured SiNW surface.

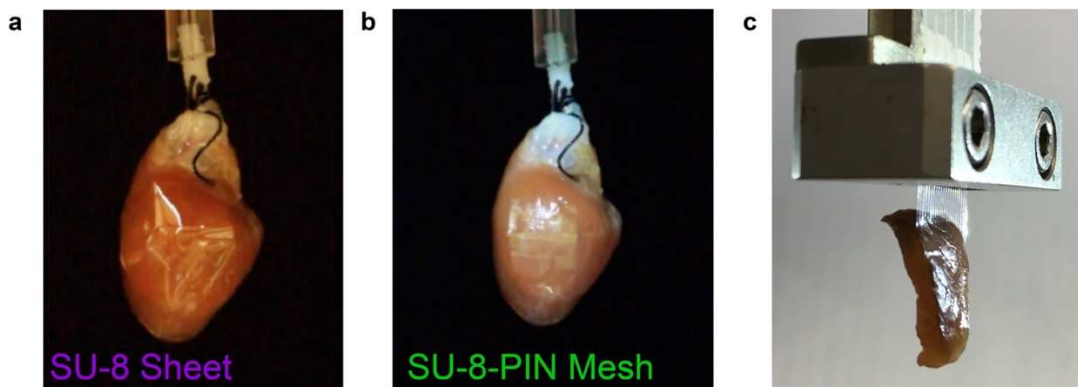


Figure 6-1. Su-8 water adhesion to tissue. a-b. SU-8 sheet (purple) **a** and SU-8/PIN-SiNW mesh (green) **b** wrapped around an adult rat heart via water-assisted adhesion. The SU-8/PIN-SiNW mesh fully conformed and adhered to the heart surface. The SU-8 sheet showed folding, wrinkling, and slippage on heart surface due to reduced water adhesion properties. SU-8 PIN mesh **b** wicked to tissue surface and adhered without sliding or losing contact for the duration of experiments. This adhesion was exclusively based on water adhesion and required no sutures or tissue glue. **c.** Tissue slice supported by SU-8 mesh structure solely *via* water-assisted adhesion. Wet tissue was brought into contact with an SU-8/ mesh and was supported by mesh for at least 20 minutes. Reproduced from Reference 1

6.2.2 Water adhesion properties for suture free and adhesion to tissue interface

The demonstrated water adhesion properties of the mesh wicking the polymer to the wet tissue surface based on capillary action and held it in place for the duration of the study despite mechanical contraction of the heart. (Figure 5-6) This adhesion wicking the polymer mesh to the tissue surface was significant to keep the device in place for the duration of the experiment, as long as 30 minutes, even under the flexing and contraction of the hearts mechanical beating. When wet tissue was brought into contact with the SU-8 structure the device was quickly pulled to the surface of the heart and wrapped around the curvilinear interface. We observed a SiNW SU-8 mesh was capable of supporting a tissue slice for up to twenty minutes exclusively based on the water-assisted adhesion at the tissue interface. Additionally, we compare the potential for tissue adhesion

between the SU-8 SiNW mesh and the SU-8 sheet. In the case of the SU-8 SiNW mesh we observe full contact between the device and heart tissue whereas in the case of the SU-8 sheet the material adhered to the tissue but had significant folds and creases and was not able to be held as firmly in place. By capitalizing on this water interface we are able to accomplish suture free adhesion for the duration of the stimulation experiments.

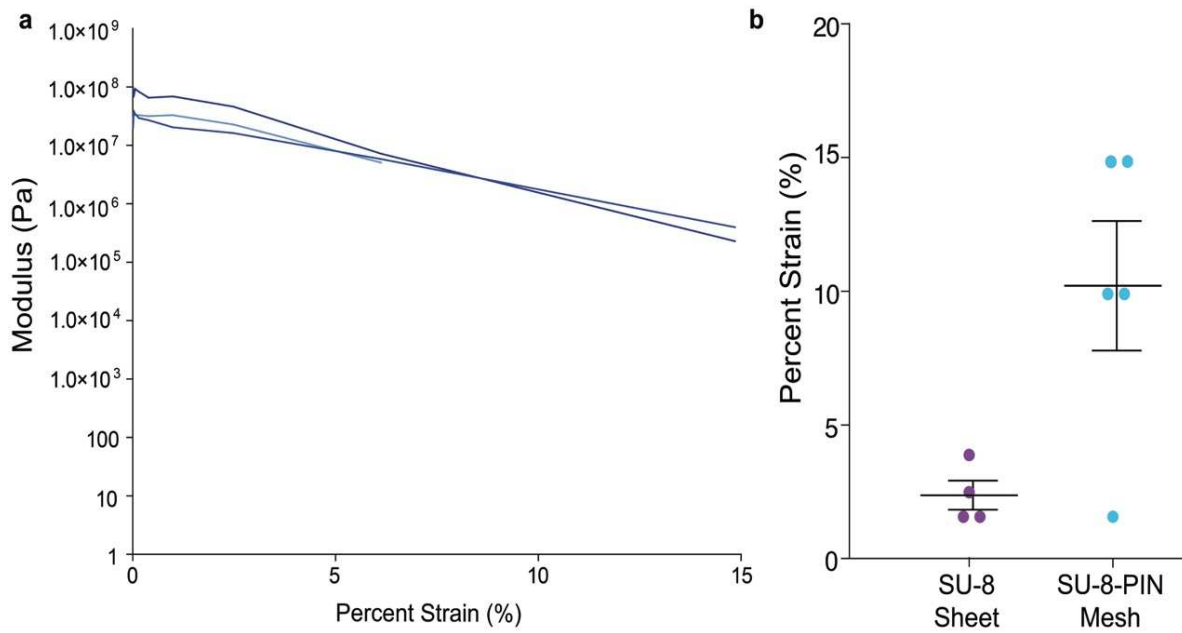


Figure 6-2. Reduction of SU-8 Modulus after fabrication with microstructure and nanostructure. **a.** Graph of DMA modulus vs percent strain was measured to determine the percent strain where failure occurred. **b.** The average values of percent strain resulting in material failure was graphed for SU-8 sheet vs SU-8 PIN Mesh. Reproduced from Reference 1

6.2.3 Soft and flexible properties

The demonstrated mechanical properties, flexibility and reduced elastic modulus, make this device ideal for a tissue device interface. The flexibility of devices is key for reducing the deleterious effects of the inflammation and fouling of the tissue device interface. While this material has reduced modulus and flexibility to bed with the curvature of the heart, the SU-8 polymer skeleton makes the device and freestanding high density SiNW mesh stretched across the

window regions highly durable even under repeated flexing or mechanical contraction. To test the stability under repeated contractions we analyzed DMA data for an oscillation strain cycle with SU-8 structures stretched over increasingly larger distances. We measured the maximum strain percent reached before SU-8 failure occurred in the form of tearing. Under cyclic stress we found that SU-8 samples were able to stretch to 10.21% strain whereas SU-8 sheets ripped at 2.38% strain. From this analysis we verified the stability of the SiNW SU-8 mesh under the repeated mechanical cycling stresses that would be required for tissue applications with significant beating motions such as for cardiac tissue.

6.2.4 Taking advantage of mechanical contraction for z-plane scanning stimulation

For the tissue based stimulation we utilized a similar scanning based laser stimulation method, but for this approach we employed the mechanical contractions of the heart to change the z-plane of the device surface as the device twisted and bent with each beat of the heart. Previously the scanning based stimulation was demonstrated in the x-y plane via a fast moving scanning laser. In this method the sample plane is constantly altered based on the beating motion of the hearts. This variation in concert with the waveguiding effects of the high density SiNW mesh produce the variable stimulation intensity and spatial spot distribution mimicking the transient and spatially distributed stimuli cardiomyocytes receive in vivo. Generally, this method was accomplished by (1) measuring the baseline beating frequency of the heart via ECG electrodes (2) measuring the change in frequency during stimulation.¹⁵ Effective stimulation of the heart was accomplished with a 534 nm laser at 19.7 mW, the minimal intensity needed for effective increase in cardiac beating. The laser was focused through a 5x objective onto the SU-8 PIN SiNW – cardiac tissue interface. The laser was pulsed to stimulate at the target frequency using a waveform generator and a duty

cycle of 20%. The baseline beating frequency of the heart and subsequent frequency alterations were monitored via ECG electrodes at the apex and aorta.

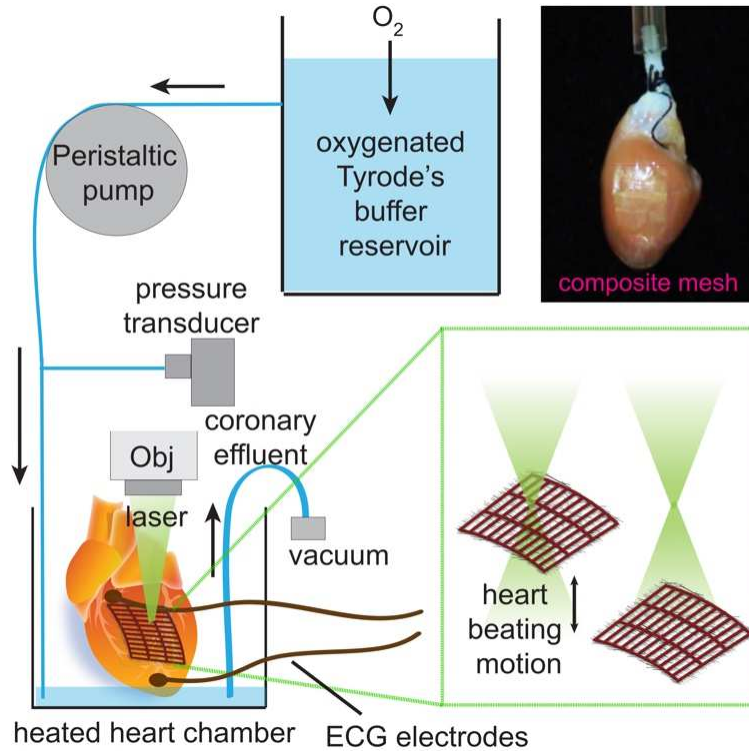


Figure 6-3. Optical training of adult hearts *ex vivo*. Langendorff set up used to assess optical training of adult rat hearts. Oxygenated Tyrode's buffer reservoir was perfused into the aorta of an adult rat heart a chamber maintained at 37°C and the perfusion rate of the buffer was controlled by a peristaltic pump. ECG electrodes were placed on the apex and aorta and both the perfusion pressure, which was transduced to a recordable signal through a transducer, and the ECG recordings were connected to an amplifier that was interfaced with a computer. A 532 nm laser was focused through a 5X objective onto the SU-8-PIN mesh placed onto exposed myocardium on the left ventricle of the heart. (inset) SU-8-PIN on adult rat heart without use of adhesives or sutures. Reproduced from Reference 1

6.2.5 Increased beating frequency of rat hearts via z-plane scanning stimulation

For this tissue system after the initiation of laser pulsing at the target frequency the heart slowly increased beating frequency until it reached the target frequency at which point one-to-one pulsing occurred where one laser pulse coincided with one heartbeat. (Figure 6-4) The slow increase of beating frequency towards the target frequency indicates a similar effect compared to the approach used for isolated cells, but the resulting phase locked target frequency and minimal

memory effect indicated that at the tissue level the method is altered. The general stimulation time for hearts to reach targeted beating frequency was approximately ~4–7 minutes of laser stimulation. Included are stimulation results of a representative experiment for increase in heart beating frequency from the baseline of 0.9 Hz to the targeted frequency of 2 Hz, accomplished in five minutes of laser stimulation. We observe three different paths (Figure 6-4 d) hearts from three different experiments took to reach to targeted frequency. This variable path to target frequency was typical experiments based on this stimulation method, but generally the path was a rise to the targeted frequency.

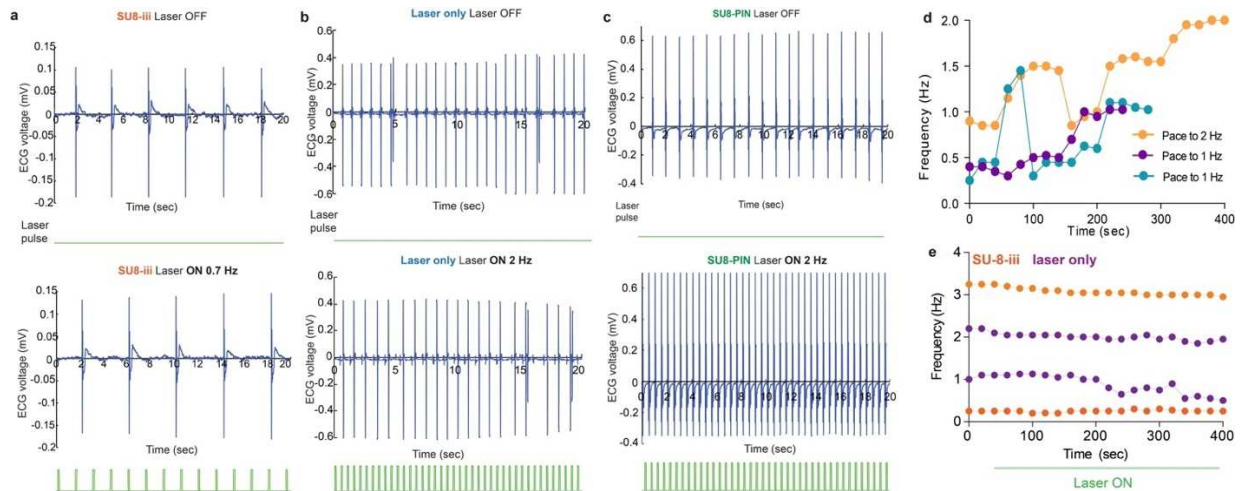


Figure 6-4. PIN SU-8 meshes induce optical training of adult rat hearts *ex vivo* while III SU-8 meshes and light alone do not. **a** Electrocardiogram recordings from an adult heart with an SU-8/III-SiNW mesh beating at 0.3 Hz prior to being exposed to 532 nm laser light pulses (top) and during exposure to 532 nm laser light pulses at 0.65 Hz on the SU-8/PIN-SiNW mesh (bottom). Light pulses are indicated in green under the ECG traces (blue). These are representative traces of N=2 different hearts and N=3 different experiments. **b** Electrocardiogram recordings from an adult heart without any mesh beating at 2 Hz prior to being exposed to 532 nm laser light pulses (top) and during exposure to 532 nm laser light pulses at the tissue surface (bottom). **c** Electrocardiogram recordings of an adult heart beating at 0.9 Hz prior to being exposed to 532 nm laser light pulses (top) and during exposure to 532 nm laser light pulses at 2 Hz on the SU-8-PIN mesh (bottom). Light pulses are indicated in green under the ECG traces (blue). **d**. Beating frequencies of three adult hearts 40 seconds prior to being exposed to 532 nm laser light (first 2 points of each trace) and during exposure to 532 nm laser light (all other points in the traces). Connections between dots do not represent real data and are just a way to visualize the trend. **e**. Beating frequencies of 4 adult hearts with SU-8/III-SiNW meshes (orange) or without any mesh (purple) at times zero and 20 seconds prior to being exposed to 532 nm laser light (first 2 points of each trace) and during exposure to 532 nm laser light (all other points in the traces). SU-8/III-SiNW mesh samples are being trained to 0.7 Hz (lower trace) and 4.5 Hz (upper trace). Light only samples are being paced to 2 Hz (lower trace) and 3 Hz (upper trace). Connections between dots do not represent real data and are just a way to visualize the trend. Reproduced from Reference 1

To verify that this trend of beating frequency increase to target stimulation frequency was exclusively the effect of PIN SiNW mesh, we measured control samples of stimulated hearts with III SU-8 mesh with laser stimulation and hearts with laser stimulation but no mesh. (Figure 6-4 a,b) For the control samples with III SU-8 mesh there is no expected photovoltaic response under laser illumination. For hearts with III SU-8 mesh there was no observed increase to beating frequency over six minutes of stimulation. Similarly, hearts with no mesh did not increase in beating frequency during the six minutes of stimulation. This indicates that the increase in beating frequency results from the photoelectric stimulation of the PIN SiNW mesh under laser illumination as opposed to some photothermal or optical based stimulation.

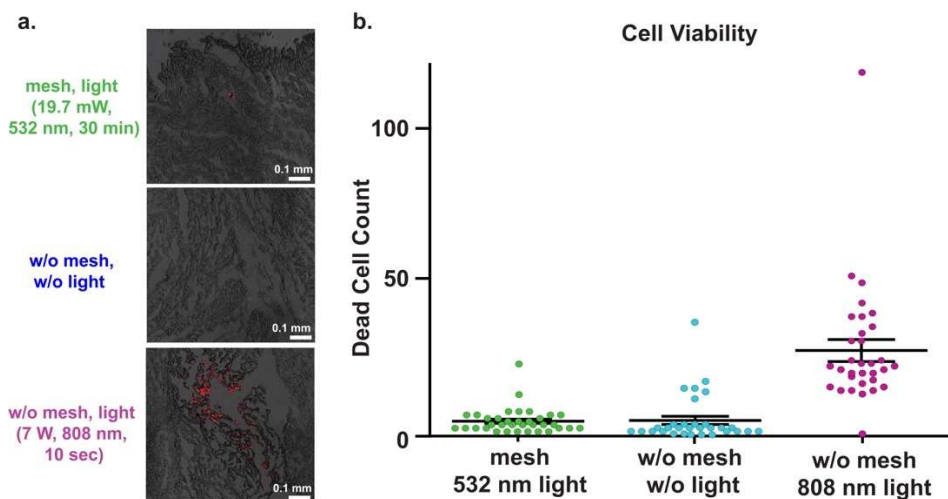


Figure 6-5. PIN SU-8 meshes cause minimal damage from phototoxicity. **a.** This analysis assessed the phototoxicity in hearts that had been exposed to the pulsed light stimulus for 30 min using propidium iodide. Staining with propidium iodide (red) shows dead cells. Dead cell count performed for multiple slices up to a depth of 600 μm . **b.** Phototoxicity of 30 min pulsed 532 nm laser, live control with 30 min no light exposure, and dead control with 10 s pulsed 8W infrared laser. SU-8-PIN mesh with 3.5 Hz pulsed 532 nm light had an average of 35 dead cells per mm^2 as compared to 33 dead cells per mm^2 in a control with no light exposure for 30 minutes. As a positive control for the dye, we exposed a heart to 8 W of 3.5 Hz pulsed infrared laser light for 10 seconds and induced visible tissue death with 62 dead cells per mm^2 in a tissue slice. Reproduced from Reference 1

6.2.6 Minimal cytotoxicity results from laser stimulation

The cytotoxicity of the hearts under laser stimulation was measured using a propidium iodide stain, fixing and sectioning of tissue, and fluorescence imaging.⁴ Hearts were stimulated with for 30 minutes under laser exposure. They were compared with both hearts under perfusion for 30 minutes no light stimulation as a negative control as well as hearts stimulated with an 808 nm laser for 10 s as a positive control with significant tissue death. Laser stimulation for cytotoxicity experiments was performed with 532 nm light pulsed at 3.5 Hz and resulted in average of 4.17 ± 0.64 dead cells over a 1-mm^2 region. For the positive control with no light exposure we observed 4.41 ± 1.26 dead cells over a 1-mm^2 region. The positive control where significant cell death was observed laser pulse of 3.5 Hz at 7W resulting in an average of 26.06 ± 3.4 dead cells over a 1-mm^2 region. These results indicate that optical stimulation of the SU-8-PIN mesh produces very little heat and does not induce significant phototoxicity in adult rat hearts and there is no significant cytotoxic effect of laser stimulation of 523 nm later at 19.7 mW, the conditions employed for altering cardiac beating frequency.

6.2.7 Conclusions and Outlook

From this work, we have developed a method employing a mechanically non-invasive approach to alter the beating frequency of intact adult rat hearts. The success of this material for tissue interfaces is partially dependent on the enhanced mechanical properties resulting from the durable mechanically strong SU-8 backbone paired with the open mesh structure increasing flexibility and reducing modulus. Integration of the high density SiNW mesh converts waveguiding properties to the mesh by polymerizing filaments of SU-8 to support the durable and flexible SiNW mesh stretched across the window region. This property is key for the functionality of the mesh at curvilinear tissue interfaces because the filaments support the mesh during the lift off and transfer

to the heart tissue surface. Additionally, the increased water adhesion of the material provides the potential for water based tissue adhesion to wet curvilinear surfaces in a suture free manner. Finally, in this approach the natural movement of the isolated heart tissue is employed to produce a z-plane scanning based approach to stimulation at variable location with variable light intensity. The next step in implementing this material would entail integrating the cardiac stimulation approach in an *in vivo* method for therapeutic studies.

6.3 Experimental

Ex Vivo Cardiomyocyte Training with SU-8-PIN mesh : Adult rats were heparinized (1000 IU/kg IP) and anesthetized using open-drop exposure of Isoflurane in a bell jar configuration. Hearts were removed, placed in ice cold HBSS buffer, and the aortas were cannulated. Oxygenated HEPES-buffered Tyrode's solution (containing, in mM: NaCl 126, KCl 5.4, Glucose 10, HEPES 10, MgCl₂ 1, CaCl₂ 2, MgSO₄ 1.2, NaH₂PO₄ 0.39; bubbled with 99.5% O₂; pH titrated to 7.3 by 2M NaOH) was perfused through the cannulated aortas. The perfusion was passed through a heating coil and bubble trap (Radnoti), and the hearts were placed in a water-jacketed beaker (Fisher Scientific) to maintain the temperature at 37°C. The perfusion rate was controlled by a peristaltic pump to obtain perfusion pressure of 80–100 mmHg (~10–15 ml/min), which was monitored using a BP-100 probe (iWorx). For ECG recordings, needle electrodes were positioned on the apex and aorta, and connected to a C-ISO-256 preamplifier (iWorx). Both recordings (ECG and perfusion pressure) were amplified using an IA-400D amplifier (iWorx) and interfaced with a PC using DigiData 1550 digitizer with pClamp software (Molecular Devices). To lower the heart rate, the atriums were removed. To allow direct interaction of the SU-8-PIN or SU-8-iii or SU-8 mesh with the cardiomyocytes, a small portion (~20mm²) of the myocardium was exposed by removing the epicardium using a scalpel (#11). SU-8-PIN or SU-8-iii or SU-8

grid meshes were lifted off glass slides as previously described and were deposited onto clean glass slides with a thin film of water with the SiNWs orientation upwards. Glass slides with patterns were brought into light contact with the exposed myocardium. When in light contact, SU-8 structures wrapped around the exposed heart surface and held in place by capillary adhesion. In order to optically train the hearts, we focused a 532 nm laser through a 5X/0.10 Olympus UIS 2 MPlanN objective onto the SU-8 mesh, using a waveform generator to adjust the frequency of the laser pulses at a 20% duty cycle.

Phototoxicity of heart slices : Adult rat hearts were prepared in the same manner as for the optical training experiments. Hearts with removed epicardium in the left ventricle and SU-8-PIN mesh were stimulated for 30 minutes with a 532 nm laser at 19.7 mW power at a frequency of 3.5 Hz and a 20% duty cycle. Controls were prepared in the same way with removed epicardium and were exposed to no laser light for 30 minutes. Positive control hearts for the dead cell dye staining were exposed to 10 s of pulsed infrared laser light at 8 W, at 3.5 Hz and a 20% duty cycle. Following exposure, hearts were stained for dead cells with 30 μ M propidium iodide according to the protocol in Jenkins et al. 2013. Hearts were perfused with PI solution for 20 minutes and were subsequently washed with Tyrode's solution for 40 minutes and placed into ice cold Tyrode's solution. The region of exposure was excised with scissors and embedded in Tissue-Tek O.C.T. (Sakura Finetek from VWR, cat#25608-930) frozen in a cold 2-methylbutane bath and then stored at -80°C. Tissue was cryosectioned in 5 μ m sections collected every 100 μ m. Sections were visualized via Leica SP8 confocal microscope with 10x objective. Dead cell count was analyzed in ImageJ with cell counting application.

Dynamic Mechanical Analysis (DMA) : SU-8-PIN meshes were first lifted off of the glass slides they were fabricated on by HF etching with 48% HF for 20 s at room temperature. The SU-8-PIN mesh were rinsed six times in 3 mL of DI water to remove all HF from solution. They were then transferred to a film tension clamp adapter of Dynamic Mechanical Analyzer (RSA-G2 TA Instruments) and adhered to the tensile testing clamp with Scotch tape. The samples were tested over a range of 0.01% - 15% strain. Modulus data was calculated from the average values of the region of linearity within 0.01% - 15% strain.

6.4 Bibliography

- 1 Parameswaran, R. *et al.* Optical stimulation of cardiac cells with a polymer-supported silicon nanowire matrix. *Proceedings of the National Academy of Sciences* **116**, 413, doi:10.1073/pnas.1816428115 (2019).
- 2 Cingolani, E., Goldhaber, J. I. & Marbán, E. Next-generation pacemakers: from small devices to biological pacemakers. *Nature reviews. Cardiology* **15**, 139-150, doi:10.1038/nrcardio.2017.165 (2018).
- 3 Savchenko, A. *et al.* Graphene biointerfaces for optical stimulation of cells. *Science Advances* **4**, eaat0351, doi:10.1126/sciadv.aat0351 (2018).
- 4 Jenkins, M. W. *et al.* Optical pacing of the adult rabbit heart. *Biomed Opt Express* **4**, 1626-1635, doi:10.1364/boe.4.001626 (2013).
- 5 Nussinovitch, U. & Gepstein, L. Optogenetics for in vivo cardiac pacing and resynchronization therapies. *Nature Biotechnology* **33**, 750, doi:10.1038/nbt.3268 (2015).
- 6 Camci-Unal, G., Annabi, N., Dokmeci, M. R., Liao, R. & Khademhosseini, A. Hydrogels for cardiac tissue engineering. *Npg Asia Materials* **6**, e99, doi:10.1038/am.2014.19 (2014).
- 7 Mawad, D. *et al.* A conducting polymer with enhanced electronic stability applied in cardiac models. *Science Advances* **2**, e1601007, doi:10.1126/sciadv.1601007 (2016).
- 8 Viventi, J. *et al.* A Conformal, Bio-Interfaced Class of Silicon Electronics for Mapping Cardiac Electrophysiology. *Science Translational Medicine* **2**, 24ra22, doi:10.1126/scitranslmed.3000738 (2010).
- 9 Feiner, R. *et al.* Engineered hybrid cardiac patches with multifunctional electronics for online monitoring and regulation of tissue function. *Nature Materials* **15**, 679, doi:10.1038/nmat4590 (2016).
- 10 Roche, E. T. *et al.* Soft robotic sleeve supports heart function. *Science Translational Medicine* **9**, eaaf3925, doi:10.1126/scitranslmed.aaf3925 (2017).
- 11 Teisala, H. *et al.* Nanostructures Increase Water Droplet Adhesion on Hierarchically Rough Superhydrophobic Surfaces. *Langmuir* **28**, 3138-3145, doi:10.1021/la203155d (2012).

- 12 Martinelli, A. *et al.* Wet Adhesion of Buckypaper Produced from Oxidized Multiwalled Carbon Nanotubes on Soft Animal Tissue. *ACS Applied Materials & Interfaces* **5**, 4340-4349, doi:10.1021/am400543s (2013).
- 13 Tang, X. *et al.* Mechano-regulated surface for manipulating liquid droplets. *Nature Communications* **8**, 14831, doi:10.1038/ncomms14831 (2017).
- 14 Pan, Z., Cheng, F. & Zhao, B. Bio-Inspired Polymeric Structures with Special Wettability and Their Applications: An Overview. *Polymers* **9**, doi:10.3390/polym9120725 (2017).
- 15 Rotenberg, M. Y., Gabay, H., Etzion, Y. & Cohen, S. Feasibility of Leadless Cardiac Pacing Using Injectable Magnetic Microparticles. *Scientific Reports* **6**, 24635, doi:10.1038/srep24635 (2016).

Chapter 7 : Porous SiNW – Carbon scaffolds for modulated water adhesion

7.1 Introduction

Recent developments in nanomaterial research have demonstrated potential for controlling and tailoring the solid-water interface for increasing sustainability in wide range of applications from self-cleaning surfaces^{1,2}, antifouling especially in marine conditions^{3,4}, antimicrobial⁵⁻⁷, anti-icing or freezing delay⁸⁻¹⁰, drag reduction at the solid-water interface^{11,12}, and water conservation^{13,14} through droplet collection or microdroplet transport. Integrating active materials with these controllable water interfaces can provide unique approaches to clean solar energy. Previously nanostructured carbon monoliths with high solar absorption efficiency has been used to drive steam generation. CVD synthesis was employed to synthesized nitrogen doped graphene monoliths with a porous structure. The plasmonic heating of the structured drives light to heat conversion resulting in rapid water evaporation.¹⁵ The large surface area due to the nanostructured surface provides significant light absorption for dramatic temperature change. The low density nanostructured allowed for low density samples to float on the water surface and the porous channels provided routes for the generated steam. Evaporation rates under illumination demonstrates significant temperature increase and generates bubbles at the hydrophobic water – device interface. Taking advantage of the solar absorption, localized heat confinement, and capillary water action provides significant harvesting of solar illumination and effective light absorption and steam generation. This previous research demonstrates how modulated water interfaces can provide significant advances into self-cleaning surfaces, anti-icing surfaces, green energy generation, and antimicrobial properties. Here we demonstrate the synthesis of a porous nanostructured monolith of SiNW backbone - carbon shell with switching between hydrophilic and hydrophobic regimes based on chemical composition and nanostructure. This material has

significant photothermal response and extreme softness compared to traditional silicon. The integration of these properties in one material make it a promising candidate for the application of solar absorbers for steam generation or anti-icing applications.

Many of these novel approaches have turned to biomimetic surfaces with nanostructures derived from natural structures such as the lotus leaf, rose petal, and butterfly wing.¹⁶ This material provides extraordinary material water interactions including significant superhydrophobic properties that are stable under droplet impact pressure, fluid immersion, and compression. This biomimetic structure is more closely patterned off of the *Salvinia molesta* fern leaves compared to the more common rose petal or lotus leaf structures. The unique property of the *Salvinia molesta* is the long term stability of air retention submerged under water.¹⁷ This provides for a hydrophobic leaf surface as well as protection from flooding. When the plant is subjected to floods a stable pocket of air is trapped to protect, insulate, and provide respiration for the plant until the leaves surface again. This property results from the integration of a hierarchal structure with hydrophobic and hydrophilic regimes. The surface of the fern leaves are covered in a micro and nanoscale pattern with hairs shaped in an egg beater structure with a crown like structure on the surface.^{18,19} All parts of the hair are coated in waxy crystals except for the apex structure. The wax crystals on the hairs have a low surface energy and a high degree of roughness on the nanoscale which confer hydrophobicity from both chemistry and topography. At the apex there is a smooth cluster of dead cells resulting in hydrophilicity at due to both chemistry and topography. The hydrophilic tips of the hairs anchor the water droplets and stabilize the water material interface for long term submersion. The key components of this unique interface are hydrophobicity, microscale structure and millimeter hairs, nanoscale structures with ridges or waxes, combination of micro and nanocavities, elasticity of the structure.

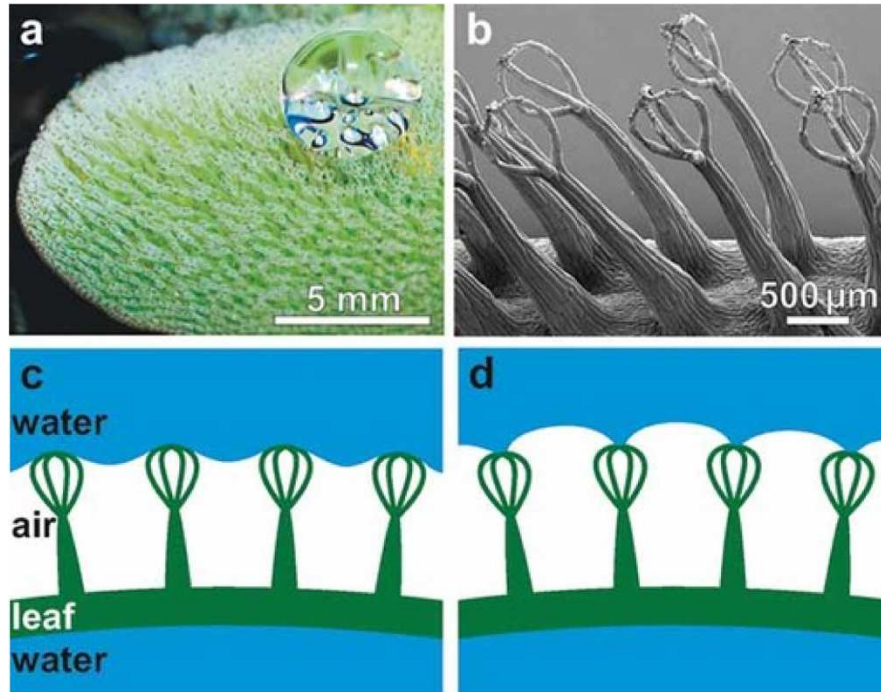


Figure 7-1. *Salvinia Molesta* fern produces a stable air - water interface. **a** Image of the top side of the fern provides detailed information about the morphology about the surface densely covered with hairs. The water droplet on the surface is spherical indicating the highly superhydrophobic quality at this surface. **b.** SEM image reveals a closer look at the hairs with the nanoscale egg beater structure that is key to the stabilized submerged interfaces. **c.** The schematic of the trapped air-water interface formed when the leaf is submerged highlights the hydrophobic repulsion of the material by pinning water at the hydrophilic tips on the top of the hairs, and **d** additionally stabilizes said interface. Reproduced from reference 20.

We have developed a 3-D silicon nanowire – carbon shell foam with tunable water interaction and active photothermal properties. The controllable solid-water interface ranging from hydrophilic to superhydrophobic; with both high water adhesion and high water repellency. (Figure 7-2) This foam is a light weight, soft, flexible silicon scaffold with a hierarchal nanostructured surface that results in drastically different solid-water interfaces. Additionally, the strong solar absorption of the material extends applications especially in the realm of anti-icing materials due to the active photothermal properties capable of melting ice upon ambient light exposure. This foam, with a wide range of water-surface interactions, has the potential to provide a deeper understanding of the fundamental properties that drive water interactions at nanoscale

surfaces as well as meet demands for applications requiring sustainability for energy and environmental applications.

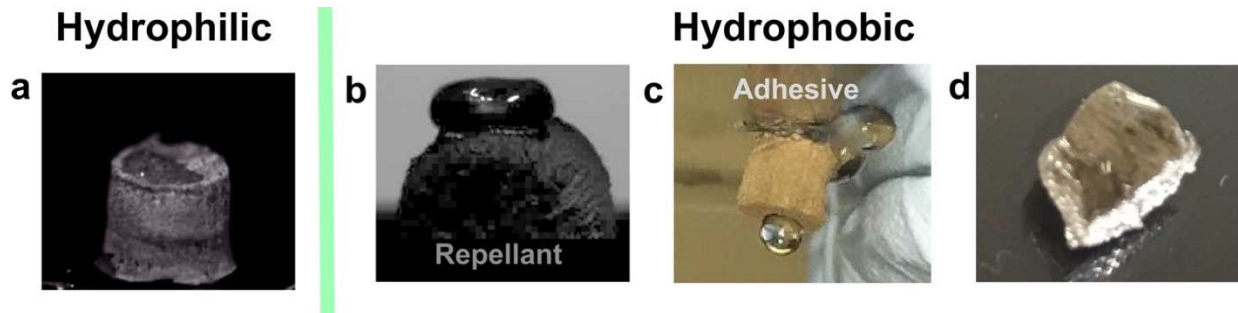


Figure 7-2. Breakdown of the varied air-water interfaces that result from minimal changes in SiNW scaffold synthetic procedure. a Image of the hydrophilic SiNW scaffold. A droplet on the surface of the scaffold can be seen to wick into the material. The contact angle cannot be measured because water wicks completely into the material. **b-d** In the second hydrophobic regime there are two main functionalities. **b.** In the first hydrophobic state the material has significant curvature and droplets do not adhere. Contact angle cannot be measured because the sliding angle is so low. This still was acquired from the dropping of a water droplet on the surface and flattening out before sliding off the surface. **c.** In the second regime, a high degree of droplet adhesion occurs. Droplets adhere to the surface and can be supported even in inversion. **d** In the final hydrophobic state, when the material is fully submerged in water a mirror like interface forms indicating a significant trapped air-water interface that is stable over a minimum of 2 hr windows.

7.2 Results and Discussion

7.2.1 Fabrication

This macro porous scaffold was fabricated with a backbone of 200 nm n-type SiNWs with a carbonized shell binding the structure together. The distribution of nanowire structure and chemical composition across the surface dictate interface variability. The hierarchical nature of the material is determined by the nanostructured SiNWs and the micro structured pores based on freeze patterning. The combination of both chemical variation and micro and nanostructure surfaces provide control over water – material interfaces.

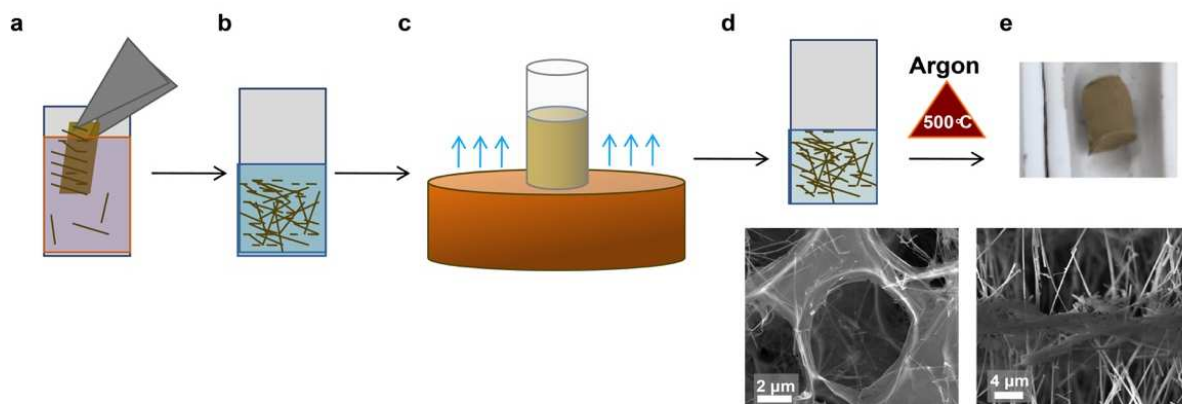


Figure 7-3. SiNW scaffold fabrication process. **a.** SiNWs are sonicated in IPA for 30 seconds to 1 min to remove SiNWs from Wafer substrate. **b.** SiNWs are centrifuged and IPA supernatant is removed. SiNWs are suspended in 1% PVA. **c.** Slurry of SiNWs in PVA is added to an Eppendorf tube fixed to a copper substrate precooled to $-10\text{ }^{\circ}\text{C}$. Unidirectional freeze patterning of slurry occurs for 30 minutes. **d.** After freezing water is removed via lyophilization leaving pores and PVA webbing supporting the structure. SEM image demonstrates PVA webbing. **e.** Samples are heated at $500\text{ }^{\circ}\text{C}$ for 1 hr under Argon to bake off polymer structure leaving behind a carbon shell binding the SiNWs in place.

7.2.1.1 Freeze patterning of silicon nanostructures

The microstructure of the 3D monolith is determined by the unidirectional freeze patterning of the SiNW slurry. 200 nm n-type SiNWs were synthesized via CVD and sonicated into IPA solution. SiNWs are centrifuged and transferred to polyvinyl alcohol (PVA) solution.

Several different methods of freeze casting were explored including variations on ice front directionality, ice front velocity, and solid loading fraction. Altering these properties affects pore size, pore shape, and solid encapsulation. The general theory of ice templating materials is based on segregation of a second phase by a solvent that is solidifying.²¹ This second phase is generally a solid nanoparticle and has been demonstrated with materials ranging from ceramic nanoparticles, metal particles, or polymers. The key considerations of this phase are that it must be able to be dispersed in the solvent. As the ice front moves forward, the second phase is either encapsulated or rejected from the ice crystals. Through this process the second phase is templated by the ice crystal growth. The balance between encapsulation and segregation of the second phase is determined by the competing attractive and repulsive forces at the ice front between the solvent

and the nanoparticles.²² Finally, the solvent is removed through sublimation leaving a porous material based on the absence of solvent crystals.

In the first variation, we explored the directionality of the ice front. (Figure 7-4) In one case the slurry can be submerged in a freezing solution to have ice formation from three different directions. This resulted in spherical pores and a soft material with a low modulus. In the second approach the solution was dipped at a fixed speed into a freezing solution. This resulted in a mainly anisotropic material with some variability depending on speed and freezing temperature. The final approach examined provided the most consistent and unique pore structure. For this approach the unidirectional freezing method was applied to provide anisotropy and structural support. The solution of nanoparticles was applied to a mold fixed to a pre-cooled copper substrate. The ice front moved uni-directionally from the copper substrate to the top of the mold. From this method we produced a vertically aligned porous structure with horizontal interconnections resembling a ladder structure.

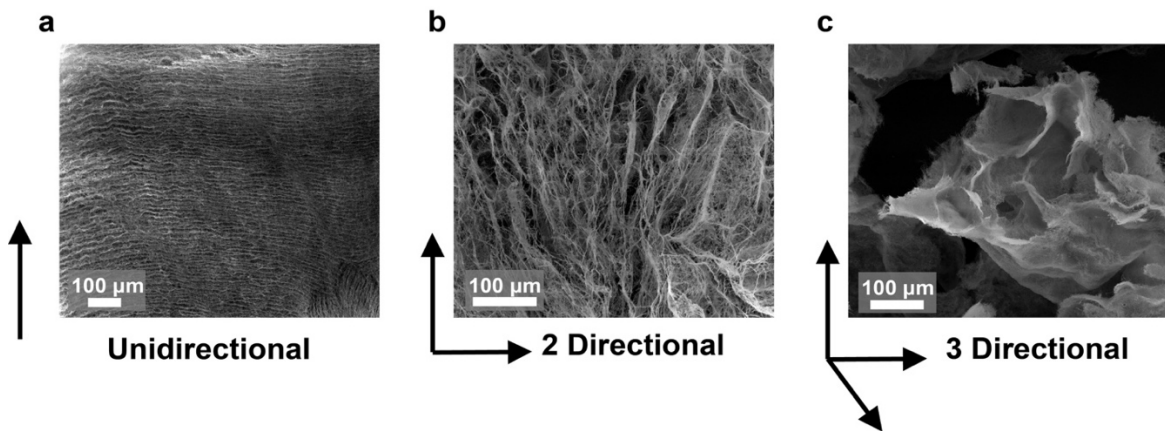


Figure 7-4. Freeze casting test with Unidirectional, 2-Directional, and 3-Directional freezing of scaffolds. **a.** Unidirectional freeze casting results in vertically aligned porous structures. Samples are produced by freezing slurry from the base up on a copper mold. **b.** 2-directional freezing produced wider and more variable vertical pores. Samples are produced by dipping mold with slurry into cold solution so that the temperature gradient was introduced both vertically and horizontally. **c.** 3-directional freezing was accomplished by a fast dipping process into cold solution. In this manner the temperature gradient occurred on all sides producing large round pores.

For the second variable, ice front velocity, we compared several different freezing solutions at different temperatures. The temperature controlled the speed of the ice front during freezing and therefore shift between the regimes of complete exclusion of the second phase, exclusion of the second phase around ice crystals, and encapsulation. One of the biggest challenges in the standardization of the process is consistent temperature control. Variation of just a few degrees can lead to drastic structural changes in the patterned morphology. For this variable we compared the effects of freezing in an ethylene glycol – dry ice mixture of -15 °C, ethanol – dry ice mixture of -72 °C, and a fast freeze in liquid nitrogen at -196 °C. Based on structural analysis of the samples by SEM we chose to work with the ethylene glycol dry ice mixture because it consistently provided clean ice crystals of 40-70 μm and the balance between second phase inclusion and encapsulation resulting in the desired ladder structures. The other temperatures produced ice front velocities that resulted in more encapsulation and inconsistent structures.

Next, we studied the loading ratio of the second phase of nanoparticles and the additive. Both the absolute ratio of both of these in solution as well as the ratio compared to each other impact the resulting structure. The nanoparticle weight percent and morphology direct encapsulation vs exclusion events. When the particle sizes are larger than the critical size the particles tend to be encapsulated by the moving ice front. Alternatively, the various additives can provide complex control over the activity of the crystals and exert significant control over the final pore structure. Additives can change solution viscosity, slow ice front velocity, decrease the surface free energy, or alter anisotropic structure by adsorbing to surfaces. PVA, the additive chosen for this work, is able to direct faceting of the pattern of ice crystals.

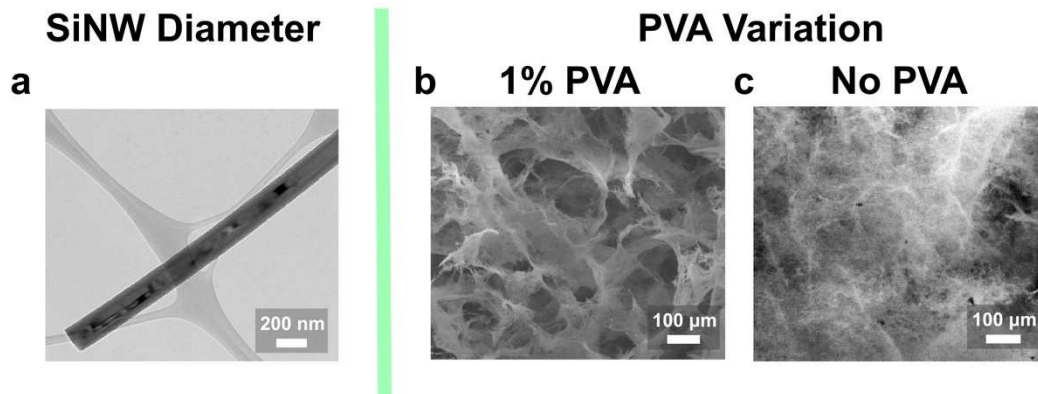


Figure 7-5. Freeze casting of scaffolds is tested with a variety of SiNW diameters, and the density of SiNWs in PVA. **a.** SiNWs are fabricated by CVD with 200 nm diameter SiNWs to produce structures with minimal structural collapse. **b.** 1% PVA and 1% SiNW loading density produced structurally sound pores on the order of 100 μm with minimal collapse after lyophilization. **c.** Scaffolds with higher than 1% PVA or as pictured here no PVA shows significant structural collapse and lack of porous structures.

For the nanoparticle loading ratio we compared morphology, length and diameter, as well as weight percent. First, we identified the appropriate loading ratio in solution by weight. Samples were fabricated with SiNW percent ranging from 0.3% - 1%. Low weight percent of nanostructures resulted in significant to partial structural collapse. From this analysis we identified approximately 1% SiNWs volume percent provided minimal structural collapse and resulted in ordered pores with the desired pore size. We compared wires ranging from 50 nm to 200 nm in diameter with consistent lengths resulting from 30 minute growth times. Samples with nanowires less than 200 nm diameter resulted in structural collapse after lyophilization of about 60% - 30% volume. At 200 nm diameter the structure demonstrated minimal collapse on the range of about 5%. As a final workspace parameter, we studied smooth versus notched SiNWs to identify which morphology resulted in the strongest SiNW interaction. We accomplished the smooth nanostructure through traditional CVD growth. Notched nanostructures were fabricated by modulating n-type and intrinsic type segments. After synthesis the n-type segments were preferentially etched to produce a repeated notch structure in the samples based on wet KOH etching.²³ SEM verified the presence of the notch like structure after etching. We synthesized samples from both morphologies and

found less structural collapse. This indicated that adding notch like structures does not increase structural area overlap between SiNWs compared to that of smooth SiNWs.

Finally, we examined the effect of additives on the resulting structure. The additives alter the solution – nanostructure interface, the ice crystal morphology, and growth velocity. This is accomplished through chemical interactions at these varied surfaces. For this work we varied different PVA concentrations. As an additive, polymeric substances such as PVA, glycerol, gelatin, or sucrose directly impact the viscosity of the slurry resulting in significant variations in the pore size.²⁴ Samples with PVA loading percent between 0% - 10% were examined. With no PVA additives the crystal formation was extremely randomized. No clear pore structure was observed. At high PVA loading samples demonstrated significant volume collapse after lyophilization. This occurred because the majority of the structure was based on hydrophilic PVA instead of the inorganic component. After water removal we observe structural collapse in any case where the SiNW concentration is too low to support the structure formed from freeze patterning. Based on this analysis we observed that 1% PVA is key to the formation of large, organized, anisotropic pore structures. (Figure 7-5) Immediately after lyophilization a webbing of PVA is visible wrapped around the SiNW structure cast by the ice crystals. (Figure 7-3) In this orientation the material is very soft and can be dissolved in water. For this reason we chose to apply a post processing step involving converting the PVA from a hydrophilic web to a carbon shell binding the SiNWs together.

7.2.1.2 Silicon-Carbon Shell Structure

After lyophilization the PVA binding the SiNW structure is easily dissolved in water. To produce a more durable crosslinking of SiNWs, the polymer shell is burned at 500 °C under nitrogen. In these conditions a carbon / silicon shell is formed. After this crosslinking process, the

scaffold changes from super hydrophilic to superhydrophobic with significant increases in durability.

This process was tested with several variations to identify the appropriate mechanical properties and ideal water - material interfaces. We compared as prepared samples with samples heated to 500 °C under oxygen, and samples heated to 500 °C under nitrogen with a relatively oxygen free environment. Samples with no heating process were extremely hydrophilic and the entire network of polymer connecting the sample was able to be dissolved in water. Samples heated under oxygen resulted in highly oxidized SiNW scaffold glued together by an oxidized carbon shell. These samples, exclusively based on the microstructure, were hydrophobic on initial contact with water. Water beaded up on the surface of the material, but through the process of IPA – water solvent exchange we were able to flow water through the scaffold. Once the surface tension of the water on the micro and nanostructure of the scaffold was broken by IPA the hydrophilic nature of the material allowed for water to fully permeate the scaffold. In the final method, there was minimal oxygen during the heating process. This resulted in two separate variations of carbon shell arrangements gluing the resulting scaffold together. The carbon either agglomerated at SiNW junctions or formed a shell around the SiNWs akin to a web. In both instances these variations provided the structural support to hold the scaffold together under stress resulting in a flexible scaffold with varied water interfaces depending on the percent of one structural carbon functionality or another. From these different methods we observed a shift from softest to strongest material between no heating, heating under oxygen, and heating under nitrogen.

We characterized the carbon shell with XPS analysis to discern the variations in chemical composition to understand the extent of the impact of modifying the structure of the carbon shell. SEM was used to characterize the resulting surface modification that are linked to the drastic

alterations in the solid water interface. From SEM analysis we identified a pore size between 40 – 70 μm with larger pores at the external regions of the sample where there was contact with the mold. This is likely because contact with the mold resulted in a different temperature gradient compared to the center portion of the scaffold with uniform surroundings. The result of this temperature gradient was a variation in pore sizes. Additionally, from SEM and 3D laser scanning confocal microscopy (Figure 7-6) we observed that the pyrolysis process leaves significant carbon residue on the surface specifically at critical nanostructure junctures. (Figure 7-6 b) The variation between the webbed carbon shell and the carbon spheres is likely the source of both structural and chemical variation dictating modulated water interfaces.

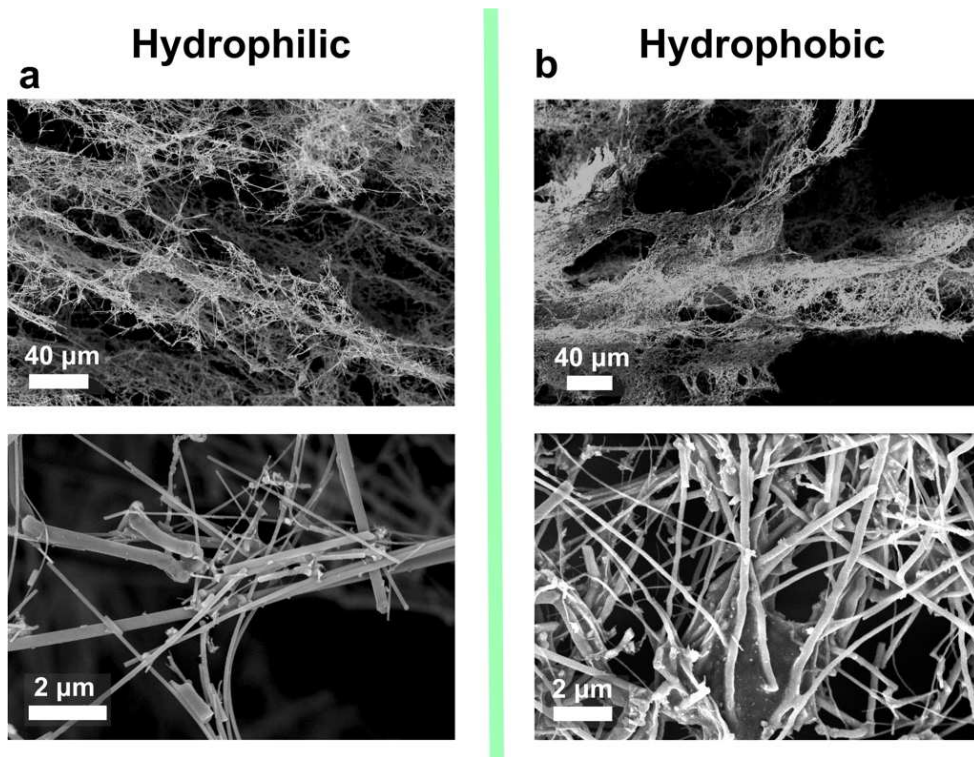


Figure 7-6. SEM Visualizing the variation between hydrophilic and hydrophobic samples. **a.** Hydrophilic scaffold shows porous structure with minimal webbing of carbon shell between the SiNWs. This nanoscale chemical variation is reminiscent of the factors controlling *Salvinia Molesta* fern. **b.** Hydrophobic scaffolds produce the same general pore structures as a, but the main source of water interfaces results from chemical variation. A significantly higher portion of carbon is present on the surface of the SiNWs. Specifically this chemical variation occurs on the nanoscale. The carbon webbing between the SiNWs is rough and reminiscent of the rough structure pinning water to the surface of the *Salvinia Molesta* fern.

7.2.2 Hierarchal porous nanostructured interfaces result in a range of water interactions

The samples heated under nitrogen provided a wide range of surface structures that produced significant changes in the material – water interfaces. This shifted samples from extremely hydrophilic to superhydrophobic repellent or superhydrophobic adhesive based on the hierarchal micro and nanoscale surface topography. We can draw from examples readily found in nature to understand how these hierarchal changes can produce novel functionality at water surfaces. The most interesting variation was produced by the samples which were superhydrophobic with high water adhesion. In addition to these high water adhesion properties we discovered the ability to trap significant volumes of air within the sample for extended periods of time. This effect is reminiscent of the unique properties of the *Salvinia Molesta* leaves. This fern varies from the traditional water adhesion approach of the rose petals in that it integrates structural hierarchy with both hydrophilic and hydrophobic properties. From this structure ferns are able to float on the water surface and are also able to trap air when submerged providing protection from flooding. This significant variability in water interfaces results from very small alterations in the fabrication process resulting in nanoscale structural variations. It provides insight into fundamental studies of water interfaces based on the competing effects of surface topography and chemical composition and also provides a new material with excellent control over water interactions. The ease of surface functionalization, together with deformable and light weight properties of the silicon scaffold, allows for modulated interactions with other soft materials (e.g., from water repellent to adhesive surfaces). We characterize these interfaces by static water contact angles via DSA, droplet impact studies, droplet inversion studies, and 3D laser scanning confocal microscopy.

7.2.2.1 Superhydrophobic state with low water adhesion

The first state that resulted from this sample synthesis is a superhydrophobic state with low adhesion to water similar to the lotus leaf. In this state water is repelled from the surface such that the droplet roll off angle is minimal. This state results from variation in the hierarchical structure preventing droplet pinning to the surface. The superhydrophobic nature of this surface results from a combination of both chemical composition and nano and microscale roughness. The nanoscale roughness is consistent between samples due to the SiNW structure. For droplet repulsion, the curvature breaks droplet contact with the surface and injects air beneath the droplet preventing adhesion.²⁵

Previously, curvature has been demonstrated to provide the variation required to switch samples from roll off to pinned states based on a flexible PDMS pillar array.²⁶ From this analysis at high curvature the contact angle was shown to be 160 °C and a sliding angle of less than 5 °C similar to a Cassie state. In the flat sample state, the measured contact angle was 150 °C with high adhesion as in the Wenzel state. The adhesive force between the wetted region and the solid is mainly due to van der Waals forces. At a high radius of curvature, the area fraction of projected wet area decreases while the roughness factor increases. Curvature increases the distance between adjacent contact posts and moves them out of the sample plane injecting air into the structure propelling the transition between pinned to roll off.

In a similar vein, the curvature of the surface on the sidewalls resulting from the mold resulted in superhydrophobic roll-off states. When samples were fabricated with sufficiently large molds with reduced radius of curvature the pinned state was achievable. Likewise, curved samples that were gently flattened transitioned from roll-off to the pinned state. For flat surfaces, depending on the stability of the freezing process and the slurry uniformity surfaces can transition from

macroscopically flat to macroscopically curved. This transition does alter the nanoscale topography. The macroscopic curvature results from a small gradient at the ice front during the freeze casting process. Samples with macroscale curvature across the flat surfaces produced the same effect as curved side wall surfaces.

We measured the superhydrophobic nature of this state using DSA measurements. No value was calculated as droplets were not stable on the surface for long enough to take a measurement. This resulted from the extremely superhydrophobic nature and extremely low contact angles. We measured the superhydrophobic stability of the samples by adding foam monoliths to a water bath for 20 minutes and repeatedly submerged samples. When samples were submerged under water the mirror like surface indicated significant amounts of air were trapped in the foam. To test the stability of this trapped air samples were cyclically compressed. Under compression no air was freed from the sample indicating that the air trapped was highly stable as was the superhydrophobicity.

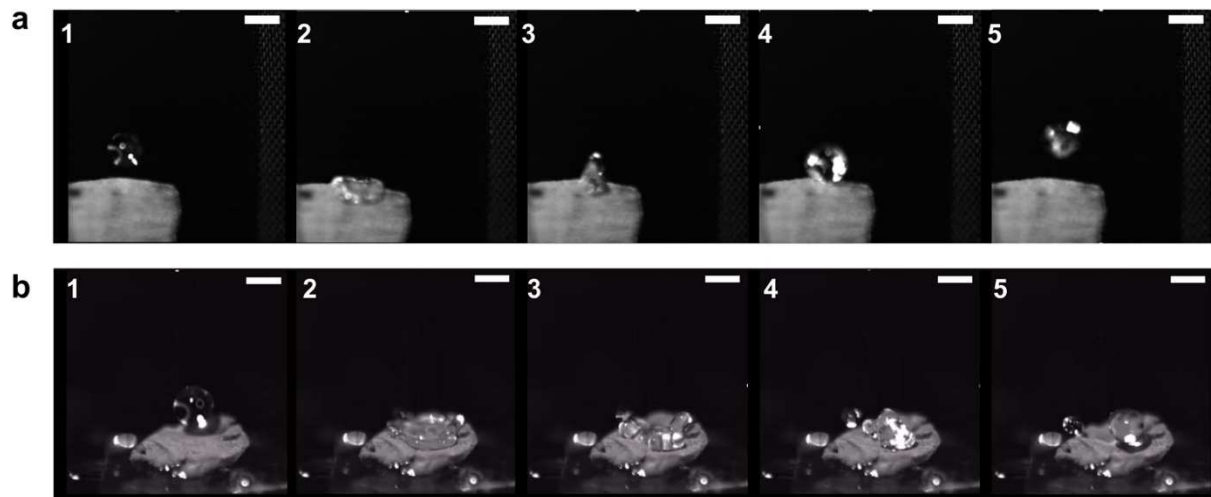


Figure 7-7. Droplet impact studies of flexible and crushed scaffolds. a. Hydrophobic repellent scaffolds flex under droplet impact and show complete recovery. The cooperative effect of super hydrophobicity and flexibility result in droplet ejection characteristics (3) and droplet bouncing height (5) of 1.25 mm. **b.** Hydrophobic crushed scaffolds have the same nanostructure and chemical composition but have no flexibility. Under droplet impact droplet spreading (2,3) occurs before droplet break up (3,4). The maximum bouncing height (5) is 0.25 mm.

In the superhydrophobic water repellent state of our silicon-based material, mimicking the nanostructured lotus leaf surface, water bounces and slides off the surface with no pinning. The highly flexible nature of the material contributes to ejection of water droplets from the surface upon impact. We used droplet impact studies to characterize the effect of the soft flexible material properties on droplet spreading, recoiling, bouncing, and ejection of water droplets upon impact. The bouncing height for crushed scaffold is drastically decreased compared to the flexible scaffold that is repellent.²⁷⁻³⁰ This demonstrates the flexibility of the scaffold was observed with droplet impact studies. (Figure 7-7) As the weight of the droplet impact the surface of the monolith the sample compresses and shows 100% recovery. From this study we found that the flexible properties of the scaffold provided significant contributions to droplet interaction with the surface. Under water repellent conditions, the flexibility of the structure provides added momentum for ejection of droplet from the surface upon impact. The flexible vs crushed scaffold produced droplet bouncing heights of 1.25 mm and 0.25 mm respectively.

7.2.2.2 Superhydrophobic state with high water adhesion

Small changes in the surface orientation can result in a superhydrophobic adhesive state in which the water droplet is pinned to the surface nanostructure, but trapped air prevents water from wicking into the foam. The superhydrophobic state with high water adhesion results from samples with similar composition to the roll-off states with the main difference being the significantly flatter microstructure. The structure of the water - material interface produced in this state mimics that of the unique *Salvinia molesta* fern leaves. The nanowire bundles cluster together with rough carbon tips at the pinnacle in a structure reminiscent of the eggbeater structures. In the fern, these bundles are coated with a smooth waxy structure providing both structural and chemical hydrophobicity. At the top of the eggbeater structure there is a cluster of dead cells which are

hydrophilic. This pins the water droplet to specific points on the surface stabilizing the interface. In our samples, the density of pinned regions direct water droplet adhesion. This results from the rough bundles at the top of nanowire clusters. The superhydrophobic nature was measured using DSA analysis. The average contact angle for droplets on this surface is 151.15° . This is slightly reduced from the actual value due to curvature at the edges of the monolith blocking the calculation of the true contact angle.

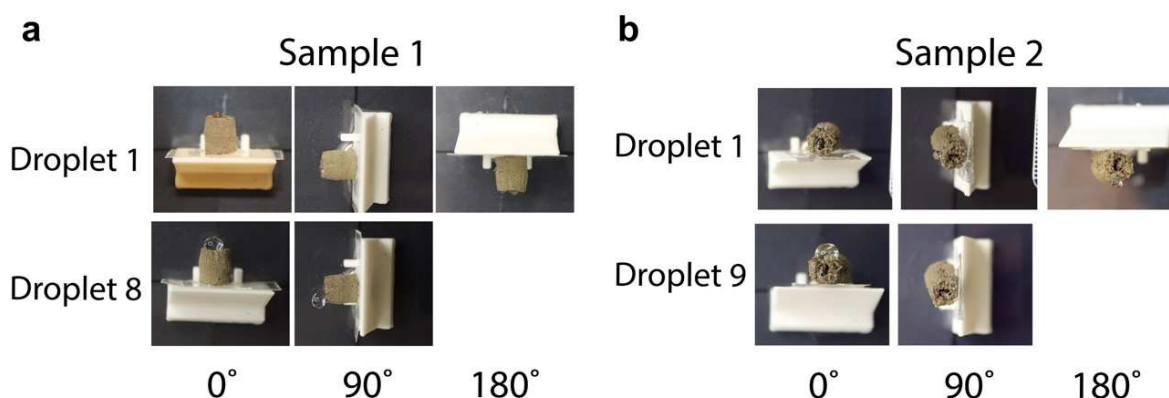


Figure 7-8. Droplet inversion studies demonstrate adhesion at interface is supports droplets against gravity. a. In the first sample, droplet detachment occurs on the 8th droplet at 180° . **b.** In the second sample, droplet detachment only occurs after the 9th droplet at 190° .

We used inversion studies to determine the roll off angle and found that the adhesion was significant enough to prevent droplet detachment even in inverted states, and calculated the maximum water droplet weight supported in the inverted state.³¹⁻³³ In this state, microdroplets up to large water droplets can be inverted completely without detaching from the surface. This material can support a significant weight of water in the inverted state before the force of gravity over comes the significant liquid solid adhesive force. Tests submerging samples in this state into water behaved in the same manner as the repulsive samples. Interestingly, samples with adhesive ends and repulsive sidewalls were able to self-orient on water surfaces. Despite the significant height of the monoliths, samples would repeatedly right themselves to float on the sample edge with high water adhesion. The ability to promote adhesion was employed for adhesion to surfaces

based on a water droplet loaded on the end of the sample. This property could be employed as a method of water based adhesion or wet tissue adhesion.

Additionally, droplet impact videos (Figure 7-7) demonstrate both superhydrophobic and water adhesive properties of the top of the scaffold. For water repellent samples, the flexibility of the scaffold acted in a cooperative nature with the water repulsion properties and assisted in droplet ejection from the sample surface. Samples with significant pinning have the same flexible nature, but for these structures the adhesion to the surface captures the impacting droplet.

7.2.2.3 Hydrophilic surfaces

In the final state, a minor modification in both surface structure and surface chemical composition makes the material extremely hydrophilic. This variation likely results from some oxygen leakage into the reaction chamber during heating under nitrogen. The presence of minimal oxygen results in more hydrophilic carbon surfaces. Additionally, the carbon binder holding the SiNW structure together changes from conglomerates at the nanowire bundles but instead is webbed around the SiNWs. The foam in this state is able to rapidly wick water into the pores. As observed by the addition of foams to water solutions not only does the material show wetting, water quickly wicks into the foam scaffold. There is no contact angle for these samples as the water droplet moves into the sample too quickly to get a measurement. We observed droplet impact to understand the water interface. For hydrophilic samples the water droplets impact the sample, pin to the surface, and bounce and spread on the surface until they are subsequently absorbed into the scaffold. From this analysis we demonstrate the potential for producing a range of material – water interfaces from minor changes in the synthetic process.

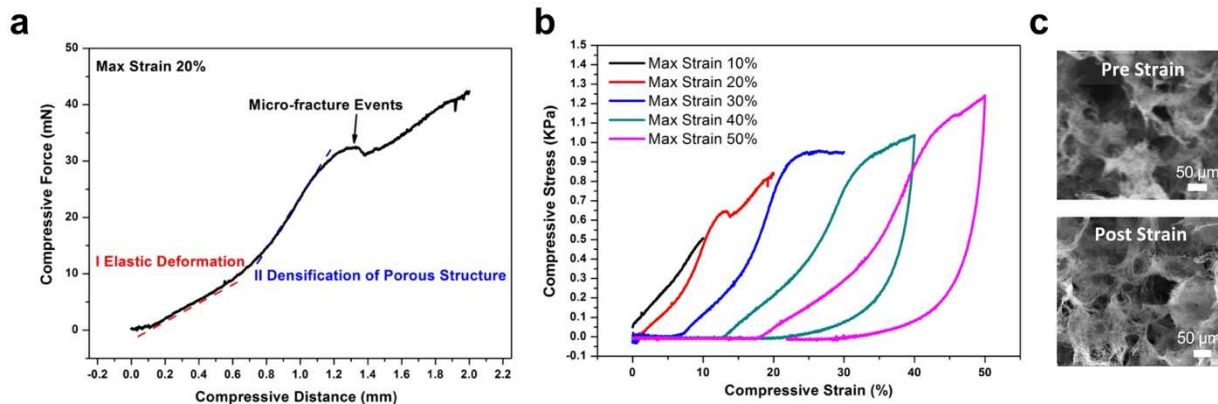


Figure 7-9. Scaffold compression demonstrates flexibility and recovery. **a.** The graph of compression testing correlates force and distance to identify the region of elastic deformation occurring below 10% strain. Around 10% strain permanent fracture in the structure begins to show based on the nonlinear slope. **b.** Cyclic compression demonstrates the potential recovery of the scaffold upon repeated significant compressions. Even after 50% compression (pink) partial recovery of the scaffold occurs. **c.** SEM imaging of the scaffold before and after compression at 50% strain demonstrate the potential for stability of the pore structure even under significant compression.

7.2.3 Materials properties soft and flexible

This silicon scaffold is highly flexible and can undergo significant strain before deforming. This makes the scaffold ideally suited for interfacing with soft materials such as polymers or tissues. We measured the scaffold flexibility through compression testing. Compression testing demonstrated cyclic compression and partial recovery of scaffold up to 50% strain. The compression test was run at 10% strain per minute with 5 cycles of 10%, 20%, 30%, 40%, and 50% strain. Each cycle showed partial recovery behavior with the highest strain providing the highest percent of permanent deformation. With compression around 10% the samples are able to show repeated cycles of strain with no permanent deformation.

The modulus of the silicon scaffold puts this material in the soft range much closer to tissue mechanical properties than typically fabricated silicon structures. This provides a unique material for interfacing with soft tissues or polymers for photothermal stimulation or water interfaces at the interface. Additionally, the mechanical properties of the scaffold provide unique water solid interfaces for systems with impacting droplets.

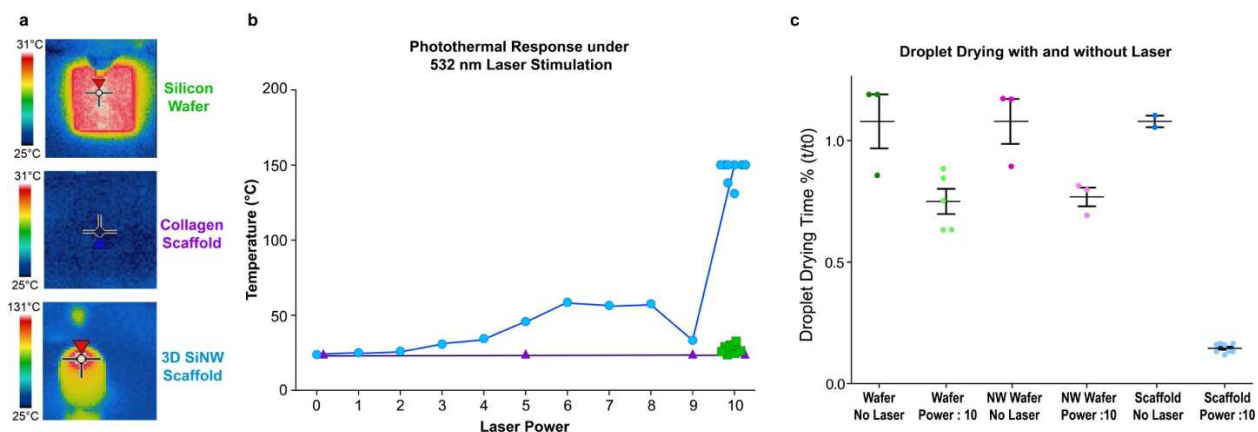


Figure 7-10. Photothermal scaffold response and potential for water evaporation. a. IR camera images of the silicon wafer, collagen scaffold, and 3D SiNW scaffold under 532 nm laser illumination. Images demonstrate significant temperature increase for SiNW-Carbon scaffold with the largest temperature variability directly at the laser spot with a temperature gradient down the scaffold structure. **b.** Photothermal response of material under laser illumination. Silicon wafers and collagen scaffolds show no appreciable temperature variation across the laser scale. The Si scaffold increases with increased laser power. IR camera maximum temperature is 150°C therefore it is likely that the temperature at 10 p laser power is likely significantly higher than 150°C. **c.** Based on the measured photothermal response, the normalized droplet drying time was measured for a droplet of water added to the material surface. Si wafer and SiNW wafers show about a 20% reduction in droplet drying time under laser illumination while the Silicon – carbon scaffold produces almost 90% reduction in droplet drying time.

7.2.4 Photothermal properties under illumination

We also investigated the potential for water purification, deicing applications, or steam generation by measuring the drastically accelerated water evaporation at the foam-water interface.³⁴⁻³⁷ We examined the photothermal activity of the material by measuring temperature increase under laser illumination with an FLIR camera. We observed significant temperature increase under 532 nm laser illumination. We observed rapidly accelerated droplet evaporation from the surface of the foam monolith. This evaporation is driven by localized heating in the monolith scaffold and the capillary interaction at the water material interface. This accelerated heating was not observed for polymer scaffolds without high density nanowire loading. The 3D porous foam monolith photothermal potential was measured via illumination under 532 nm laser between 0% - 10% power. The change in temperature was measured with FLIR camera with a maximum temperature value of 150 °C. Samples increased in temperature between 0% - 10%

power and reached the maximum 150 °C between 9% and 10%. This indicates that the samples have a higher potential photothermal maximum. Various silicon scaffolds all show similar temperature increases indicating this effect is consistent between structures. Indeed, when we illuminated samples with a higher intensity laser, the temperature increase was enough to chemically alter the carbon shell structure. This changed the scaffold irreversibly from hydrophobic to hydrophilic.

As a control for the temperature increase under laser stimulation, we measured the temperature change for freeze cast collagen scaffolds, silicon wafers, and silicon wafers with water droplets. Collagen scaffolds showed no change in temperature between 0% - 10% power. The measured temperature for collagen scaffold for these laser intensities remains between 28.9°C – 29.9 °C. Both silicon wafers and silicon wafers with a water droplet on the surface demonstrate a maximum temperature from 28.9°C with no laser to 32 °C with laser at 10% power. We studied the potential for water evaporation from the surface by measuring the variation in evaporation times under light exposure for water droplets on SiNW scaffolds and water droplets on silicon wafers. Both Silicon wafers and SiNW wafers produced approximately 20% reduction in drying time under laser illumination. This analysis showed that scaffolds were able to dramatically reduce evaporation times through photothermal heating of the scaffold and heat transfer at the localized material – water interface. This supports the potential for this material to function in water evaporation applications.

From these calculations of significant photothermal potential it is clear that the both the high density of silicon nanowires and the carbon shell contribute to light absorption and photothermal activity. This photothermal activity is far beyond what we have previously seen for silicon either etched silicon nanostructures or mesoporous silicon nanostructures. From this active material we

are able to provide an added active functionality to the material for applications such as solar absorbers, water evaporation, or anti-icing properties. This monolith has significant light absorption, an open porous network, and the ability to float on a water surface providing localized heat transfer at the interface.

7.2.5 Conclusions and Outlook

We have demonstrated significant potential for this lightweight foam made from a silicon nanowire-carbon shell that we can achieve a wide range of tunable water material interactions. This variation provides insight into the factors that impact modification of surface – water interfaces based on nanostructure and surface chemical composition. Understanding how these two factors independently contribute to the production of either hydrophobic or hydrophilic surfaces could provide new insights for tailoring materials for sustainable energy and environmental applications. Control over superhydrophobic adhesive, rose petal, or repellent lotus leaf surfaces is applicable to water conservation in condensation collection and microdroplet transport, self-cleaning, antifouling, anti-icing, and drag reduction applications. The structure that hasn't been as easily accessible is structures mimicking the *Salvinia Molesta* fern with highly stabilized water material interfaces. Here, we demonstrated trapped air volumes submerged for hours and even trapped air under cyclic structural compression. The final addition of the active photothermal response is significant due to the high density of silicon and carbon. This opens up the range of materials applications to ice-phobic, anti-icing, and especially promising solar based steam generation.

7.3 Experimental

Fabrication of SiNWs : CVD synthesis procedure for the fabrication of 200nm AuNP is employed here. n-type Si wafers are plasma cleaned for 10 min at 100W. The surface is immediately treated with 1:3 Polylysine in water for 10 minutes. This solution is gently rinsed off with Di H₂O. Wafers are dried with nitrogen gas. When fully dry, 200 nm AuNP are deposited on the wafer surface for 2 hours. Solution is gently rinsed off with Di H₂O. Wafers are gently dried under nitrogen. Then wafers are loaded into the CVD quartz tube. SiNWs are synthesized at 485°C for 20 min at 40 Torr.

PVA solution : Before scaffold synthesis can begin 1% PVA solution is made in water and heated to 90°C for one hour with stirring. PVA for synthesis must be of the Mowiol variety for proper additive functionality.

Scaffold Fabrication : Weigh each Si wafer before sonication. Sonicate wafers in IPA for 5 min with a frequency of 37, power of 100, and sweep scan. Dry and re-weigh wafers. Subtract the new weight from initial weight to get NW weight. Centrifuge solution at 4000 G for 9 minutes or until all SiNWs are concentrated. Aspirate the supernatant. Dilute NW pellet to desired loading ratio in 1% PVA solution. Precool copper substrate with dry ice and ethylene glycol. Thoroughly mix slurry and add to mold on precooled substrate. Wait 30 minutes or until completely frozen. Remove sample and quickly place in -80C freezer overnight. Lyophilize samples for two days to remove water.

Burning of PVA structure : Place samples in quartz boat and load into quartz tube. Begin argon gas flow to remove oxygen. Ramp bake temperature to 500°C and hold for 1 hr. Cool to room temperature before disconnecting from argon gas flow.

Mechanical measurements via Instron tensile tester : Scaffold is adhered to a glass slide and loaded into the Instron. A flat surface is compressed into the material to measure compression stress strain response of the material. First the response under compression was measured by a uniaxial compression to 20% strain producing a force vs strain graph that defines the elastic regime of the material. Then cyclic compression at the desired strain is performed to determine the durability of the material under strain. Finally cyclic compression tests between 10% -50% is measured to determine the recoverability of the material.

Wettability of material measured by DSA : Contact angle of the different materials is measured via DSA (Kruss). The static contact angle is measured through fitting the droplet in the sessile mode in the Kruss software.

Droplet impact studies : Scaffolds are first adhered to glass slides and placed below syringe. Droplets of varied sizes are dropped from a range of heights to test the material response under different impact methods. Videos capture with high speed camera.

Droplet impact studies : Scaffolds are first adhered to glass slides and placed onto inversion structures. Droplets are added to structures and slowly rotated to 90°. An image in this state is captured. Next the scaffold is rotated to 180° and a second image is captured. The scaffold is

rotated back to 0° and a second droplet is added. The procedure is repeated until droplet detachment occurs.

Photothermal response under 532 nm laser : Each scaffold was located approximately two inches below the diffuse 532 nm laser. The laser intensity was ramped from 0p to 10p (max laser power). An image of the scaffold was captured by FLIR camera at each step to measure the change in photothermal profile. This was measured for scaffolds, collagen, and Si wafers with and without water droplets. For water droplet experiments the time for a droplet of the same volume with and without laser illumination was measured to determine the effect of photothermal heating at the interface.

7.4 Bibliography

- 1 Khanjani, P. *et al.* Superhydrophobic Paper from Nanostructured Fluorinated Cellulose Esters. *ACS Applied Materials & Interfaces* **10**, 11280-11288, doi:10.1021/acsami.7b19310 (2018).
- 2 Zhang, Z.-h. *et al.* One-step fabrication of robust superhydrophobic and superoleophilic surfaces with self-cleaning and oil/water separation function. *Scientific Reports* **8**, 3869, doi:10.1038/s41598-018-22241-9 (2018).
- 3 Chapman, J. & Regan, F. *Nanofunctionalized Superhydrophobic Antifouling Coatings for Environmental Sensor Applications—Advancing Deployment with Answers from Nature*. Vol. 14 (2012).
- 4 Xu, M., Sun, G. & Kim, C.-J. Infinite Lifetime of Underwater Superhydrophobic States. *Physical Review Letters* **113**, 136103, doi:10.1103/PhysRevLett.113.136103 (2014).
- 5 Zhang, X., Wang, L. & Levänen, E. Superhydrophobic surfaces for the reduction of bacterial adhesion. *RSC Advances* **3**, 12003-12020, doi:10.1039/C3RA40497H (2013).
- 6 Elbourne, A., Crawford, R. & Ivanova, E. *Nano-structured Antimicrobial Surfaces: From Nature to Synthetic Analogues*. Vol. 508 (2017).
- 7 Xue, C.-H., Guo, X.-J., Ma, J.-Z. & Jia, S.-T. Fabrication of Robust and Antifouling Superhydrophobic Surfaces via Surface-Initiated Atom Transfer Radical Polymerization. *ACS Applied Materials & Interfaces* **7**, 8251-8259, doi:10.1021/acsami.5b01426 (2015).
- 8 Sarshar, M. A., Song, D., Swartz, C., Lee, J. & Choi, C.-H. Anti-Icing or Deicing: Icephobicities of Superhydrophobic Surfaces with Hierarchical Structures. *Langmuir* **34**, 13821-13827, doi:10.1021/acs.langmuir.8b02231 (2018).

- 9 Kim, A., Lee, C., Kim, H. & Kim, J. Simple Approach to Superhydrophobic Nanostructured Al for Practical Antifrosting Application Based on Enhanced Self-propelled Jumping Droplets. *ACS Applied Materials & Interfaces* **7**, 7206-7213, doi:10.1021/acsami.5b00292 (2015).
- 10 Zuo, Z., Liao, R., Song, X., Zhao, X. & Yuan, Y. Improving the anti-icing/frosting property of a nanostructured superhydrophobic surface by the optimum selection of a surface modifier. *RSC Advances* **8**, 19906-19916, doi:10.1039/C8RA00712H (2018).
- 11 Park, S. Y. *et al.* Polarization-controlled differentiation of human neural stem cells using synergistic cues from the patterns of carbon nanotube monolayer coating. *ACS nano* **5**, 4704-4711, doi:10.1021/nn2006128 (2011).
- 12 Lee, C. & Kim, C.-J. Underwater Restoration and Retention of Gases on Superhydrophobic Surfaces for Drag Reduction. *Physical Review Letters* **106**, 014502, doi:10.1103/PhysRevLett.106.014502 (2011).
- 13 Chen, L., Si, Y., Guo, Z. & Liu, W. Superhydrophobic sand: a hope for desert water storage and transportation projects. *Journal of Materials Chemistry A* **5**, 6416-6423, doi:10.1039/C7TA00962C (2017).
- 14 Song, M. *et al.* Controlling liquid splash on superhydrophobic surfaces by a vesicle surfactant. *Science Advances* **3**, e1602188, doi:10.1126/sciadv.1602188 (2017).
- 15 Ito, Y. *et al.* Multifunctional Porous Graphene for High-Efficiency Steam Generation by Heat Localization. *Advanced Materials* **27**, 4302-4307, doi:10.1002/adma.201501832 (2015).
- 16 Avrămescu, R.-E., Ghica, M. V., Dinu-Pîrvu, C., Prisada, R. & Popa, L. Superhydrophobic Natural and Artificial Surfaces-A Structural Approach. *Materials (Basel, Switzerland)* **11**, 866, doi:10.3390/ma11050866 (2018).
- 17 Mayser, M. & Barthlott, W. *Layers of Air in the Water beneath the Floating Fern Salvinia are Exposed to Fluctuations in Pressure*. Vol. 54 (2014).
- 18 Barthlott, W. *et al.* The Salvinia Paradox: Superhydrophobic Surfaces with Hydrophilic Pins for Air Retention Under Water. *Advanced Materials* **22**, 2325-2328, doi:10.1002/adma.200904411 (2010).
- 19 James Hunt, B. B. Nanoscale biomimetics studies of *Salvinia molesta* for micropattern fabrication. *Journal of Colloid and Interface Science*, 187-192 (2011).
- 20 Barthlott, W. *The Salvinia Paradox: Superhydrophobic Surfaces with Hydrophilic Pins for Air Retention Under Water*.
- 21 Deville, S. Ice-templating, freeze casting: Beyond materials processing. *Journal of Materials Research* **28**, 2202-2219, doi:10.1557/jmr.2013.105 (2013).
- 22 L Li, W., Lu, K. & Walz, J. *Freeze Casting of Porous Materials: Review of Critical Factors in Microstructure Evolution*. Vol. 57 (2012).
- 23 Luo, Z. *et al.* Atomic gold-enabled three-dimensional lithography for silicon mesostructures. *Science* **348**, 1451, doi:10.1126/science.1257278 (2015).
- 24 Isaac Nelson, S. E. N. Intrinsic and extrinsic control of freeze casting. *Journal of Materials Research and Technology* (2019).
- 25 Mielonen, K. & Pakkanen, T. A. Superhydrophobic hierarchical three-level structures on 3D polypropylene surfaces. *Journal of Micromechanics and Microengineering* **29**, 025006, doi:10.1088/1361-6439/aaf7e4 (2019).

- 26 Wu, D. *et al.* Curvature-Driven Reversible In Situ Switching Between Pinned and Roll-Down Superhydrophobic States for Water Droplet Transportation. *Advanced Materials* **23**, 545-549, doi:10.1002/adma.201001688 (2011).
- 27 Weisensee, P. B., Tian, J., Miljkovic, N. & King, W. P. Water droplet impact on elastic superhydrophobic surfaces. *Scientific Reports* **6**, 30328, doi:10.1038/srep30328 (2016).
- 28 Kim, J.-H. & Rothstein, J. P. Droplet Impact Dynamics on Lubricant-Infused Superhydrophobic Surfaces: The Role of Viscosity Ratio. *Langmuir* **32**, 10166-10176, doi:10.1021/acs.langmuir.6b01994 (2016).
- 29 Vasileiou, T., Gerber, J., Prautzsch, J., Schutzius, T. M. & Poulikakos, D. Superhydrophobicity enhancement through substrate flexibility. *Proceedings of the National Academy of Sciences* **113**, 13307, doi:10.1073/pnas.1611631113 (2016).
- 30 Jamil, M. I. *et al.* Icephobic Strategies and Materials with Superwettability: Design Principles and Mechanism. *Langmuir* **34**, 15425-15444, doi:10.1021/acs.langmuir.8b03276 (2018).
- 31 Xiang Hui Xu, Z. Z., Fang Guoa, Jin Yang, XiaoTao Zhu. Fabrication of superhydrophobic binary nanoparticles/PMMA composite coating with reversible switching of adhesion and anticorrosive property. *Applied Surface Science* **257** (2011).
- 32 Zhu, H., Guo, Z. & Liu, W. Adhesion behaviors on superhydrophobic surfaces. *Chemical Communications* **50**, 3900-3913, doi:10.1039/C3CC47818A (2014).
- 33 Daniel Ebert, B. B. Wear-resistant rose petal-effect surfaces with superhydrophobicity and high droplet adhesion using hydrophobic and hydrophilic nanoparticles. *Journal of Colloid and Interface Science* **384**, 182-188 (2012).
- 34 Zhang, P., Li, J., Lv, L., Zhao, Y. & Qu, L. Vertically Aligned Graphene Sheets Membrane for Highly Efficient Solar Thermal Generation of Clean Water. *ACS Nano* **11**, 5087-5093, doi:10.1021/acsnano.7b01965 (2017).
- 35 Chen, C. *et al.* Highly Flexible and Efficient Solar Steam Generation Device. *Advanced Materials* **29**, 1701756, doi:10.1002/adma.201701756 (2017).
- 36 Gao, M., Zhu, L., Peh, C. K. & Ho, G. W. Solar absorber material and system designs for photothermal water vaporization towards clean water and energy production. *Energy & Environmental Science* **12**, 841-864, doi:10.1039/C8EE01146J (2019).
- 37 Zhu, L., Gao, M., Peh, C. K. N. & Ho, G. W. Solar-driven photothermal nanostructured materials designs and prerequisites for evaporation and catalysis applications. *Materials Horizons* **5**, 323-343, doi:10.1039/C7MH01064H (2018).

Chapter 8 : Conclusion and Outlook

Here we have (1) implemented a new method of characterizing the surface properties of silicon nanomaterials based on an PES analysis and then (2) implemented these materials characterized by PES for four different applications.. (1) This analysis ranged from tuning of CVD synthetic conditions to post synthesis modifications such as functionalization. From this method we explored a platform of silicon nanomaterials with facile fabrication but discovered significant variation in surface chemical composition and electronic band structure. From this analysis we demonstrated two different approaches to CVD tuning for specific applications; neuromodulation, and 3D atomic patterning. Next, we utilized PES analysis to characterize the impact of post CVD synthetic tuning including; APTES based functionalization, Hydrosilylation functionalization, MACE, addition of metal and metal oxide coats, and electroless deposition of gold. (2) Following this thorough PES analysis we chose to explore the applications of two of these materials, coaxial PIN SiNWs and 200 nm high phosphine doped SiNWs for both photoelectric and photothermal applications at four different interfaces. The PIN SiNWs were applied at polymer interfaces, cellular interfaces, and tissue interfaces. At each of these interfaces the waveguiding and photoelectric properties were exploited for stimulation of unique properties. For the second material, we fabricated hierarchal SiNW backbone – Carbon shell monoliths with modulated water interfaces ranging from superhydrophilic to superhydrophobic based on the nanostructure and chemical composition.

In the establishment of the PES method specifically, we were able to draw a wider conclusion about the factors of CVD synthesis, including temperature, pressure, doping, and diameter, that caused large shifts in the top 10 nm of these silicon nanomaterials. With this understanding of silicon nanomaterials we utilized this XPS and UPS method to characterize a

range of Si nanomaterials for different photoresponsive applications. This first focused on identifying the contamination of atomic gold at the surface of PIN SiNWs from the core shell growth process. We identified the chemical species of gold present at the surface to be atomic gold in the form of gold silicide. In conjunction with neuron experiments, we identified the presence of this atomic gold, compared to the metallic gold present in core SiNWs, to be a crucial component of the photoelectric stimulation of neurons. Additionally, we explored the effects of high doping ratios and large diameter SiNWs on the instability of the Au-Si eutectic alloy during the droplet. XPS revealed a large percent of the atomic signal to be an atomic gold component. After gold etching to remove the remaining metallic gold nanoparticle, the atomic gold peak becomes even more prominent. This identification of atomic gold along the surface of the wire was supported by MACE which revealed 3D periodic grooves along the surface of the silicon nanowires resulting from periodic pinning of the droplet during the growth. From this method of analysis we demonstrated an option for directly measuring surface electronic properties of nanomaterials and we employ chemical analysis at the interface to identify new CVD factors that exert control over the outermost component of the nanostructures. Further work in the PES characterization approach, would include the expansion of our characterized materials into a wider range of nanostructure diameter, doping ratios, and morphologies would provide a more comprehensive picture to explain what factors of CVD synthesis direct different surface modifications. Specifically, the majority of the current work has focused on p-type or n-type SiNWs, but intrinsic silicon can have significant impacts on the arrangement of gold at the surface of the SiNWs. We have expanded our capabilities of incorporation of atomic gold and demonstrated its importance for stimulation at biological interfaces. Further work will provide a deeper understanding of the impact of this atomic gold under illumination. Recent data has suggested that any amount of gold

incorporation at the silicon can result in H₂O₂ production at the interface. There are still many questions as to how this reaction could be occurring based on the band diagram of the silicon. A deeper delve into the range of gold silicon structures with this functionality specifically focusing on the band diagram directly measured for the silicon – vacuum interface using XPS/UPS method could provide some answers to questions in this current work. Additionally, the majority of the studies with photoresponsive applications are being carried out at solution interfaces. XPS/ UPS can provide insight into the surfaces at a vacuum interface, and developing a method to predict how the measured values at vacuum interfaces will be altered at something like a silicon electrolyte interface could be invaluable to photoelectric or photoelectrochemical work moving forward. Finally, this work could be carried one step further by integrating illumination into the analysis. The comparison of XPS/UPS analysis for PIN structures with and without illumination could provide insight into the changes that occur during the generation of charge carriers.

In contrast, surface modifications that can be applied post CVD synthesis to link functional groups or modify the interface of the SiNWs. We employed XPS and UPS to measure the quality of the modifications or the effects on the interface of the resulting materials. Further work would be a full scale PES analysis of each of these modifications although there are some challenges in the form of carbon contamination, applying the XPS/UPS analysis to post synthetic modifications such as functionalization and etching could expand our understanding of those processes. Here we introduced two different method for linking compounds to the surface of the SiNWs. The first approach relies on an insulating OH layer for functionalization with APTES. In the second approach, we utilized hydrosilylation starting from hydrogen terminated silicon surfaces. Both of these surface treatments would result in very different photoelectric activity at the interface and can be used to tailor materials for one application or another. For this reason a full PES study of

the band structure variation would provide insight into the effect of the carbon linkage to the silicon surface. Previous work has shown that the types of functionalized molecules bound through Si-C or Si-O linkages results in drastic shifts in the measured surface electronic properties. For application of these SiNWs bound to antibodies and cells (as an example) for stimulation purposes, we would benefit from implementation of the full PES analysis. This was identified through chemical identification of species such as Si, SiO₂, N, O, and C at the surface. From this method SiNWs were in one approach functionalized with a linker to act as a hook into the cellular membrane to localize the device at a specific region of the cell. In the second approach the functionalization process linked an antibody to the SiNW surface and employed this functionality to bind T cells to SiNWs. In an alternative approach for post synthetic modification SiNW surfaces were etched by the MACE process to enhance photothermal processes. The varying steps in this process were monitored through XPS to identify the effects of each step including addition of gold, MACE, and gold etchant to track surface modifications. At the current level of analysis it is clear that the MACE process involves charge transfer at the interface and could be resulting in significant surface rearrangement. Exploring the true rearrangement of gold on the surfaces after these etching processes via SEM, TEM or APT would support the current XPS measurements. This would inform the changes in the measured electronic properties and provide a clearer picture of the process. We then explored the silicon – metal or silicon – metal oxide interfaces that could be produced through post synthesis modifications including sputter coating, e-beam evaporation, ALD, and electroless deposition. XPS depth profiling probed these interfaces for both SiNWs and Si wafers. From this analysis we found that TiO₂ ALD deposition produces the sharpest interface with significantly less intermixing between the metal oxide and silicon when compared to ALD of Al₂O₃ or any form of gold deposition. In the analysis of the gold silicon interfaces we found that

the interface was predominantly islands of gold with a buried interface of gold silicide. This occurred for sputter coating, e-beam evaporation, and electroless deposition at differing intensities. The key result of these surface modifications is that it allows us to directly tailor the Si interfaces to shift photoresponsive mechanisms between photothermal, photoelectric, or photoelectrochemical and XPS provides detailed clues to surface modifications or rearrangements. Based on this information we have a clear picture of the different types of interfaces produced. Measurements of the production of hydrogen peroxide off these surfaces would allow us to investigate the impact of each approach on the photoelectrochemical potential. Specifically, TiO₂ surfaces have been used to produce H₂O₂ but it is unclear if it would work cooperatively with the Si-Au. Additionally, with these three different methods of post synthesis addition of gold, we could further explore the requirements for photochemical reactions, such as production of H₂O₂, at the interface. The current picture is unclear outside of the fact that significant gold : silicon atomic percent is not required. For this reason, a study of the change in photoelectrochemical efficiency at each step in the depth profiling procedure could reveal what interface, chemical arrangement, or chemical species is key to this activity.

Based on this PES analysis, we selected of materials for specific applications. In one approach we selected on SiNW characterized in depth through both XPS and UPS to provide photoelectric stimulation at biological interfaces, and we selected one of our other characterized SiNWs to explore photothermal interactions at water interfaces.

Based on the PIN coaxial SiNWs, we fabricated polymer based high density silicon mesh. The photolithographic patterning process took advantage of the waveguiding properties to form polymer ribbons for rugged and durable structures with enhanced water adhesion due to the micro and nanostructure. Looking forward into the next steps for understanding the SiNW polymer

interfaces, an exploration of the other impact of the nanofibers of polymer (beyond the current study of durability of silicon mesh across a large window) resulting from waveguiding would provide more insight into the waveguiding process. Additionally, the comparison of different versions of SiNW structures would allow us to identify what specific properties, length, diameter, shell roughness, gold contamination, ect convert this activity. For this, a study of the range of nanomaterials characterized via XPS/UPS, core, core shell (nn or pp), doping ratio, gold variation, diameter, would provide more detailed information on what properties enhance these effects. It is clear from data on low loading doses of large SiNWs excessive waveguiding enhanced film formation occurred. If we apply these other materials characterized by PES we could tease out the factors that enhance these waveguiding effects. Alternatively, different surface functionalization, even just exploring the impact of plasma cleaned versus hydrogen terminated silicon, could significantly tailor the interaction with the polymer altering these properties. It is possible that any silicon nanowires will participate to a similar degree, but with the wide material platform we have the option to study these different components more in depth.

Secondly, we applied this high density photovoltaic based silicon nanowire structure for cellular stimulation. The combination of an x-y scanning based optical stimulation method with the waveguiding properties of the high density mesh efficiently to pace isolated cardiac cells. Carrying forward the work of the cellular stimulation based on a scanning stimulation method and high density bio-material interface could be applied to different areas of research. Due to the significant reduction in required light intensity for stimulation, this scanning based approach could be a benefit for optical stimulation of sensitive cell types that suffer from impaired cellular activity under the levels of light exposure required for other point stimulation based methods. Alternatively, a fundamental study investigating the potential for a series of low intensity inputs

spatially distributed across the cell potentially mimicking the physiological method in which cells interact with their native environments could provide more support for this type of stimulation provide more efficient or physiologically relevant cellular responses. In addition to a fundamental study on the spatial distribution of stimulation, there is still a significant question about the true interaction between cells and the photoresponsive PIN SiNWs. The most likely scenario is that stimulation is similar to other electrical pacing methods, but a range of interactions have been proposed ranging from photoelectric to photoelectrochemical. A fundamental study of the true interface for stimulation would be an ideal next step. Finally, the measured cellular response to training demonstrated cells could maintain the paced frequency for up to around 45 minutes, but there were several external factors limiting those measurements including the impact of Fluo-4 staining on cell viability over long periods of time, Fluo-4 bleaching, or CO₂ incubator for the duration of the stimulation all limit cell life time.

Based on this cellular stimulation success and the unique material properties of high flexibility and water adhesion, we applied this material at the tissue level. We demonstrated that this scanning functionality could be applied in the z-plane based on natural tissue movements at the tissue surface. The combination of the scanning stimulation and high density mesh effectively paced isolated hearts. The tissue material interface was supported by the flexibility of the scaffold under mechanical stresses and the high water adhesion that wicked the material to the heart surface without the need for sutures or glue. The majority of this work focused on cardiomyocytes, but this material would be functional with other electrically responsive cell types. Moving this work forwards to clinical or therapeutic applications, a wider set of options for cell – material interfaces would expand the functionality of the material. Neurons are a promising candidate specifically with the option to interact with the vagus nerve with potential implications for digestive issues,

treatment resistant depression, stress responses, or a wide range of other ailments. Previous work stimulating the vagus nerve has had promising results as a therapeutic target. Additionally, the vagus nerve is located much closer to the skin surface making it an ideal target for light based stimulation. Although one of the issues with the current cardiac treatment approach is the light penetration depth into tissue, there are several options that could be explored as a solution including flexible implantable micro LEDs for stimulation closer to the tissue interface. The benefit of implantable micro LEDs is that they are significantly less bulky and have been shown to have reduce immunogenic responses. The next step for demonstrating efficacy would be in vitro implantation of the polymer device and a study of the immunogenic or fibrotic response of the body. If this material is demonstrate to truly be more biocompatible with soft tissue interface, stimulation studies in vivo with implantable micro LEDs or NIR stimulation would be the next focus. NIR is an ideal solution for tissue studies as it has a deeper penetration depth compared to the green laser wavelengths studied currently. Due to the fact that silicon absorbs significantly in the NIR region, this is one of the key solutions to challenges of buried tissue interfaces. Additionally, expanding the analysis of the tissue platform would be crucial to clinical or therapeutic applications.

Finally, we developed a 3D silicon nanowire based foam for the modulation of water interfaces. This foam utilized biomimetic surfaces to create novel water interactions based on the fern *Salvinia Molesta*. This material was based on SiNW backbone with a binding of carbonized PVA material. The result of this structure was a highly flexible material with strong photothermal capabilities. Scaffolds can vary between hydrophilic to hydrophobic repellent to hydrophobic adhesive based on nanostructure and chemical composition. There are still many questions facing the true source of the factors dictating the water interfaces. Currently, a study of the chemical

species is challenging as the nanoscale topography indicates that there are small regimes predominated by different chemical species. A deeper analysis of these surfaces integrating UPS data potentially, would provide more control over the shift between each different regime. Additionally, the biggest challenge to synthesis of these materials for a variety of applications is the issue with scaling up the process. The raw material required for each sample is significant and can take on the order of days to produce a quality scaffold. An alternative to this process would be exploring the option of bottom up synthesis for the scaled up production of silicon nanowires. Alternatively, initiating growth with smaller diameter gold NP followed by shell growth to produce 200 nm SiNWs would produce a higher yield of SiNWs. This results from the physical challenges facing the initiation of SiNW growth of SiNWs from 200 nm AuNPs. The expansion of the functionality of the material would also significantly carry this project forward. Specifically, taking advantage of the photothermal properties of the SiNW scaffold could be achieved through the exploration of anti-icing or de-icing applications. Due to the fact that the scaffold has a significant photothermal response this application could be ideal. Alternatively, the implementation of lightweight scaffold monoliths capable of floating on water surfaces have previously been used in green energy applications through photothermal steam generation. Effective materials for this process have several key factors including photothermal properties, large pores for escape of steam, minimal water – material contact area, and a lightweight material capable of floating at the water surface. Due to the fact that this material excels in all of these categories it would be interesting to explore the potential for solar steam generation based on this SiNW-Carbon scaffold.

The conclusion of this work results in a (1) new PES method for directly measuring Si nanomaterial surface chemical composition and electronic band structure (2) a library of tools

applicable to a range of applications that are well characterized for (3) practical applications of this analysis method to the development of new materials with either photoelectric or photothermal properties.